Emergence of disordered collective motion in dense systems of isotropic self-propelled particles

Yann-Edwin Keta

THÈSE POUR OBTENIR LE GRADE DE DOCTEUR DE L'UNIVERSITÉ DE MONTPELLIER

En Physique et Astrophysique

École doctorale : Information, Structures, Systèmes

Unité de recherche : Laboratoire Charles Coulomb, UMR 5221 CNRS
Université de Montpellier

Emergence of disordered collective motion in dense systems of isotropic self-propelled particles

Présentée par Yann-Edwin KETA

Le 29 septembre 2023

Sous la direction
Ludovic BERTHIER et Robert L. JACK

Devant le jury composé de

Ludovic BERTHIER	Directeur de recherche	Université de Montpellier	Directeur
Olivier DAUCHOT	Directeur de recherche	ESPCI Paris	Président
Silke HENKES	Professeure associée	Universiteit Leiden	Examinatrice
Robert L. JACK	Professeur	University of Cambridge	Directeur

et après rapport de

Cécile COTTIN-BIZONNE	Directrice de recherche	Université Claude Bernard Lyon 1	Rapportrice
Julien G. TAILLEUR	Professeur associé	Massachusetts Institute of Technology	Rapporteur

UNIVERSITÉ
DE MONTPELLIER

Emergence of disordered collective motion in dense systems of isotropic self-propelled particles

Émergence de mouvement collectif désordonné dans des systèmes denses de particules auto-propulsées isotropes

Yann-Edwin Keta

24/12/2023, 16:04

To Aaron Swartz and all those who share.

Summary

Active matter is a broad class of materials within which individual entities, the active particles, consume energy in order to perform movement. These materials are at the intersection of many distinct fields of research, such as biology, engineering, and physics, and have thus attracted considerable attention. Because of their perpetual consumption of energy, these systems are out of thermodynamic equilibrium. As a consequence they display a wealth of surprising phenomena which challenge our conception of equilibrium phases and dynamics. Among them, collective motion is particularly intriguing and exciting on multiple grounds. First because it emerges in systems with distinct length and time scales, from collections of cells to large crowds, flocks, and swarms, yet with some common characteristics. This thus suggests some sense of universality in the mechanisms leading to different collective behaviours. Second because parts of these motions display signatures shared with other equilibrium phenomena. While the latter are very diverse, ranging from the glass transition to inertial turbulence, these connections mean that a number of concepts and tools are readily available to describe out-of-equilibrium behaviours. Third because the possible applications of the understanding and control of these phenomena are far-reaching: treatment of specific pathologies, design of intelligent materials, crowd management, etc. In this Thesis, we focus on dense active matter, where the movement of individual particles is hindered by crowding effects, and aim to characterise how this competition leads to emerging collective motion. To this effect we use a simple model of two-dimensional isotropic self-propelled particles, namely active Ornstein-Uhlenbeck particles, where the departure from the equilibrium limit is controlled via the persistence time of propulsion forces. Owing to its simplicity, the phenomena described within this model have the potential to apply to a broad range of materials. We broadly map the phase behaviour of this model, from the equilibrium-like regime at small persistence to the to far-from-equilibrium regime at large persistence. We focus our efforts on the latter regime, where velocity correlations were recently shown to emerge. We demonstrate that a disordered liquid phase exists up to very large persistence, if polydispersity frustrates the ordering of the system, and that this persistent liquid displays various manifestations of disordered collective motion. First, we show that persistent systems are dynamically arrested at large packing fraction. Close to dynamical arrest, we find that the liquid displays dynamical heterogeneity similar to equilibrium dense systems. We investigate, in the idealised limit of infinite persistence, the microscopic processes leading to these heterogeneities. Then, away from dynamical arrest, we show that our model displays chaotic advection flows, as typically shown by turbulent systems. We highlight how this specific behaviour may be universal to a broader class of active systems relying on the competition of crowding and persistent forcing. Finally, in monodisperse systems which display long-range order at large packing fraction, we describe the far-from-equilibrium mechanisms leading to structural relaxation.

Résumé

La matière active est une vaste classe de matériaux au sein desquels chaque entité, les particules actives, consomme de l'énergie pour effectuer un mouvement. Ces matériaux sont à l'intersection de plusieurs champs de recherche distincts, tels que la biologie, l'ingénierie et la physique, et ont donc attiré une attention considérable. En raison de leur consommation perpétuelle d'énergie, ces systèmes sont hors de l'équilibre thermodynamique. En conséquence ils exhibent une myriade de phénomènes surprenants qui défient notre conception des phases et dynamiques à l'équilibre. Parmi eux, le mouvement collectif est particulièrement intriguant et excitant sous plusieurs aspects. Premièrement parce qu'il émerge dans des systèmes aux échelles de longueur et de temps distinctes, des ensembles de cellules aux larges foules, troupeaux et essaims, avec cependant des caractéristiques communes. Cela suggère alors une logique universelle derrière dans les mécanismes à l'origine de ces différents comportements collectifs. Deuxièmement parce que certains de ces mouvements ont des signatures communes avec des phénomènes d'équilibre. Bien que ces derniers soient très divers, allant de la transition vitreuse à la turbulence inertielle, ces connections donnent accès à de nombreux outils et concepts afin de caractériser les comportements hors-équilibre. Troisièmement parce que les applications possibles d'une compréhension fine voire du contrôle de ces phénomènes sont d'une grande portée : traitement de pathologies spécifiques, conception de matériaux intelligents, gestion des foules, etc. Dans cette Thèse, nous nous concentrons sur la matière active dense, où le mouvement des particules individuelles est entravé par des effets d'encombrement, et cherchons à caractériser comment le mouvement collectif émerge de cette compétition. Pour cela nous utilisons un modèle simple en deux dimensions de particules auto-propulsées isotropes, à savoir des particules d'Ornstein-Uhlenbeck, où l'écart à la limite d'équilibre est contrôlée par le temps de persistance des forces de propulsion. En raison de sa simplicité, les phénomènes décrits pour ce modèle ont le potentiel de s'appliquer à une variété de matériaux. Nous cartographions les phases de ce modèle, du régime proche de l'équilibre à petite persistance au régime loin de l'équilibre à grande persistance. Nous concentrons nos efforts sur ce second régime, là où a été récemment

montré l'émergence de corrélations de vitesse. Nous démontrons qu'une phase liquide désordonnée existe à très grande persistance, à condition que la polydispersité frustre l'ordre structurel, et que ce liquide exhibe différentes manifestations de mouvement collectif désordonné. D'abord, nous montrons que les systèmes persistants sont dynamiquement arrêtés à grande densité. Dans le voisinage de l'arrêt dynamique, nous trouvons que le liquide affiche des hétérogénéités dynamiques similaires aux systèmes denses à l'équilibre. Nous examinons, dans une limite idéale de persistance infinie, les processus microscopiques menant à ces hétérogénéités. Ensuite, à distance de l'arrêt dynamique, nous montrons que notre modèle exhibe des écoulements d'advection chaotiques, à l'instar des systèmes turbulents. Nous mettons en exergue comment ce comportement spécifique pourrait être universel au sein d'une classe plus large de systèmes actifs s'appuyant sur une compétition entre l'encombrement et le forçage persistant. Enfin, dans des systèmes monodisperses qui exhibent à grande densité un ordre à longue portée, nous décrivons les mécanismes permettant la relaxation structurelle loin de l'équilibre.

Remerciements

Quelle aventure mes ami·es... Après les épreuves de la rédaction et de la soutenance, après mon déménagement hors de Montpellier, et à l'aube d'une nouvelle année, je peux enfin me poser, repenser à ces trois années de thèse, et écrire ces quelques lignes pour remercier celleux sans qui je ne serais sûrement pas allé jusqu'au bout.

Tout d'abord je veux remercier mes directeurs, Ludovic et Rob. Ludovic d'abord qui a accepté de croire avec moi en ce projet et m'a offert cette possibilité d'étudier avec lui au sein de son groupe à Montpellier. Merci énormément à Rob aussi qui, malgré la distance entre Montpellier et Cambridge, a su m'aider et m'aiguiller, merci pour son enthousiasme et son soutien. Merci aux deux de m'avoir "supporté" durant toute cette thèse – voire même depuis avant cela.

Merci aussi à mon jury, mes rapporteurices Cécile et Julien, et les membres du jury Olivier et Silke. Merci beaucoup pour les nombreuses discussions durant ma thèse, qui ont su me rappeler, à des moments où je pouvais douter de moi et de mes recherches, à quel point j'aimais faire de la physique et le ravissement que j'éprouvais à discuter de nouvelles idées et de nouvelles méthodes. Merci également d'avoir accepté d'évaluer mon travail et merci pour les intéressantes questions et discussions durant ma soutenance.

Je voudrais exprimer toute ma gratitude pour mes camarades du laboratoire Charles Coulomb. Merci bien évidemment à toustes les membres de l'équipe, avec qui j'ai pu partager un bureau, de nombreux repas conviviaux, et des sorties pour se changer les idées. Merci donc à Cecilia, Juliane, Gerhard, Olivier, Benjamin, Romain, Yonglun, Kumpei et Leo. Un grand merci également aux autres non-permanent·es, avec qui j'ai pu organiser plusieurs événements, avoir des discussions plus ou moins sérieuses au laboratoire, et surtout avec qui j'ai pu bien rigoler pour faire redescendre la pression. Merci beaucoup à MJ, Adrien, Alrik, Adam, Khalil, Nick et Clara. Finalement j'aimerais remercier toustes les non-permanent·es de mon laboratoire d'adoption, l'IMAG, à quelques bâtiments du L2C, pour leur sympathie et leur humour.

Parce que la vie ce n'est pas que la sphère professionnelle, mais bien, bien plus, j'aimerais également remercier de tout mon cœur celleux qui ont fait de ce "bien plus" un moment fantastique, qui ont partagé mes joies quand j'étais au plus haut et qui m'ont permis de tenir quand j'étais au plus bas.

Merci à mon *broer* Alan, qui a été à mes côtés dès mon premier jour à Montpellier, qui m'a fait connaître la ville et les petit·es rigolos qui la peuplent, avec qui j'ai rigolé, pleuré, dansé, chanté, chillé, et qui est toujours avec moi malgré la distance. Merci à Damien, toujours le sourire aux lèvres et le cœur sur la main, merci pour son enthousiasme, son aide, pour sa *déter'* et son excellente compagnie. Merci d'avoir été et d'être toujours là. Merci à Antoine pour son sens de la bonne blague et ses envolées lyriques, pour avoir été un si bon compagnon de baby-foot et un danseur toujours enthousiaste. Merci à Valentine pour sa bonne humeur communicative, son amour débordant et gestes attentionnés. Merci à Morgane pour tout ce qu'on a partagé pendant ces années. Merci à Bart et Ozzy pour avoir été de si bons camarades et toujours été au rendez-vous.

Merci à Aria, Cam et Pauloss pour être des personnes exceptionnelles, merci pour votre bêtise comme pour votre intelligence. Merci de m'avoir accompagné tous les jours depuis de nombreuses années, je vous aime. Merci à Élise pour son humour et son amour, son soutien et toute la force qu'elle m'a insufflée. Merci aussi à toute la colo. Merci Sonpier.

Merci papa et maman, merci Bibiche et toustes mes frères et soeurs. Merci à Montpellier, ses librairies, ses cafés, ses gens dont toustes celleux – nombreu·ses – que je ne n'ai pas cité·es. Merci à Charlotte, Lucille, Florine et Marta.

Merci aux éditeurices de Wikipedia, aux contributeurices de StackExchange, et aux développeur·ses de logiciels libres.

Contents

1 Introduction

1.1 Broad context

Statistical physics aims at bridging the gap between microscopic properties and macroscopic behaviours. While simple individual entities (commonly called *particles*) could be described by *e.g.* Newtonian mechanics, the description of a large collection of them (of the order of $\mathcal{N}_\mathrm{A} \approx 10^{23}$) necessitates the use of statistical descriptors. The kinetic theory of gases is one of its earliest examples, linking macroscopic properties such as temperature and pressure to a microscopic property, namely the average kinetic energy of particles. In the presence of interactions between the constitutive entities of the system, the behaviour of the ensemble may be different than the behaviour of separated individuals: this is called an *emerging phenomenon*. We encounter many of these in our everyday life: water molecules in a dilute gas seldom interact and move freely, however upon compression they may *transition* to a liquid state which flows viscously, while upon cooling they may transition to a solid state which resists elastically to external constraints.

A central concept in statistical physics is thermodynamic equilibrium, which is the property of a system where there are no macroscopic flows of matter or energy. The system is invariant under time reversal, a consequence of which is detailed balance: each microscopic process within the system is equilibrated by its reverse process which happens with equal probability. Within this hypothesis, a wealth of very broad and powerful relations are available to describe the system, such as the equilibrium Boltzmann distribution which relates the probability of a given state to its energy and to temperature, and also fluctuation-dissipation theorems which relate fluctuations at equilibrium to the response of the system to external perturbations.

There are several ways a system can break detailed balance and time reversal symmetry, and thus be out of equilibrium [1]. First, one may impose external gradients, which consequence is to create macroscopic flows opposing this gradient. For example, in a kettle filled with water and heated at one extremity, convective flows will propagate the heat through the liquid. Second, the system may be relaxing towards equilibrium, for example the water in the kettle after one removed the heat source. This relaxation can be slow or even infinitely slow in the case of *glasses* [2]. Third, some of the particles may be able to use stored or ambient energy to *e.g.* perform movement or induce energy flows, this is the case in *active matter* [3, 4]. (The latter name is in opposition to *passive*, *i.e.* equilibrium, systems.) These examples are not exclusionary: in this Thesis we will encounter the overlap between slowly relaxing and active systems.

1.2 Active matter

Active matter is an umbrella term which applies to a broad range of living and synthetic systems at all scales: from cell tissues [5–7] and suspensions of microtubules [8, 9] or colloids [10–13], to human crowds [14, 15] and robot swarms [16], and to bird flocks [17, 18] and fish schools [19]. In all these examples, individual entities (called *active particles*) are able to perform movement on their own by consuming energy. Because of this consumption of energy, the movement of an active particle is not time-reversal symmetric, and the system is out of equilibrium. These movements are extremely diverse, and imply various interactions between the particles and their environment, *e.g.* individual cells may crawl on an underlying substrate or use flagella to propel themselves in a fluid. Moreover, the interactions between the particles are also diverse, *e.g.* chemical signalling, visual signalling, or hydrodynamic interactions. Due to these interactions, an ensemble of these particles may display an emerging collective behaviour which is different from the behaviour of the individual. A central endeavour in active matter research is to identify mechanisms underlying these collective behaviours and which are universal over different classes of system. Among these behaviours, we will devote special attention to collective motion, in which active particles perform spatially correlated movement in the absence of external gradients.

Understanding the behaviour of active systems is of great interest in engineering and biology, *e.g.* to design metamaterials, to understand the spread of cancer cells and wound healing [6], or for crowd safety and management [14, 15]. These also have applications in theoretical physics. Indeed, these provide useful toy models to extend concepts and tools from equilibrium statistical physics to the out-of-equilibrium realm, *e.g.* pressure [20, 21] or fluctuation-dissipation relations [22, 23].

A physical approach to the field of active matter mainly involves two powerful tools. First, the simplification

of the problem, with the development of models which can be thoroughly studied. Here the simplification refers to the reduced number of choices in the parametrisation of the problem, not in the behaviour of the model itself. Indeed, despite their simplicity these models may present complex emerging behaviour as we will show below. The point of starting from simple models is that it enables us to pinpoint the relevant physical mechanisms at the origin of these complex behaviours. Second, the use of advanced numerical methods to explore the correspondence between microscopic and macroscopic behaviour.

A common and versatile class of models for active matter is self-propelled particles. In these, activity is introduced as non-gradient forces acting on each particle. We call these *propulsion forces*. They may be deterministic [24, 25] but are most often stochastic. We must differentiate systems where there are no couplings between these forces, and systems where these couplings exist and thus where we have to consider their order (usually *nematic* or *polar*). We will refer to these active systems as being *isotropic* and *anisotropic* respectively.

Intense analytical and numerical efforts have been devoted to the study of self-propelled particles in two spatial dimensions. The reason for this is that numerous biological systems of interest have effectively two-dimensional dynamics, *e.g.* monolayers of swimming bacteria [26], confluent cell monolayers [27], and suspensions of microtubules confined to an oil-water interface [28]. We will in this Thesis focus on two-dimensional active matter. This choice of dimensions has important consequences for the fluctuations in dense phases which we will detail in Secs. 1.3, 1.4.

1.2.1 Anisotropic active matter

One of the earliest examples of anisotropic self-propelled particles model is the Vicsek model [29]. It starts from the observation that, in many biological systems, individuals tend to move similarly to other individuals in their neighbourhood. Vicsek *et al.* thus proposed a model in which a given particle in a two-dimensional space moves at a constant speed, and the direction of this velocity is updated at regular intervals to assume the average movement direction of its neighbours in a radius r, with an additional random perturbation. This model only has 2 control parameters: the amount of noise and the density (which sets the typical number of neighbours in a radius r). An individual particle performs a persistent random walk, however an ensemble of these show a transition, at low noise and large density, to an ordered polar phase in which all particles move in the same direction, resembling flocks of birds or bacteria. This model thus exemplifies how local microscopic interactions may lead to coherent motion on much larger scales. It is noteworthy that this transition to a polar phase involves a spontaneous breaking of continuous symmetry in two dimensions, which at equilibrium is forbidden by the Mermin-Wagner theorem. Since self-propulsion takes the system out of equilibrium, this transition is possible in the Vicsek model.

When describing dense active matter, *e.g.* dense cell tissues, steric interactions may matter. To account for these effects, numerous models involving repulsions between particles or density-dependent velocities have been introduced. These models were very powerful at reproducing complex behaviours observed in experiments, such as pattern formation [30] or bacterial swarming [31], enabling us to study these phenomena with greater precision.

1.2.2 Isotropic active matter

In isotropic models of self-propelled particles, propulsion forces follow independent stochastic processes which are usually defined by their standard deviation (their *strength*) and the time scale over which they decorrelate with themselves (their *persistence time*). In the limit of zero persistence time the active propulsion force acts as an uncorrelated white noise, thus this is commonly considered as the equilibrium thermal limit, and increasing persistence time as taking the system further from equilibrium [22]. A typical example of isotropic self-propelled particles is run-and-tumble particles (RTPs) [32, 33], which is inspired by the motion of *Escherichia coli*. In this model, particles are propelled with forces of fixed strength and which randomly change their directions with a given fixed tumble rate (*i.e.* inverse persistence time). An individual particle thus also performs a persistent random walk. However an ensemble of these, interacting via repulsive interaction, show a transition at large persistence time and moderate density to a phase-separated state known as motility-induced phase separation (MIPS) [1]. This transition bears similarities with the liquid-gas phase separation, with the steady state of the system showing a dense macroscopic cluster immersed in a dilute gas. Borrowing terms from equilibrium systems, we may then ask if this dense cluster is a flowing *liquid* or an arrested *solid* (see Secs. 1.3, 1.4).

Isotropic models also display some forms of collective motion in "extreme conditions". Ref. [34] proposes to define these conditions as a combination of large propulsion strength and persistence time with respect to the typical strength of interparticle interactions and typical time of relaxation time in the absence of activity. In this setting, systems of isotropic self-propelled particles were shown to support mesoscopic velocity correlations as a consequence of the coupling between density fluctuations and persistent active forcing [34–37]. There is

evidence that these correlations of instantaneous motion translate into large length scale correlated motion on larger time scales, either in the form of avalanche-like dynamics in which small local changes are at the origin of large-scale motion [34, 38] (see Sec. 1.4), or in the form of chaotic flows [34, 39] (see Sec. 1.5).

1.3 Crystallisation

At large density and low temperature, equilibrium systems may be most thermodynamically stable in the form of a crystal. Crystals are elastic solids, within which the arrangement of particles follows a lattice which is periodic in all directions of space. The process by which a disordered liquid transforms into an ordered crystal, *crystallisation* (and its inverse *crystal melting*), is highly dependent on the number of spatial dimensions. In three dimensions, this transition is a discontinuous first-order transition. Crystal nuclei are first formed in the bulk liquid and grow until the whole system is ordered. In this three-dimensional crystal, particles have finite (thermal) fluctuations around their lattice site, thus order may be conserved. This is not the case in two dimensions: in the absence of long-range interactions, there are long-wavelength fluctuations around the lattice sites which amplitude grows as the logarithm of the system size. These are known as Mermin-Wagner fluctuations. Therefore, for large enough systems, these fluctuations are much larger than the typical length between particles and the order is destroyed. These fluctuations do not however forbid the existence of a transition to an ordered solid, but the mechanism by which a two-dimensional liquid forms an ordered crystal is different from its three-dimensional counterpart [40].

Topological defects play a crucial role in the melting of two-dimensional crystals [41, 42]. Consider an ensemble of identical disks. In two dimensions the densest packing has particles arranged in a regular hexagonal lattice, within which each of these disks has exactly six nearest neighbours. This corresponds to the perfect crystal, which is invariant by translation along the lattice primitive vectors. There are two kinds of order in this packing: *translational* order, indicating that neighbouring particles fluctuate around equally spaced positions along the lattice primitive vectors, and *orientational* order, indicating that nearest neighbours particles are found in the directions of the lattice primitive vector. A *disclination* is a topological defect that corresponds to a particle which has a number of neighbours different than six, typically five or seven. Thus locally these defects break orientational order. Two bounded disclinations, *i.e.* a couple of particle with respectively 5 and 7 neighbours and which are neighbours of each other, corresponds to a *dislocation*. The latter is an other topological defect around which orientational order is conserved but not translational order. Finally, it is noteworthy that dislocations may also be bonded, in which case translational order is conserved away from the defects. Kosterlitz-Thouless-Halperin-Nelson-Young (KTHNY) theory predicts that the melting of a two-dimensional crystal with increasing temperature or decreasing density is a two-step process [43]. First, global translational order is destroyed, which at the topological level happens through the unbinding of dislocations. As a consequence the shear elastic modulus vanishes and the system is fluid. This fluid is however not isotropic as the orientational order is still conserved globally, it is called an *hexatic* phase. Second, global orientational order is destroyed, which at the topological level happens through the unbinding of disclinations. The resulting system is an isotropic liquid phase. The solid-hexatic transition, at equilibrium, is a continuous transition [44], while the hexatic-liquid transition may be either first-order or continuous [45].

On the one hand, this two-step melting scenario has been confirmed in some dense active systems of identically shaped particles, either isotropic [46, 47] or anisotropic [48]. It was also reported, for a model of isotropic self-propelled particles, that the dense phase of MIPS is structurally similar to an equilibrium crystal near the crystal-hexatic transition [49]. Interestingly, despite displaying the structural characteristics of a two-dimensional solid, these dense large-persistence phases display at the same time the dynamical characteristics of a fluid [49, 50] – a behaviour which cannot be observed at equilibrium. There is thus a non-trivial relation between structure and dynamics in dense active systems.

On the other hand, an experiment with dense athermal vibrated disks highlighted that, right below ordered close packing, the system featured finite-sized crystalline clusters [51]. From a static point of view, this situation is not dissimilar to an equilibrium phase separation, which would indicate a first-order transition between a disordered liquid and an order solid. However a careful dynamical inspection shows that these clusters "self-melt" by continuously forming active liquid bubbles [51], which behaviour is incompatible with the KTHNY scenario.

1.4 Glass transition

Glasses are ubiquitous in our everyday life (and vocabulary). It is no doubt that the person reading the present Thesis will have around them a *glass* cup, or a window *glass*, or may even be reading this text through *glasses*. Humans have been using naturally occurring glasses and making their own for millennia, yet the physical

process by which a liquid becomes a glass is still an intense field of research. One way to obtain a glass is to *supercool* a liquid beyond its freezing point. At low temperature, the ordered crystal may be thermodynamically favoured with respect to the disordered liquid, and the latter should transition to the former. However there is a kinetic component to this transition: in three dimensions crystal nuclei must be formed then grow until the whole system is crystalline. This transition may be avoided at large cooling rates, especially if the composition of the system frustrates structural order, which is achieved *e.g.* in simple systems by employing a variety of sizes for the particles. In these conditions the viscosity of the fluid increases significantly, reaching a point where no dynamics can be observed on experimental time scales, and the system is effectively dynamically arrested. The process through which the disordered liquid transforms into an arrested solid is called the *glass transition* [2, 52]. It is noteworthy that this transition happens without any noticeable change in the structure between the liquid and the glass which show, contrarily to the crystal, similar disordered structure – a problem which has puzzled physicists for decades [53, 54].

The glass transition must be distinguished from the jamming transition through which a disordered (or *amorphous*) granular material acquires an elastic bulk modulus at large packing fraction. While both glasses and jammed packings behave elastically on small time scales and are disordered, the latter rely on specific geometrical constraints [55].

From a theoretical point of view, liquid state theory aims to characterise the emerging macroscopic properties of a liquid from a simple microscopic model for its particles, most often spherical particles which interact via conservative isotropic forces and which are subject to thermal excitation [56]. This approach thus takes its roots in statistical physics. In these models there is an inherent competition between *crowding*, *i.e.* how strongly does the interaction potential keep particles from overlapping, and *forcing*, *i.e.* how strongly does the driving (which can be external such as shear, or internal such as thermal motion) make particles overlap. This competition is well encapsulated in the concept of *potential energy landscape* [57]. The latter is the surface defined by the function which attributes the interaction potential energy to a set of coordinates in the system. Therefore to each configuration corresponds an unique point on this surface. This representation is convenient because the properties of the system are well described, in the supercooled regime close to the glass transition, by the sole sets of local minima of this surface (*i.e.* force-balanced configurations) and transition paths (or *barriers*) between them [57]. *Structural relaxation* is the process by which the system, starting from a given initial configuration, explores the potential energy landscape and eventually loses memory of its original configuration. This process happens through a succession of barrier crossings, where local structures *rearrange*, and over a time scale known as the *relaxation time*. When forcing overcomes crowding the system crosses the barriers easily and particles freely diffuse. On the contrary, if crowding overcomes forcing, which is the case close to the glass transition, the system rarely experiences transitions through barriers.

In the case of systems subject to thermal excitation, these rearrangements happen through *rare activated events*. Their rate thus decreases with decreasing temperature, which in turn increases the relaxation time. At low enough temperature, the system is effectively trapped in a metastable configuration and is unable to explore the potential landscape, especially more probable (*i.e.* less energetic) configurations: it thus breaks detailed balance and falls out of equilibrium. In this regime, a small decrease of the temperature (of the order of a few percent) amounts to a large increase of the relaxation time (of several orders of magnitude). The relaxation time eventually exceeds all accessible experimental time scales, leaving the system dynamically arrested.

In the case of sheared amorphous systems, the mechanism for transition through barriers is different. Specifically, athermal systems may be sheared quasistatically [58]: an infinitesimal shear transformation is applied to the system and the system is left to relax to a force-balanced configuration. In this case, rather than thermal hopping through barriers, the metastable state of the system is destabilised by the shear transformation, and a small localised rearrangement follows. Because of elasticity, the effects of this local change are felt far from the rearrangement, which in turn causes other cascading rearrangements. This phenomenon is known as an *avalanche*.

Beside dynamical slowdown, an important hallmark of supercooled liquids is *dynamical heterogeneity* [54, 59]. In the supercooled regime, the rate of rearrangement of local structures is not homogeneous in space as it would be in normal liquids. A mapping of the regions where rearrangements occurred during a time lapse of the order of the relaxation time shows that these regions are clustered together: there are on the one hand large fast regions of the system where multiple rearrangements took place and on the other hand equally large slow regions which kept their initial structure. These non-trivial spatiotemporal fluctuations become more pronounced as the glass transition is approached. This is a form of disordered collective motion which is common to other crowded disordered systems, *e.g.* jammed granular materials under shear [60, 61] and spin glasses [62]. This resemblance raises questions about the possible common mechanisms with which these systems explore their potential energy landscape [63]. Describing and rationalising the emergence of dynamical heterogeneities has thus been a central problem in glass physics research [52] as their seemingly universal nature provides an essential test for various theories of the glass transition, *e.g.* mode-coupling theory [64], random first-order transition theory [65], and

dynamical facilitation approach [66].

There has been an interest over the last two decades on the glassy behaviour of active systems [67]. In particular, dense bacterial suspensions [68] and confluent cell tissues [27, 69] have attracted specific attention, due to the combination of both large densities and wide variety in individual particles' (in this case, cells) sizes which promotes glass formation in equilibrium systems. The dynamics of confluent monolayers of MDCK cells, for example, was shown to slow down with increasing density, and also displays dynamical heterogeneity, similarly to equilibrium systems [69]. This behaviour is intriguing on numerous aspects. First, it raises the question of whether biological organisms may use glass-like properties to perform actions, or if these properties emerge in specific conditions [70, 71]. In the latter case, this would mean that tools and concepts developed in the context of condensed matter physics may be applied to biological systems in order to characterise them. Second, from a physical point of view, this highlights even further that dense and disordered systems have common properties and behaviour, irrespectively of their forcing mechanism. Thus, progresses on the understanding of the relaxation of active glasses may inform the way passive glasses relax.

These questions have motivated the development of diverse theoretical tools [72, 73], numerical models [34, 74], and, only very recently, synthetic experimental systems [12, 13], with which active glassy dynamics may be studied. Among these, simple models of spherical particles subject to self-propulsion forces have been extensively studied [75–82]. The great interest in these models may be attributed in part to their close resemblance to equilibrium numerical models of glasses, which thus enables to use similar observables in order to characterise their dynamics and fluctuations. A first major breakthrough was to show that these systems, in which thermal fluctuations are replaced or supplemented by active driving, still exhibited dynamical slowdown: at small temperature and small propulsion strength [80, 83], and, in the absence of thermal fluctuations, at large packing fractions and small propulsion strength [77, 78]. More surprisingly, even though one could naively expect that driving would delay if not destroy the glass transition [84], the use of persistent active driving was shown in some cases to promote it [81]. Finally, dense active systems were shown to also display strong dynamical heterogeneities, and that these become increasingly important as the glass transition is approached [79, 81, 82].

From these observations, different theories for the equilibrium glass transition were adapted to take into account active driving, among them mode-coupling theory [73, 78, 85, 86] and random first-order transition theory [83, 87]. These theories have been quite successful at small persistence time, close to the equilibrium limit [78, 83], but significant deviations were reported far from equilibrium [83]. It was pointed out early that non-equilibrium instantaneous velocity correlations may have a role to play in the slow relaxation of dense active matter [78, 81], yet its role has remained elusive. In addition, the striking resemblance between the velocity fields in dense yet frozen active matter [88] and the dynamical heterogeneities described in dense cell tissues [69] questions further the relation between these non-equilibrium correlations and the relaxation mechanisms of dense active systems. An understanding of the relaxation of active glasses therefore necessitates a fine characterisation of the emergence of collective motion in active systems.

1.5 Turbulence

Liquids present a variety of composition at the microscopic level. It is the case for pure solutions, from the simple three-atom molecules of water to the long carbon chains of lipids, and even more striking for complex solutions like coffee or wine. Despite this microscopic variety, these solutions display similar macroscopic behaviours. This suggests a description of the fluid at an intermediate *mesoscopic* level, at which the microscopic details do not matter.

At this level, the time evolution of the velocity in a viscous fluid is well described by the deterministic Navier-Stokes equation. This equation, despite being almost two-centuries old and of paramount importance in theoretical and practical applications, has no known exact solution and its numerical solving is also difficult in some specific cases. This difficulty comes from its non-linearity, embedded in its convective inertia term. The Reynolds number quantifies the importance of inertial forces with respect to viscous forces. At low Reynolds number, the flow is well described by the (linear) Stokes equation: it is laminar, *i.e.* flow particles follow smooth paths. On the contrary, at high Reynolds number, when inertial effects dominate, the flow is *turbulent* [89]. In this case, the flow is characterised by chaotic changes in the velocity, and unsteady vortices (or *eddies*) on many different length scales. These eddies play a fundamental role, they are formed at large length scales then, because they are unstable, separate in eddies on smaller length scales which inherit the kinetic energy of the larger eddies. This process continues again until these eddies reach a sufficiently small scale at which viscosity is able to dissipate this energy. This transfer of energy from the large to the small scales is known as a *kinetic energy cascade*.

A great leap forward in the understanding of turbulence was Kolmogorov's theory of 1941, nicknamed K41

[90]. This theory postulates that, at very large Reynolds number, the statistics of the flow is isotropic and universal across scales, in between the large length scale where the eddies are formed and the small length scale at which energy is dissipated, and only depends on the fluid viscosity and its energy dissipation range. This range of scales, called the inertial range, may be several orders of magnitude large. It is a powerful theory, first because it leads to some accurate predictions, for example for the distribution of kinetic energy across length scales, and then because it underlies that many different fluid systems obey the same universal behaviours.

Active systems also display irregular and multiscale flows, *e.g.* bacterial swarms [91, 92], dense epithelial tissues [7], and suspensions of microtubules and kinesin motors [28, 93], which all show intermittent swirling motion. The term *active turbulence* [94] is then becoming increasingly popular to describe these chaotic mesoscale flows within these various anisotropic active systems. Unlike classical turbulence, active turbulence is observable in the absence of inertia, *i.e.* at exactly zero Reynolds number. Moreover, the energy injection is not externally imposed but self-generated at small scales [94].

Is active turbulence as universal as inertial turbulence? Or, at least, can its different models be organised in subclasses with universal properties? In equilibrium statistical mechanics, close to critical points, universal properties are known to emerge among systems which share the same symmetries [95]. Thus, a first step to answer these questions may reside in a classification of active turbulence models with respect to their symmetries, which is the path followed in a recent review on the subject [94]. First, the symmetry of the anisotropic active driving, which may be either nematic or polar. Then, the system will be considered *wet* if it conserves momentum, for example if hydrodynamic interactions dominate, and *dry* if it does not. There are thus 4 classes: wet nematic, dry nematic, wet polar, and dry polar. On the one hand, in nematic systems [96–98] flow derives in both wet and dry conditions from an instability in the dynamics of the nematic director field, with an emerging length scale determined by the balance between active and nematic stresses [96, 98]. On the other hand, most studies of polar active turbulence have either considered wet systems of swimmers [99], or the Toner-Tu-Swift-Hohenberg equation [100, 101], which describes incompressible flows in dry systems. It is noteworthy that in the latter equation there is no distinction between the active force and the velocity, which is exact *e.g.* in the absence of steric interactions. Among these classes, only wet nematic active turbulence was shown to display universal scaling behaviour of the distribution of kinetic energy across length scales [98], similarly to Kolmogorov's law.

May isotropic active systems also support active-turbulent flows? It was suggested [34] that dry isotropic self-propelled particles, in the limit of large density and persistence at which mesoscale velocity correlations emerge, displayed swirling motion with strong similarities with active turbulence in anisotropic systems [100, 102]. There already are hydrodynamic theories describing velocity correlations in these models [103, 104], and these already show that details of the self-propulsion mechanism and of the interparticle interactions are irrelevant, suggesting some sense of universality. However it is yet unknown how or if these theories would capture active-turbulent behaviour. Finally, these theories rely on both elasticity and an independence between positions and propulsions, which is not captured by the classification of Ref. [98].

1.6 Overview

Dense active matter challenges our understanding of condensed matter, from their phase behaviour, to their microscopic relaxation and emerging macroscopic flow. In particular, far from equilibrium, there is mounting evidence that activity is at the origin of complex collective behaviours, in a range of packing fractions going from the fluid to the glass or the crystal [34–37]. The mechanisms for these behaviours are not all uncovered, which makes the work of establishing possible universality classes extremely difficult.

In this Thesis, using a single generic model of self-propelled particles, we provide a framework in which various manifestations of coherent movement can be observed and studied. We will seek to answer the following question: *how does collective motion emerges from the competition between crowding and persistent forcing in isotropic active systems?*

In Chap. 2 we introduce our model: its definition, its control parameters, its characteristic scales, and will review the literature on similar (equilibrium and nonequilibrium) models. This review will enable us to introduce the main quantities at our disposal to describe the structure and the dynamics of our model.

In Chap. 3 we build the phase diagram of our model, in the space spanned by its control parameters. This diagram shows that a disordered liquid exists up to very large persistence, *i.e.* far from equilibrium, we will concentrate our efforts in this specific regime.

In Chap. 4 we study the microscopic relaxation in this persistent liquid on its path to dynamical arrest. We show that this relaxation dynamics is fundamentally different from the structural relaxation in equilibrium liquids, yet our system also displays disordered collective motion in the form of dynamical heterogeneity.

In Chap. 5 we introduce a quasistatic method which approximates the dynamics in the limit of infinite

persistence. This technique enables us to uncover how dynamical heterogeneity is built in this idealised limit.

In Chap. 6, we show that a fine tuning of the control parameters enables us to reproduce active turbulence, despite the absence of couplings between propulsion forces. A careful analysis of our system in this regime shows that it does not fit the existing classification of active-turbulent systems. We provide evidence that it belongs to a new and unexplored class.

Finally, in Chap. 7, we set the system in order to observe structurally ordered phases. We introduce in this case the relevant structural and dynamical length scales, and their possible relations.

We gather our conclusions in Chap. 8.

2 | Active Ornstein-Uhlenbeck particles

We introduce in this Chapter the model of self-propelled particles we will consider in this Thesis, namely active Ornstein-Uhlenbeck particles (AOUPs). We will then review the literature on the structural and dynamical properties of this model at large density and/or large persistence. We will finally conclude with a brief discussion of the length and time scales involved in the flow of these particles and the associated emerging phenomena.

Contents

2.1 Model definition and properties

We want to keep the model as simple as possible so as to highlight the precise origin of physical behaviours. Self-propelled particles have few control parameters yet display complex emerging phenomena.

2.1.1 Definition of active Ornstein-Uhlenbeck particles

We start from the equation of motion in time t of a single particle i, in two dimensions (2D), subjected to a drag force and a propulsion force

$$m\ddot{\boldsymbol{r}}_i = -\xi\dot{\boldsymbol{r}}_i + \boldsymbol{p}_i \tag{2.1}$$

where m is its mass and ξ a viscous damping coefficient. By convention we note $\dot{r} \equiv \mathrm{d}r/\mathrm{d}t$ and $\ddot{r} \equiv \mathrm{d}^2r/\mathrm{d}t^2$ the first and second derivative of r with respect to time t. We introduce $\hat{\boldsymbol{z}}$ an unit vector orthogonal to the plane of the motion. In the following, we will only consider overdamped dynamics and neglect the inertial term on the left hand side. Therefore the drag force will exactly compensate all the other forces

$$\xi\dot{\boldsymbol{r}}_i = \boldsymbol{p}_i. \tag{2.2}$$

This hypothesis is very generic in the description of soft matter systems and in particular dense cell tissues [5, 35].

The specific choice of the propulsion forces evolution $\boldsymbol{p}_i$ is the defining feature of the model of self-propelled particles [105]. We choose to have $\boldsymbol{p}_i$ follow an Ornstein-Uhlenbeck process [106]

$$\tau_p\dot{\boldsymbol{p}}_i = -\boldsymbol{p}_i + \sqrt{2\xi^2 D_0}\boldsymbol{\eta}_i \tag{2.3}$$

where $\boldsymbol{\eta}_i$ is a zero-mean Gaussian white noise with variance

$$\left\langle \boldsymbol{\eta}_i(0)\boldsymbol{\eta}_j(t)\right\rangle = \mathbb{1}\delta_{ij}\delta(t), \tag{2.4}$$

where the angular brackets $\langle\cdots\rangle$ denote a time average taken over different initial times 0 in the steady-state dynamics, $\mathbb{1}$ is the identity matrix, δ_{ij} is the Kronecker delta, and $\delta(s)$ is the Dirac delta function. We call the particles subjected to this force *active Ornstein-Uhlenbeck particles* (AOUPs) [107–109].

Different choices can be made for the propulsion forces $\boldsymbol{p}_i$ evolution. Another common model is *active Brownian particles* (ABPs) [110], for which

$$\boldsymbol{p}_i = \xi v_0 \begin{pmatrix}\cos\theta_i \\ \sin\theta_i\end{pmatrix} \tag{2.5a}$$

$$\dot{\theta}_i = \sqrt{2/\tau_p}\,\eta_i \tag{2.5b}$$

where η_i is a zero-mean Gaussian white noise with variance $\langle\eta_i(t)\eta_j(t')\rangle = \delta_{ij}\delta(t-t')$, and therefore $\boldsymbol{p}_i$ also have fluctuations described by (2.7). While there are some differences at the single-particle level [111], we do not expect significant differences for the regimes of large persistence and density which we are investigating [33, 86].

2.1.2 Properties and scales for free AOUPs

It follows from equation (2.3)

$$\boldsymbol{p}_i(t) = \boldsymbol{p}_i(0)e^{-t/\tau_p} + \int_0^t \mathrm{d}s\,\sqrt{2\xi^2 D_0/\tau_p^2}\,\boldsymbol{\eta}_i(s)e^{-(t-s)/\tau_p} \tag{2.6}$$

and in the steady state [106]

$$\left\langle \boldsymbol{p}_i(t)\cdot\boldsymbol{p}_j(t')\right\rangle \underset{t,t'\to\infty}{\sim} \delta_{ij}(2D_0/\tau_p)e^{-|t-t'|/\tau_p} \tag{2.7}$$

$$\mathrm{Prob}(\boldsymbol{p}_i) = \tfrac{1}{2\pi(D_0/\tau_p)}\exp\left(-\tfrac{1}{2(D_0/\tau_p)}|\boldsymbol{p}_i|^2\right) \tag{2.8}$$

and thus the equation of motion for the free particle (2.2) lays the following mean squared displacement (MSD)

$$\left\langle|\boldsymbol{r}_i(t)-\boldsymbol{r}_i(0)|^2\right\rangle \underset{\text{free}}{=} 4D_0\tau_p(t/\tau_p + (e^{-t/\tau_p}-1)) \tag{2.9}$$

which is ballistic at small times

$$\left\langle|\boldsymbol{r}_i(t)-\boldsymbol{r}_i(0)|^2\right\rangle \underset{\substack{t\to 0\\ \text{free}}}{\sim} 2v_0^2t^2,\ v_0 = \sqrt{D_0/\tau_p} \tag{2.10}$$

where v_0 defines the free-particle self-propulsion velocity, and diffusive at large times

$$\lim_{t\to\infty}\frac{\left\langle|\boldsymbol{r}_i(t)-\boldsymbol{r}_i(0)|^2\right\rangle}{t} \underset{\text{free}}{=} 4D_0 \tag{2.11}$$

where D_0 defines the free-particle self-diffusion constant. As an integrated Ornstein-Uhlenbeck process [112], we can show that the displacements of a free particle are also normally distributed.

This definition of the propulsion forces $\boldsymbol{p}_i$ enforces a Gaussian force (2.8), which has a characteristic amplitude ξv_0 and an autocorrelation time τ_p (2.7, 2.10). We also define the persistence length

$$\ell_p = v_0\tau_p = \sqrt{D_0\tau_p} \tag{2.12}$$

which is the typical distance travelled by a free particle before losing memory of its original velocity. The dimensionless persistence length

$$\widehat{\mathrm{Pe}} = \ell_p/\sigma \tag{2.13}$$

is sometimes referred to as the Péclet number [49, 113].

For $\tau_p = 0$, Eq. (2.3) gives $\boldsymbol{p}_i = \sqrt{2\xi^2 D_0}\boldsymbol{\eta}_i$, and thus Eq. (2.2) describes the Brownian motion of a free particle at equilibrium with a thermal bath at temperature $k_\mathrm{B}T = \xi D_0$. For any $\tau_p > 0$, $\boldsymbol{p}_i$ is a coloured noise which is not compensated by a corresponding coloured generalised drag force. This is a violation of the second fluctuation-dissipation theorem [114], and the system is out-of-equilibrium [22].

2.1.3 Definition and scales of the interacting system

We consider systems of N AOUPs, in a periodic square box of linear size L, with diameters σ_i. Particles interact through a pairwise additive potential U, which is a function of the positions $\boldsymbol{r}_i$ and diameters σ_i of the particles, and we will denote $-\nabla_i U$ the force exerted on particle i by all other particles. By convention we note $\nabla_i \equiv \partial/\partial \boldsymbol{r}_i \equiv \partial_{\boldsymbol{r}_i}$ the partial derivative with respect to position $\boldsymbol{r}_i$. We introduce ε the characteristic energy scale of the potential U. We set the units of length, time, and energy respectively to

$$\sigma = \frac{1}{N}\sum_{i=1}^{N}\sigma_i = 1,\ \tau_0 = \xi\sigma^2/\varepsilon = 1,\ \varepsilon = 1 \tag{2.14}$$

where the mean diameter σ sets the typical length between two particles in a dense system, the interaction time scale τ_0 is the relaxation time for a system of two particles interacting via a harmonic potential of strength ε and thus sets the typical time scale of evolution of two-particle interaction forces, and the potential parameter ε sets the typical interaction energy between two particles. With these we write the dimensionless equations of our model

$$\dot{\boldsymbol{r}}_i = -\nabla_i U + \boldsymbol{p}_i \tag{2.15}$$

$$\tau_p \dot{\boldsymbol{p}}_i = -\boldsymbol{p}_i + \sqrt{2D_0}\boldsymbol{\eta}_i \tag{2.16}$$

which, besides the choice of the potential U and the distribution of the σ_i, has 4 control parameters: the number of particles N, the number density $\rho = N/L^2$, the free-particle self-diffusion constant D_0, and the persistence time τ_p.

We will restrict our study to purely repulsive soft interaction potentials U which diverge at distance $r = 0$. We expect our results to be robust to the specific choice of potential U, as long as it matches these criteria. We will mainly use the Weeks-Chandler-Andersen (WCA) potential

$$U = \sum_{i>j} U_{ij} \tag{2.17a}$$

$$U_{ij} = 4\varepsilon\left[\left(\frac{\sigma_{ij}}{r_{ij}}\right)^{12} - \left(\frac{\sigma_{ij}}{r_{ij}}\right)^{6} + \frac{1}{4}\right]\Theta(2^{1/6}\sigma_{ij} - r_{ij}) \tag{2.17b}$$

where $r_{ij} = |\boldsymbol{r}_j - \boldsymbol{r}_i|$, $\sigma_{ij} = (\sigma_i + \sigma_j)/2$, and Θ is the Heaviside step function.

We will consider systems for which diameters σ_i are drawn from a uniform distribution of mean $\overline{\sigma_i} = \sigma = 1$, and the polydispersity index

$$I = \sqrt{\overline{(\sigma_i - \overline{\sigma_i})^2}}/\overline{\sigma_i} \tag{2.18}$$

is either $I = 0$ (monodisperse) or $I = 20\%$ (polydisperse). We chose this specific value of I for polydisperse systems such that we do not observe crystallisation in the range of other parameters we have studied. We would expect weak dependence of the dynamics on I or the shape of the distribution as long as the system does not crystallise.

We introduce the packing fraction

$$\phi = 2^{1/3}\frac{\pi N\overline{\sigma_i^2}}{4L^2} = 2^{1/3}\frac{\pi\overline{\sigma_i^2}}{4}\rho \tag{2.19}$$

which is proportional to the number density ρ.

It is noteworthy that the centre of mass of the system moves at the velocity

$$\overline{\boldsymbol{V}} = \frac{1}{N}\sum_i \dot{\boldsymbol{r}}_i = \frac{1}{N}\sum_i \boldsymbol{p}_i \tag{2.20}$$

where the second equality derives from Newton's third law. Throughout this Thesis, we will only consider movements with respect to the centre of mass. In this frame, we denote

$$\boldsymbol{v}_i = \dot{\boldsymbol{r}}_i - \overline{\boldsymbol{V}} \tag{2.21}$$

each particle's velocity.

2.2 Numerical integration

We first need to provide an initial configuration. If we do not already have one, we create one by placing particles on a regular triangular lattice and then assigning them a random diameter in the distribution corresponding to the polydispersity index I. We then use the FIRE algorithm [115, 116] to minimise particle overlaps.

When particles are crowded or when they move fast towards each other, a simple first-order integration scheme (such as Euler method) is not adopted since the WCA potential is very steep. We use Heun's method [117–119] to improve stability. We denote δt the integration time step. From a given set of initial positions $\{\boldsymbol{r}_1^0, \dots, \boldsymbol{r}_N^0\}$ and initial propulsions $\{\boldsymbol{p}_1^0, \dots, \boldsymbol{p}_N^0\}$, the algorithm first computes a Euler integration of Eqs. (2.15, 2.16)

$$\boldsymbol{r}_i^* = \boldsymbol{r}_i^0 + \delta t \left[-\nabla_i U(\{\boldsymbol{r}_1^0, \dots, \boldsymbol{r}_N^0\}) + \boldsymbol{p}_i^0 \right], \tag{2.22}$$

$$\boldsymbol{p}_i^* = \boldsymbol{p}_i^0 - (\delta t/\tau_p)\boldsymbol{p}_i^0 + \sqrt{2\,\delta t\, D_0/\tau_p^2}\,\tilde{\boldsymbol{\eta}}_i, \tag{2.23}$$

where $\tilde{\boldsymbol{\eta}}_i = (\tilde{\eta}_{i,x}, \tilde{\eta}_{i,y})$ are two random numbers drawn for a normal distribution with zero mean and unit variance. The algorithm then uses these first estimations to re-compute the forces and correct the step

$$\boldsymbol{r}_i = \boldsymbol{r}_i^* + \frac{\delta t}{2}\left[-\nabla_i U(\{\boldsymbol{r}_1^*, \dots, \boldsymbol{r}_N^*\}) + \nabla_i U(\{\boldsymbol{r}_1^0, \dots, \boldsymbol{r}_N^0\}) \right] + \frac{\delta t}{2}\left[\boldsymbol{p}_i^* - \boldsymbol{p}_i^0 \right], \tag{2.24}$$

$$\boldsymbol{p}_i = \boldsymbol{p}_i^* - \frac{\delta t/\tau_p}{2}\left[\boldsymbol{p}_i^*/\tau_p - \boldsymbol{p}_i^0/\tau_p \right]. \tag{2.25}$$

Hence, the most computationally heavy step which is computing the forces has to be done twice per iteration. In order to speed this up, we implement a cell list [120]. Our simulation scripts are written in C++ and are available under the MIT license [121].

We want to characterise the steady state of the system. This is done by checking that time averages $\langle \dots \rangle$ do not depend on the initial time taken in the average.

We chose the integration time step δt small enough such that the integration procedure remains stable and the steady-state averages do not depend on its value.

2.3 Phase description of interacting AOUPs

We will review in this Section the main results on the phase behaviour of monodisperse and polydisperse systems of self-propelled particles. It is noteworthy that in dense and disordered passive systems, dramatic dynamical changes can happen without similarly dramatic changes in the structure [122]. Moreover, because self-propelled particles are out of equilibrium, there is *a priori* no reason why the structure would dictate the dynamics of the system [49, 51]. Our review will thus address the two following fundamental questions about the system separately.

1. Is it structurally ordered?
2. Does it flow easily?

We will provide the essential quantities and concepts to tackle these questions.

2.3.1 Is it structurally ordered?

We have to first distinguish homogeneous phase from phase-separated states, and then in homogeneous phases distinguish those which are ordered from those which are not.

2.3.1.1 Motility-induced phase separation

Assemblies of interacting disks at equilibrium are able, in the presence of attractive interactions, to phase separate between a macroscopic dense phase and a macroscopic dilute phase [123]. This phenomenon is known as liquid-gas phase separation. The resulting heterogeneity in density can be characterised by computing the local packing fraction [109, 113, 124]

$$\phi_{\mathrm{loc}}(\boldsymbol{r}, a) = \frac{1}{a^2}\sum_{i=1}^{N} \frac{\pi}{4}(2^{1/6}\sigma_i)^2 \Theta(a - |r_{i,x} - r_x|)\Theta(a - |r_{i,y} - r_y|) \tag{2.26}$$

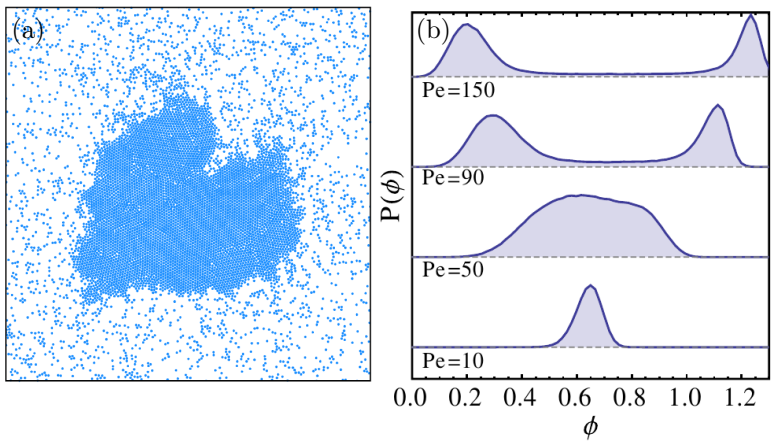

Figure 2.1: (a) Snapshot of a phase-separated system. Taken from Ref. [22], Fig. 1. The system is athermal AOUPs with $D_0 = 100$ and $\tau_p = 20$. (b) Distribution of local packing fraction ϕ_{loc} for different Péclet number $\text{Pe} = 3\widehat{\text{Pe}}$ (2.13) at fixed global packing fraction $\phi = 0.65$. Taken from Ref. [49], Fig. 2(b). The system is thermal ABPs, interacting via a WCA potential. Persistence time is fixed $\tau_p = \tau_0/3$ and self-propulsion velocity v_0 is varied.

which is the packing fraction in a square box of size a centred around $\boldsymbol{r}$.

Using a purely repulsive potential (such as WCA (2.17)), it should be impossible to observe liquid-gas coexistence at equilibrium. Far from equilibrium, because of persistent self-propulsion forces, it is possible for active systems to phase separate, creating a dense macroscopic cluster surrounded by a dilute gas. This phenomenon is known as *motility-induced phase separation* (MIPS) [1]. Persistent particles colliding head-on are able to arrest each other [125, 126] and can escape this situation only when propulsion forces change, which happens on the time scale τ_p [127]. This behaviour can be translated as persistence-induced effective attractive forces [22, 126, 128], however these forces are not sufficient to trigger phase separation and multi-particle effects have to be taken into consideration [128]. At sufficient density, if the time for particle to come in contact with new particles is much smaller than the time to change their propulsions, which implies large persistence length ℓ_p (2.12) with respect to the interparticle distance, then particles accumulate, forming dense clusters which grow with time [129].

Fig. 2.1 shows results from Refs. [22, 49] which consider AOUPs and ABPs respectively. In both of these systems, MIPS is observed at large persistence and moderate packing fraction. This transition is apparent in the distribution of local packing fraction ϕ_{loc} (2.26) (Fig. 2.1(b)). While this distribution is unimodal at small persistence length ($\text{Pe} = 10$ in Fig. 2.1(b)), indicating a homogeneous phase, it is bimodal ($\text{Pe} \geq 90$ in Fig. 2.1(b)) at large persistence length, indicating a phase-separated state [49, 113, 124]. Moreover, the positions of the local maxima of the distribution of ϕ_{loc} do not depend on the global packing fraction ϕ [49, 109], these maxima can then be used to delimit the phase-separated region in phase space.

2.3.1.2 Orientational and translational structure

In three dimensions and above, disordered passive liquids have a first-order transition to ordered (crystalline) solids at low temperatures [130, 131]. In two dimensions, this solidification is a two-step process, where long-range orientational order emerges before quasi-long-range translational order [44]. Characterising the order range of these fields necessitates to compute the correlations (*i.e.* fluctuations) of the orientational and density field respectively. Short-ranged correlations will be associated with exponential decays to 0 of these correlation functions, while quasi-long-ranged correlations are associated with algebraic (*i.e.* power-law) decay to 0. In the case of long-range correlations, these do not decay to 0 at infinite distance.

Orientational order refers to the ordering of bonds between neighbouring particles. In a perfectly ordered solid, a given particle i has 6 neighbours $j \in \{1, \dots, 6\}$, which are located at equal distance and at angles

$$\theta_{j,i} = \frac{2\pi}{6} j + \theta_0 \tag{2.27}$$

where θ_0 corresponds to the orientation of the crystal with respect to some reference axis. Therefore we can quantify the orientational order around particle i with the (complex) hexatic order parameter [46, 51, 132] or

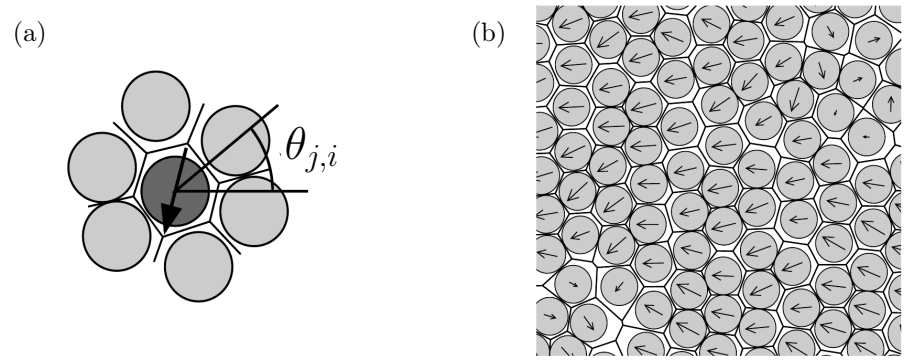

Figure 2.2: (a) Local orientation bond-order parameter orientation $\arg(\psi_{6,i})$. (b) Orientational field of a hard-disk configuration. Taken from Ref. [43], Fig. 3.3.

orientational field

$$\psi_{6,i} = \frac{1}{z_i} \sum_{j=1}^{z_i} \exp(\mathrm{i}6\theta_{j,i}) \tag{2.28}$$

where z_i is the number of nearest neighbours of i by Voronoi tesselation, and $\theta_{j,i}$ is the angle between the vector going from particle i to its j-th neighbour and a reference axis. Therefore, if i has exactly six neighbours with orientations (2.27) then

$$\psi_{6,i} = \exp(\mathrm{i}6\theta_0) \tag{2.29}$$

which modulus is 1, indicating perfect order, and argument is $6\theta_0$, indicating the local orientation [43] (Fig. 2.2). There exists an equivalent indicator in 3D [133, 134].

In order to distinguish a liquid (disordered) from an hexatic (orientationally ordered) or a solid phase (translationally and orientationally ordered) it is necessary to compute the hexatic order parameter correlation function

$$C_{\psi_6\psi_6}(r) = \left\langle \frac{\sum_{i,j=1}^{N} \psi_{6,i}\psi_{6,j}^{*}\delta(r - |\boldsymbol{r}_i - \boldsymbol{r}_j|)}{\sum_{i,j=1}^{N} \delta(r - |\boldsymbol{r}_i - \boldsymbol{r}_j|)} \right\rangle, \tag{2.30}$$

which decays exponentially in the liquid phase, algebraically in the hexatic phase [46], and remains non-zero over large distances in the solid phase [43].

To characterise translational order, we resort to the pair distribution [132]

$$g(\boldsymbol{r}) = \frac{L^2}{N^2} \sum_{i=1}^{N} \sum_{j \neq i} \langle \delta(\boldsymbol{r} - (\boldsymbol{r}_j - \boldsymbol{r}_i)) \rangle \,, \tag{2.31}$$

which is non-isotropic for ordered crystalline phases [44]. In these phases, the projection of $|g(\boldsymbol{r}) - 1|$ in a given direction decays algebraically, and exponentially in translationally disordered phases [44]. In the liquid, $g(\boldsymbol{r})$ is isotropic [132] and we will compute

$$g(r) = \frac{1}{2\pi r} \frac{L^2}{N^2} \sum_{i=1}^{N} \sum_{j \neq i} \langle \delta(r - |\boldsymbol{r}_j - \boldsymbol{r}_i|) \rangle \tag{2.32}$$

the *radial* pair distribution function. This function derives from the spatial correlations of the density field and thus provides the unnormalised probability to find another particle at a distance $r > 0$ away from any particle [132]. We introduce the Fourier space equivalent of the pair distribution function, the static structure factor

$$S(\boldsymbol{k}) = \frac{1}{N} \sum_{i,j=1}^{N} \langle \exp\left(-\mathrm{i}\boldsymbol{k} \cdot (\boldsymbol{r}_j - \boldsymbol{r}_i)\right) \rangle = 1 + \rho \int \mathrm{d}\boldsymbol{R} \, \exp(-\mathrm{i}\boldsymbol{k} \cdot \boldsymbol{R}) g(\boldsymbol{R}), \tag{2.33}$$

which quantifies the fluctuation of the density field on the length scale $\lambda = 2\pi/k$ [132], and is related to the pair distribution function g via Fourier transform. We assume isotropy so that we can replace $S(\boldsymbol{k})$ by its average value $S(k)$ over all different orientations of the vector $\boldsymbol{k}$ ($|\boldsymbol{k}| = k$). In practice, we average over vectors $\boldsymbol{k} = (2\pi m/L, 2\pi n/L)$ such that $m, n \in \mathbb{Z}, |\boldsymbol{k}| \in [k - \delta k/2; k + \delta k/2]$ with $\delta k = 0.1$. The first peak of $S(k)$ is at

$$k^* = 2\pi/r_{\mathrm{nn}} \tag{2.34}$$

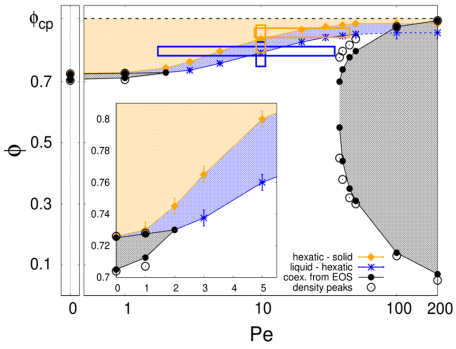

Figure 2.3: Phase diagram at fixed persistence time τ_p (Pe $\sim v_0$) of monodisperse thermal ABPs interacting via a purely repulsive 64-32 Lennard-Jones potential. Taken from Ref. [46], Fig. 1.

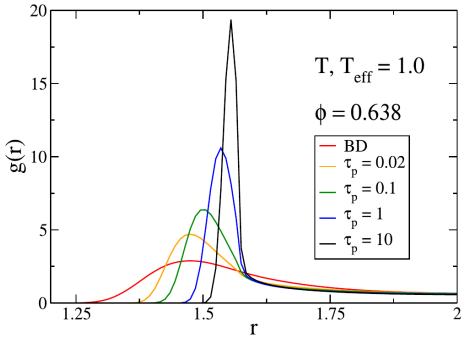

Figure 2.4: Pair distribution function $g(r)$ (2.32) for different persistence times τ_p at fixed packing fraction ϕ and free-particle self-diffusion constant $D_0 = T_{\text{eff}}$. The red line (BD) corresponds to a Brownian system at temperature $T = 1.0$. Taken from Ref. [82], Fig. 6(b) (also Ref. [81], Fig. 5(a)).

where r_{nn} corresponds to the typical distance of the nearest neighbour [132]. This distance in dense systems is usually of the order $r_{\text{nn}} \sim 1$.

These tools allow to build phase diagrams for monodisperse [46, 88] and polydisperse [76] systems. Models of self-propelled particles such as ours have three control parameters in the thermodynamic limit $N \to \infty$, therefore drawing a two-dimensional phase diagram necessitates to choose a cut through the phase space. Previous works have established, for monodisperse ABPs interacting via purely repulsive potentials, the phase diagram at fixed self-propulsion velocity v_0 (Ref. [88], Fig. 1(a)) and at fixed persistence time τ_p [46] (Fig. 2.3). For polydisperse ABPs, the phase diagram at fixed persistence time τ_p was drawn (Ref. [76], Fig. 2), and we will build later the phase diagram for AOUPs at fixed free-particle self-diffusion constant D_0. At low persistence and packing fraction, all models have disordered liquid phases, where fluctuations of both the orientational field (2.30) and the density field (2.32) decay exponentially. At large packing fraction, monodisperse models first experience a transition from the disordered liquid to an hexatic phase where fluctuations of the orientational field decay algebraically, and then to a solid phase where fluctuations of the density field decay algebraically [46]. All models (both monodisperse and polydisperse) exhibit MIPS at large persistence. Moreover, in monodisperse models at large persistence, the dense cluster of the phase-separated system is either hexatic or solid, consistently with Ref. [49]. In the polydisperse model, at small persistence and large packing fraction, the dynamics of the disordered liquid slows down dramatically and the system enters the disordered solid (glass) phase [76], which has to be characterised with dynamical quantities.

In homogeneous disordered phases, the structure is affected by the persistence time τ_p of the self-propulsion. Ref. [81] studies the glass transition in polydisperse AOUPs, and finds significant persistence-induced structural changes which affect this transition. Fig. 2.4 shows that, at constant free-particle self-diffusion constant D_0 and packing fraction ϕ, the first peak of the pair distribution function sharpens with increasing persistence time τ_p as well as shifts to larger distances. The sharpening of the peak informs us that there is an increased adhesion as particles are more persistently propelled against each other [81]. The shifting of the peak to larger distances is a consequence of decreasing self-propulsion velocity v_0 as τ_p is increased at fixed D_0: particles cannot penetrate as far into the interaction potential and thus appear stiffer [81]. Ref. [81] (Fig. 6(a)) shows in the meantime small variations in the positions of the peaks of the structure factor $S(k)$. Since the packing fraction ϕ is kept constant, we indeed do not expect large variations in the typical distance of the nearest neighbour.

2.3.2 Does it flow easily?

Knowing how the system flows amounts to quantifying the length and time scales over which the particles move, and the heterogeneities in these movements.

2.3.2.1 Cage escape and relaxation

Movements of the particles are described by their displacements over a time t

$$\Delta \boldsymbol{r}_i(t) = \begin{pmatrix} \Delta r_{i,x} \\ \Delta r_{i,y} \end{pmatrix} = \int_0^t \mathrm{d}s\, \boldsymbol{v}_i(s) \tag{2.35}$$

where the displacement of the centre of mass has been subtracted.

In order to characterise the typical length scale of the movement over a given time t, we compute the variance of the displacements, also known as mean squared displacement (MSD)

$$\mathrm{MSD}(t) = \frac{1}{N} \sum_{i=1}^{N} \left\langle |\Delta \boldsymbol{r}_i(t)|^2 \right\rangle , \tag{2.36}$$

which is linked to the velocity autocorrelation function

$$\mathrm{MSD}(t) = \frac{1}{N} \sum_{i=1}^{N} \int_0^t \mathrm{d}s \int_0^t \mathrm{d}s'\, \left\langle \boldsymbol{v}_i(s) \cdot \boldsymbol{v}_i(s') \right\rangle . \tag{2.37}$$

As for the free particle (2.10), the MSD increases as t^2 (ballistic) at small times

$$\mathrm{MSD}(t \to 0) \sim v^2 t^2, \; v^2 = \frac{1}{N} \sum_{i=1}^{N} \left\langle |\boldsymbol{v}_i(0)|^2 \right\rangle , \tag{2.38}$$

which indicates that, at small length and time scales, velocities have not decorrelated from their initial value. As for the free particle (2.11), it increases as t (diffusive) at large times

$$\mathrm{MSD}(t \to \infty) \sim 4Dt \tag{2.39}$$

where D defines the diffusion constant of the system, which indicates that, at large length and time scales, velocities have decorrelated from their initial value.

Ref. [77] studies how persistent self-propulsion affects the glass transition of hard-core thermal ABPs. Fig. 2.5(a) shows that at small packing fraction (top curve), the behaviour of the MSD is close to the free-particle limit (2.9), with the persistence time τ_p marking the crossover from the initial ballistic to the eventual

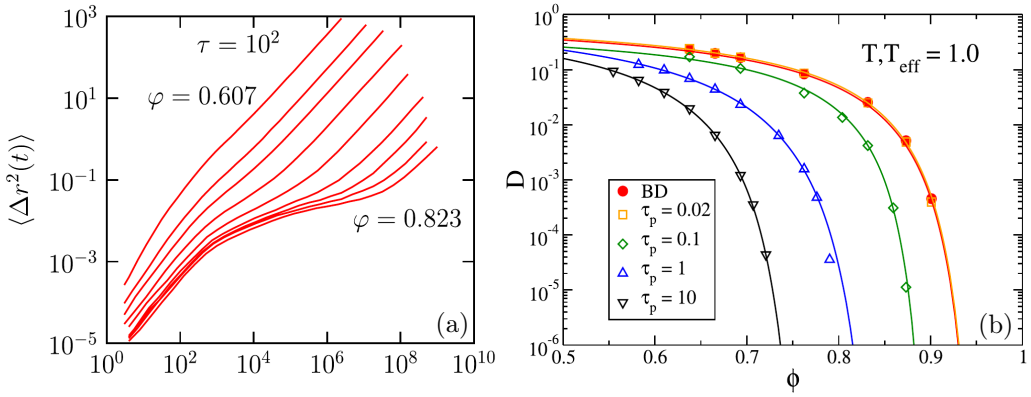

Figure 2.5: (a) Mean squared displacement $\mathrm{MSD}(t) = \left\langle \Delta r^2(t) \right\rangle$ as a function of time, for different packing fractions $\phi = \varphi$ increasing from top to bottom, at constant persistence time $\tau_p = \tau = 10^2$. Taken from Ref. [77], Fig. 1(b). The system is a Monte Carlo analogue of thermal ABPs with hard-core exclusion. (b) Effective diffusion constant D as a function of packing fraction ϕ, for different persistence times τ_p, at constant free-particle self-diffusion constant $D_0 = T_{\mathrm{eff}}$. The red line (BD) corresponds to a Brownian system at temperature $T = 1.0$. Taken from Ref. [81], Fig. 2(a). The system is athermal AOUPs interacting via a WCA potential.

diffusive regime. As the packing fraction ϕ increases (from top to bottom), there is the emergence and the stretching of an intermediate sub-diffusive regime, indicating that particles remain close to their initial position for an extended period of time after the decorrelation of their initial propulsion forces. This behaviour is known as *caging* in passive supercooled liquids [64, 77], and leads to a two-step relaxation scenario [132]: first particles explore and stay within the cage formed by their initial neighbours (β-relaxation), then particles escape their cage to relax the structure (α-relaxation). A consequence of this localisation of particles for longer periods of time as the packing fraction is increased is a drop in the effective diffusion constant D. This is the same effect at play in the AOUP model of Ref. [81] (Fig. 2.5(b)): at large packing fractions ϕ, for all persistence times considered, small variations of ϕ in linear scale lead to large variations of D on a logarithmic scale. As a consequence of the underlying non-equilibrium glass transition, the dynamics of the system is unable to relax its structure at large ϕ [81].

In the potential energy landscape picture, slowing down of the dynamics emerges from the existence of a large number of meta-stable states. At low temperatures, transitions between these happen through rare activated events, resulting in slow structural relaxation [53, 135]. Formally, it is temperature which drives this slowing down [136]. However, increasing the packing fraction also increases the height of the potential energy barriers the system has to cross, which in turn slows down the dynamics. We thus observe dramatic slowing down of the dynamics by tuning either of these parameters, in passive systems [136] and in ensembles of self-propelled particles [81, 82]. In the following we will borrow examples from systems where temperature is decreased at fixed density, and will extrapolate to the behaviour of system where density is increased at fixed temperature.

In order to characterise the typical time scale of the movement over a given distance $\lambda = 2\pi/k$, we first compute the self-intermediate scattering function [132]

$$F_s(k,t) = \frac{1}{N}\sum_{i=1}^{N} \langle \cos(\boldsymbol{k}\cdot\Delta\boldsymbol{r}_i(t))\rangle \,. \tag{2.40}$$

At small times, $|\Delta\boldsymbol{r}_i(t)| \ll \lambda$ and $F_s(k,t)$ is close to 1. At large times, if all the particles satisfy $|\Delta\boldsymbol{r}_i(t)| \gg \lambda$, then $F_s(k,t)$ is close to 0. We define the characteristic time $\tau_s(k)$ [137, 138] over which $F_s(k,t)$ relaxes from 1 to 0,

$$F_s(k,\tau_s(k)) = e^{-1}, \tag{2.41}$$

which indicates over which time scale the displacements of the particles relax above the length scale λ. By convention, we define the structural relaxation time scale [82]

$$\tau_\alpha = \tau_s(k^*) \tag{2.42}$$

which characterises the time scale over which the displacements of the scale of the interparticle distance $r_{\mathrm{nn}} = 2\pi/k^*$ (2.34) relaxes. In dense and disordered passive systems, movements over this length scale corresponds to cage escapes, which are the elementary structural relaxation events in the system [64]. We can also define the dynamical overlap

$$Q(t,a) = \frac{1}{N}\sum_{i=1}^{N} \langle \Theta(a - |\Delta\boldsymbol{r}_i(t)|)\rangle \tag{2.43}$$

where $\Theta(a - |\Delta\boldsymbol{r}_i(t)|)$ is 1 if and only if particle 1 moved less than a length scale a over time scale t and 0 otherwise. It is thus analogous to F_s in that it indicates over which time scale the displacements of relax above the length a [139, 140].

The two-step relaxation scenario picture by the MSD (Fig. 2.5(a)) is mirrored in the self-intermediate scattering function F_s (Ref. [79], Fig. 5(d), same system of athermal AOUPs as Ref. [81]). At high temperatures, displacement over the length scale of the interparticle distance happens on time scales comparable to the persistence time, *i.e.* right after the initial ballistic regime. At small temperatures, the self-intermediate scattering function crosses over to a regime of very slow decay after the initial ballistic regime. This is a consequence of particles remaining close to their initial position for an extended period of time [132]. Eventually particles are able to escape and the whole structure relaxes on the time scale τ_α large compared to the persistence time τ_p.

Disordered solids in two dimensions are subject to Mermin-Wagner fluctuations [141], which are long-wavelength density fluctuations. In large systems, these may affect measures based on the sole displacements of individual particles over the scale of the interparticle distance [139]. In order to recognise cage-escape events, it is thus necessary to consider displacements of the particles with respect to their cage, *i.e.* to their initially neighbouring particles. Given $\mathcal{N}_i(0)$ the ensemble of nearest neighbours of particle i at time $t = 0$ (*e.g.* determined via Voronoi tesselation, or particles within a given interaction radius at initial time), we define the

cage-relative displacement

$$\Delta^{\mathrm{CR}}\boldsymbol{r}_i(t) = \Delta\boldsymbol{r}_i(t) - \frac{1}{\#\mathcal{N}_i(0)} \sum_{j\in\mathcal{N}_i(0)} \Delta\boldsymbol{r}_j(t) \tag{2.44}$$

where $\#\mathcal{N}_i(0)$ is the number of elements in $\mathcal{N}_i(0)$. We can compute their variance (similarly to (2.36)), and the characteristic time scales of these displacements from the corresponding self-intermediate scattering function (similarly to (2.40)).

Another consequence of cage escapes is that particles change their local environment, with initially neighbouring particles leaving their neighbourhood. It is thus possible to characterise the time scale over which the structure relaxes by following the number of particles still close to their initial neighbours. We introduce the bond-breaking correlation function [142]

$$C_b(t) = \left\langle \frac{\sum_{i,j=1}^{N} \Theta(|\boldsymbol{r}_j(t) - \boldsymbol{r}_i(t)|/\sigma_{ij} - A_2)\,\Theta(A_1 - |\boldsymbol{r}_j(0) - \boldsymbol{r}_i(0)|/\sigma_{ij})}{\sum_{i,j=1}^{N} \Theta(A_1 - |\boldsymbol{r}_j(0) - \boldsymbol{r}_i(0)|/\sigma_{ij})} \right\rangle \tag{2.45}$$

which quantifies the percentage of pairs of particles i and j whose scaled distance $|\boldsymbol{r}_j - \boldsymbol{r}_i|/\sigma_{ij}$ is below A_1 (*bonded*) at $t = 0$ and above A_2 at t (*unbonded*). In order to avoid noise in the form of short-time oscillations, we use $A_2 > A_1$ [143].

2.3.2.2 Dynamical heterogeneity

Relaxation in dense and disordered systems is dynamically heterogeneous [54, 59, 144]. On time scales corresponding to the relaxation time scale τ_α, there is a clustering of particles with respect to their mobility: in some regions of the systems particles have moved large distances compared to the interparticle distance, while in other regions of the systems particles almost have not moved. Relaxation is heterogeneous in both time and space.

On the one-particle level, it can be uncovered via the distribution of displacements, or self part of the van Hove function [56, 144]

$$G_s(r,t) = \frac{1}{2N} \sum_{i=1}^{N} \langle \delta(r - \Delta r_{i,x}) + \delta(r - \Delta r_{i,y}) \rangle \,. \tag{2.46}$$

This function is the distribution of algebraic displacements along any direction (assuming isotropy) and not of their norms. At small times $t \to 0$, this distribution matches the distribution of the velocities (2.59). In passive (equilibrium) systems, the latter is the Maxwell-Boltzmann distribution, *i.e.* Gaussian. At large time $t \gg \tau_\alpha$, the distribution of the displacements is also Gaussian [144, 145]. On intermediate time scales, the distribution has a Gaussian central part with exponential tails, where movements inside the cage populate the central parts, and relaxation movements (cage escapes) populate the tails [146].

On the multi-particle level, dynamical heterogeneities can be uncovered with four-point correlation functions [54]. Given a dynamical observable $o_i(t)$, *i.e.* which characterises the mobility of particle i over time t, we define its four-point correlation function [140, 147]

$$G_4(\boldsymbol{r},t) = \frac{1}{N} \sum_{i,j=1}^{N} \left[\langle o_i(t) o_j(t) \delta(\boldsymbol{r} - (\boldsymbol{r}_j(0) - \boldsymbol{r}_i(0))) \rangle - \langle o_i(t)\delta(\boldsymbol{r}) \rangle \langle o_j(t)\delta(\boldsymbol{r}) \rangle \right] \tag{2.47}$$

which indicates the degree to which particles at an initial separation of $\boldsymbol{r}$ have correlated mobilities [54]. We introduce the spatial integral of this quantity, known as *dynamical susceptibility*

$$\chi_4(t) = \int \mathrm{d}^2\boldsymbol{r}\, G_4(r,t) = N \left[\left\langle \left| \frac{1}{N} \sum_{i=1}^{N} o_i(t) \right|^2 \right\rangle - \left\langle \frac{1}{N} \sum_{i=1}^{N} o_i(t) \right\rangle^2 \right] \tag{2.48}$$

which is related to the typical number of particles involved in correlated motion, or equivalently the size of correlated clusters [54].

Ref. [145] (Fig. 5(c)) illustrates, for passive particles, that for times small or large compared to the relaxation time scale τ_α the distribution of displacements is Gaussian. On time scales comparable to τ_α then this distribution shows the existence of two distinct sub-groups of particles, with the small-distance travelling particles being those which stayed within their cage (*immobile* particles), and the large-distance travelling particles being those which have relaxed relaxed their local structure by escaping their cage (*mobile* particles) [145]. This heterogeneity of the dynamics on time scales comparable to τ_α, with different populations of mobile and immobile particles, is also illustrated by the dynamical susceptibility χ_4 (Fig. 2.6, same system of athermal AOUPs as

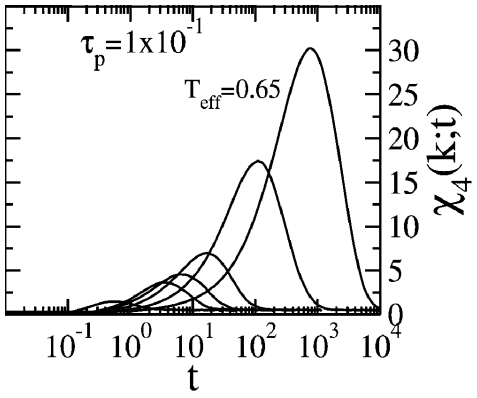

Figure 2.6: Dynamical susceptibility (2.48) computed from $o_i(t) = \cos(\boldsymbol{k}^* \cdot \Delta \boldsymbol{r}_i(t))$, *i.e* such that $F_s(k^*, t) = (1/N) \sum_{i=1}^{N} \langle o_i(t) \rangle$, as a function of time, at constant persistence time τ_p and packing fraction ϕ, and different packing fraction free-particle self-diffusion constant $D_0 = T_{\text{eff}}$. Taken from Ref. [79], Fig. 14(d). The system is athermal AOUPs interacting via a WCA potential.

Ref. [81]). At small (resp. large) times, the system is homogeneously composed of immobile (resp. mobile) particles, therefore the variance in (2.48) cancels. On time scales comparable to the relaxation time scale τ_α, the dynamics is maximally heterogeneous and χ_4 peaks [79]. As the dynamics slows down, *i.e.* as τ_α increases, then the height of the peak in χ_4 also increases. This indicates that the relaxation is spatially correlated over a length scale which increases as the dynamics slows down [54, 79].

2.4 Emergence of velocity correlations

At equilibrium, in virtue of the Maxwell-Boltzmann distribution, positions and velocities are independent, therefore it is impossible to observe velocity correlations in space. Out of equilibrium, this does not have to hold, and there have indeed been several reports of extended velocity correlations in dense systems of self-propelled particles [82, 113, 124]. More recently, several analytical derivations were brought forward to explain the emergence of these correlations, in active crystals [88], glasses [35], and liquids [103].

In this Section, we will follow the reasoning of Ref. [35] to show how the competition between persistent forcing and particles' crowding leads to velocity correlations, and then explore some properties of these correlations.

2.4.1 Harmonic description of the dynamics

In order to understand the emergence of velocity correlations in dense systems of self-propelled particles, it is useful to first consider the case of a single AOUP in a 1D harmonic potential

$$\dot{r} = -\tau_0^{-1} r + p, \tag{2.49a}$$

$$\tau_p \dot{p} = -p + \sqrt{2D_0}\eta, \tag{2.49b}$$

where η is a unit-variance zero-mean Gaussian white noise. Following Ref. [148], we write the Fokker-Planck equation [106] from (2.49)

$$\frac{\partial}{\partial t}\text{Prob}(r,p,t) = -\frac{\partial}{\partial r}\left[(-\tau_0^{-1} r + p)\text{Prob}(r,p,t)\right] - \frac{\partial}{\partial p}\left[-\tau_p^{-1}\text{Prob}(r,p,t)\right] + \frac{\partial^2}{\partial p^2}\left[D_0/\tau_p^2 \text{Prob}(r,p,t)\right] \tag{2.50}$$

which we solve in the stationary case $\partial_t \text{Prob}(r,p) = 0$ with the hypothesis

$$\text{Prob}(r,p) \propto \exp(-ar^2 - bp^2 - cxp) \tag{2.51}$$

and find

$$a = \frac{(\tau_0 + \tau_p)^2}{2D_0\tau_0^3},\ b = \frac{\tau_p(\tau_0 + \tau_p)}{2D_0\tau_0},\ c = -\frac{\tau_p(\tau_0 + \tau_p)}{D_0\tau_0^2}. \tag{2.52}$$

This stationary distribution of the position and propulsion enables us to compute the mean elastic energy in this harmonic mode

$$\left\langle \frac{1}{2}\tau_0^{-1} r^2 \right\rangle = \frac{D_0}{2}\frac{1}{1+\tau_p/\tau_0}. \tag{2.53}$$

We recover the equipartition of elastic modes in the limit $\tau_p \ll \tau_0$, *i.e.* the equilibrium limit. On the opposite limit $\tau_p \gg \tau_0$

$$\left\langle \frac{1}{2}\tau_0^{-1} r^2 \right\rangle \underset{\tau_p \gg \tau_0}{=} \frac{D_0}{2}\frac{1}{\tau_0^{-1}\tau_p} \tag{2.54}$$

we have a violation of the equipartition theorem. Moreover (2.54) indicates first that the softer the mode (*i.e.* the smaller τ_0^{-1}) the larger its elastic energy, and second that this favouring of softer modes increases with increasing persistence time τ_p.

We can use this result with an ensemble of AOUP by making a linear expansion of (2.15) around a local minimum of U

$$\begin{pmatrix} \dot{\boldsymbol{r}}_1 \\ \vdots \\ \dot{\boldsymbol{r}}_N \end{pmatrix} = -\mathbb{H} \begin{pmatrix} \boldsymbol{r}_1 \\ \vdots \\ \boldsymbol{r}_N \end{pmatrix} + \begin{pmatrix} \boldsymbol{p}_1 \\ \vdots \\ \boldsymbol{p}_N \end{pmatrix} \tag{2.55}$$

where we introduce the Hessian matrix

$$\mathbb{H}_{ij} = \partial_{\boldsymbol{r}_i}\partial_{\boldsymbol{r}_j} U. \tag{2.56}$$

Eq. (2.55) is a set of N equations in the form of (2.49) when projected onto the eigenmodes of $\mathbb{H}$. We will denote its eigenvalues $\tau_{0,k}^{-1}$. An important observation is that the lower $\tau_{0,k}^{-1}$ the more spatially extended the corresponding eigenmode [58, 149–151], therefore the *most extended* modes which are the *softest* modes are the *most favoured* by the persistent dynamics. It is this mechanism, in which a persistent active force is applied to an elastic sheet formed by the packing of particles, which is at the origin of velocity correlations.

There are other ways of linearising the dynamics. Ref. [35] suggests to rewrite (2.15) for a dense packing packing of polydisperse ABPs in a continuum elastic formulation, which in Fourier space involves the dynamical matrix whose eigenvalues depend on the elastic moduli of the system. Ref. [88] proposes to take the Fourier transform of (2.15) using the crystalline symmetry of their dense monodisperse system and doing a harmonic approximation of the interaction potential U. Ref. [103] proceeds similarly as Ref. [35] for dense ABPs but uses the Fourier transform of the virial part of the pressure tensor which is linearised around the average density. We also point out the existence of Ref. [104] which develops an involved hydrodynamic theory, and whose results are qualitatively consistent with Refs. [35, 103].

We classify these proofs in two categories. First the proofs which share the similarity that the dynamics is considered as a (persistent) perturbation of a local quadratic minimum of the interaction potential U [35, 88], such that *e.g.* the eigenmodes and eigenvalues of $\mathbb{H}$ do not change with time and thus we can take the average in (2.53). This assumption should hold under two conditions. First, the displacements must be small. This implies that the self-propulsion force ξv_0 itself is small. Second, the time spent inside a minimum should be much larger than the time to decorrelate the propulsions. This should be satisfied if the relaxation time (2.42) $\tau_\alpha \gg \tau_p$ [35]. Then there are hydrodynamic theories [103, 104] which partly rely on uncontrolled hypotheses, it is thus not possible for the moment to exactly identify their framework of applicability. We note however that part of their results are consistent with the former class of theories, which highlights the universality of these findings.

2.4.2 Emerging scales of velocity correlations

In this Section, we will review the literature around the properties of the velocity field in dense systems of self-propelled particles. We will first describe its correlations in space (two-particle quantity) and in time (single-particle), and then the one-particle velocity distribution.

There are two kinds of correlations which we aim to characterise: correlations in space which are quantified by correlation functions of the form of

$$C_{\boldsymbol{vv}}(r) = \frac{1}{(1/N)\sum_{i=1}^N \langle |\boldsymbol{v}_i(0)|^2 \rangle} \left\langle \frac{\sum_{i,j=1;i\neq j}^N \boldsymbol{v}_i(0)\cdot\boldsymbol{v}_j(0)\,\delta(r-|\boldsymbol{r}_j(0)-\boldsymbol{r}_i(0)|)}{\sum_{i,j=1;i\neq j}^N \delta(r-|\boldsymbol{r}_j(0)-\boldsymbol{r}_i(0)|)} \right\rangle \tag{2.57}$$

which is 1 at $r = 0$ by definition and decays over a characteristic finite length scale $\xi_{\boldsymbol{v}}$ known as the velocity correlation length, and correlations in time which are quantified by autocorrelation functions of the form of

$$C_{\boldsymbol{v}}(t) = \left\langle \frac{\sum_{i=1}^N \boldsymbol{v}_i(0)\cdot\boldsymbol{v}_i(t)}{\sum_{i=1}^N |\boldsymbol{v}_i(0)|^2} \right\rangle \tag{2.58}$$

which is 1 at $t = 0$ by definition and may decay on several different time scales. We expect these correlation functions to be strictly decreasing functions of distance and time respectively. Velocity correlation lengths $\xi_{\boldsymbol{v}}$

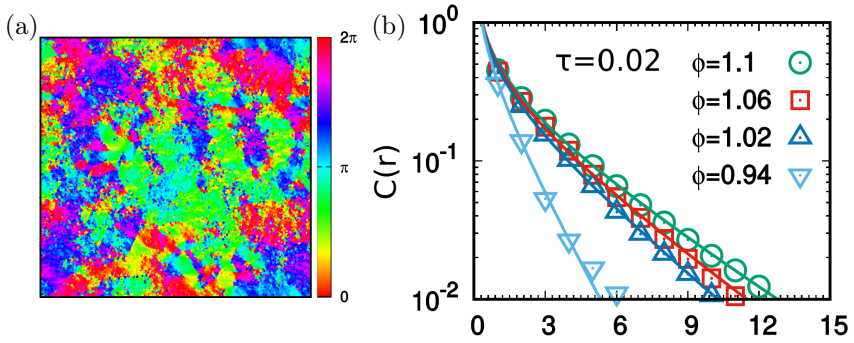

Figure 2.7: (a) Snapshot of the system where each disk represents a particle, with the colour corresponding to the orientation of its velocity $\arg(\boldsymbol{v}_i)$. Taken from Ref. [88], Fig. 3(d). (b) Velocity correlation function as a function of r, of the form of (2.57), for different packing fractions ϕ, at fixed persistence time $\tau_p = \tau$ and free-particle self-diffusion constant D_0. Taken from Ref. [88], Fig. 5(d). The system is athermal ABPs interacting via a WCA potential.

can be computed either by thresholding the correlation function [152], *i.e.* determining the distance above which the correlation function is below a given threshold, or fitting the correlation length to some expected functional form in real space [35] or Fourier space [103].

We follow Ref. [88] which studies the emergence of velocity correlations in dense and persistent systems of ABPs. We show an example for the velocity field in Fig. 2.7(a). The velocity correlation length $\xi_{\boldsymbol{v}}$ characterises the size of the patches of aligned velocities, *i.e.* single-colour patches. We showed in the previous Section that the velocity correlations emerge from the persistent forcing (on a time scale τ_p) of the elastic medium formed by the dense packing of particles. In a continuum elastic description [35, 153], the properties of this elastic medium is described by elastic moduli (longitudinal and transversal). Thus, the correlation length is expected to increase with increasing elastic moduli of the system [35, 103] (or increasing curvature of the potential [88]), and increasing persistence time τ_p [35, 81, 82, 88, 103]. This is confirmed by Fig. 2.7(b) where the correlation length increases with increasing packing fraction ϕ [88].

Ref. [35] indicates that there are two different kinds of time scales over which the velocity correlations in time (2.58) decays. First there are the harmonic time scales associated with the relaxation in the quadratic expansion around the potential energy minimum. Then there is the persistence time τ_p which is the time scale over which the propulsion forces evolve. It is noteworthy that in Ref. [35], the expression for the velocity autocorrelation function (2.58) (Eq. 57 in Supplementary Material) converges if and only if the persistence time is smaller than the harmonic time scales. This is consistent with the assumption in Sec. 2.4.1 that propulsion forces should change on time scales which are smaller (*i.e.* faster) than the time scale on which configurations change. Finally, we highlight that Ref. [154] provides an other connection between the propulsion dynamics and the elastic properties of the system, showing that the fluidisation of an active glass happens when the persistence time τ_p coincides with the characteristic time scale of the most unstable direction in the energy potential landscape.

Non-equilibrium properties may also appear in the distribution of algebraic velocities along any direction (assuming isotropy)

$$\mathrm{Prob}(\mathrm{v}) = \frac{1}{2N}\sum_{i=1}^{N}\left\langle \delta(\mathrm{v} - v_{i,x}(0)) + \delta(\mathrm{v} - v_{i,y}(0))\right\rangle . \tag{2.59}$$

This distribution is characterised by its variance $v^2 = \left\langle |\boldsymbol{v}_i|^2 \right\rangle /2$ (2.38), which sets the typical value of the velocity. In a free system, where the velocity equals the self-propulsion force (2.2), this variance is half the variance of the self-propulsion force, *i.e.* v_0^2. At equilibrium, in virtue of the Maxwell-Boltzmann distribution, velocities should be normally distributed. This does not have to hold out of equilibrium ($\tau_p > 0$). Deviations from the Gaussian behaviour can be quantified via different non-Gaussian parameters [144, 145, 155]. These parameters appear as ratios of fourth-order and second-order moments, which are trivial for Gaussian distributions. The larger these parameters are the more important large values of the velocities are compared to their normal distribution.

At large persistence time τ_p, the speed of particles becomes negligible compared to the self-propulsion velocity [35, 156]. This indicates that, at large persistence, the interaction forces counter-balance the self-propulsion forces, hence a decrease of the velocity variance. This is supported by Fig. 2.8 (same model of athermal ABPs as Ref. [88]), which shows that, as the typical velocity of the particles plummets, the typical interaction force soars up to the value of the self-propulsion velocity. Moreover, at large persistence, the distribution of velocities

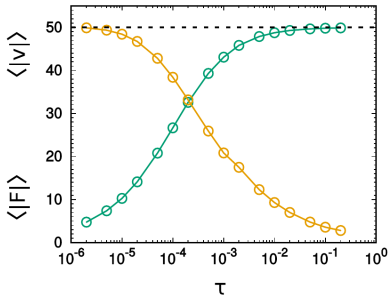

Figure 2.8: Typical velocity amplitude $\langle|\boldsymbol{v}_i(0)|\rangle$ and typical force amplitude $\langle|\boldsymbol{F}_i(0)|\rangle = \langle|\nabla_i U(0)|\rangle$ as functions of τ_p, for fixed v_0 and ϕ. Taken from Ref. [156], Fig. 2. The system is athermal ABPs interacting via a WCA potential.

departs from a Gaussian behaviour and develops fat tails, indicative of the non-trivial influence of many-body interactions in persistent liquids [156, 157].

2.5 Scales and emerging behaviour

We have introduced a model of overdamped particles (2.15). On each of these particles acts an independent self-propulsion force $\boldsymbol{p}_i$ (2.16) with a characteristic time scale of evolution τ_p (2.7), and a characteristic amplitude which in turn leads to a free-particle self-propulsion velocity v_0 (2.10). These scales define a length scale $\ell_p = v_0\tau_p$ (2.12) which corresponds, for a free particle, to the distance travelled before losing memory of its initial velocity. These scales have to be compared with other characteristic scales of the model (2.14): the interaction time scale τ_0 (1 in our units) which sets the time to relax two-particles interactions, and the typical length between two particles which we expect to be of the same order of the average diameter of a particle σ (1 in our units) in a dense system.

At small persistence $\tau_p \ll \tau_0$, the time over which an individual propulsion changes is smaller than the time over which the interaction between two particles changes. Therefore, on the time scale τ_0, the self-propulsion force acts as an effective zero-correlation white noise. This corresponds to the Brownian limit, and the system acquires equilibrium properties such as the Maxwell-Boltzmann distribution, or the equipartition of elastic modes. On the contrary, at large persistence $\tau_p \gtrsim \tau_0$, on the time scale over which the interaction between two particles changes the individual particles keep a memory of their previous propulsion force. This leads to non-trivial behaviour such as the emergence of velocity correlations in space and time, non-Gaussian velocity distributions, and plummeting velocity variance. Moreover, in the case where $\ell_p \gg \sigma$, *i.e.* when particles move ballistically between collisions, they are able to accumulate, leading to a non-equilibrium transition to a phase-separated state known as MIPS, despite the absence of explicit aligning interactions.

On top of these two fundamental time scales (the persistence time τ_p and the interaction time τ_0), the dynamics of dense systems is also characterised by a third, emerging time scale, the relaxation time τ_α (2.42). This is the time scale on which the structure of the system relaxes, *i.e.* on which particles lose memory of their initial neighbours. In equilibrium and small-persistence systems, dynamics over this time scale is maximally heterogeneous, with a clustering of particles with respect to their mobility: mobile regions where particles have moved large distances compared to their own diameters, and immobile regions where particles have kept their initial neighbours.

We will explore during the remainder of this Thesis which collective motions emerge from the competition between these time scales (τ_p, τ_0, and τ_α), and the associated underlying mechanisms.

3 | Phase diagram of polydisperse AOUPs

In this Chapter, we will build the phase diagram of polydisperse AOUPs interacting via a WCA potential. We recall that there are, in the thermodynamic limit $N \to \infty$, three control parameters in our model. In order to present only a two-dimensional phase diagram, we have to decide a cut through parameter space. We decide to build the phase diagram at constant free-particle self-diffusion constant $D_0 = 1$, and thus draw the diagram in the space spanned by the packing fraction ϕ and the persistence time τ_p. We will discuss this choice in Sec. 3.3.

We will first delineate the region where the system is homogeneous. We will then delimit the domain where the system is dynamically arrested, and characterise the orientational and translational order in this phase. We will finally present the phase diagram in the space of constant D_0, and discuss this choice of a cut through phase space. This program parallels the one already undertaken for monodisperse particles [46, 49, 88]. It is noteworthy that our model model includes an interaction potential which, in contrast to polydisperse harmonic potentials [76], diverges at the origin. This enables us to study crowded systems of self-propelled particles at large persistence where interaction forces are able to be of the same order of propulsion forces.

Some of the results of this Chapter were published in Ref. [158].

Contents

3.1 Motility-induced phase separation

We expect the system to spontaneously phase separate when the persistence length $\ell_p = \sqrt{D_0 \tau_p}$ is large compared to the typical distance between particles (of order 1) [1, 129] (see Sec. 2.3.1.1).

In order to determine if the system is homogeneous or phase-separated, we measure the distribution of the local packing fraction ϕ_{loc} (2.26) [49, 109, 113]. In practice, we exploit the fact that the positions of the local maxima of the ϕ_{loc}-distribution do not depend on the global packing fraction ϕ [49, 109]. We thus generate steady-state configurations for different persistence times τ_p at constant $\phi = 0.50$ in which we measure histograms. From these histograms, we extract the positions of the local maxima when the distribution is bimodal as functions of the persistence time $(\phi_{\text{loc}}^{\min}(\tau_p), \phi_{\text{loc}}^{\max}(\tau_p))$. At a given τ_p for which these local maxima exist, the system will thus be phase-separated if the global packing fraction satisfies $\phi_{\text{loc}}^{\min}(\tau_p) < \phi < \phi_{\text{loc}}^{\max}(\tau_p)$. We observe that the distribution $\text{Prob}(\phi_{\text{loc}})$ is bimodal only if $\tau_p > 10^2$, *i.e.* $\ell_p > 10$, which is consistent with the condition of a large persistence length compared to the typical interparticle distance in order to observe MIPS [1, 129].

It is expected that the MIPS existence region ends in a critical point at low τ_p [159]. The precise characterisation of this critical point necessitates a finite-size scaling analysis. Since our interest is in the homogeneous dense phase and not the phase-separated state, this precise characterisation is outside of the scope of our study. A consequence of the existence of this critical point is that fluctuations of the local packing fraction are large close to it. For a given number of particles N, we may thus only see a broad distribution of local packing fractions ϕ_{loc} and not a clear bimodal distribution. This thus limits our ability to circumscribe the phase-separated region at small τ_p. Away from the critical point, and if the system is large enough, we expect that the properties of the bulk dense cluster to be representative of the dense homogeneous system at $\phi = \phi_{\text{loc}}^{\max}(\tau_p)$ [160, 161].

3.2 Dynamical arrest

We expect at large packing fraction ϕ that the dynamics of the system is unable to relax its structure, and the system thus goes from a liquid to an arrested glass (see Sec. 2.3.2). To confirm this scenario, we follow the dynamics of the system with the MSD (2.36), see Fig. 3.1(a, b). At small persistence time ($\tau_p = 10^{-2}$), the

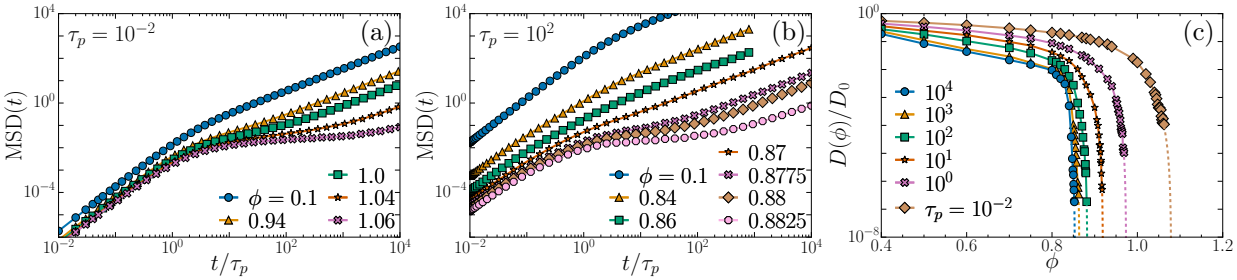

Figure 3.1: (a, b) Mean squared displacement (2.36) at fixed persistence time τ_p for different packing fractions ϕ. (c) Effective diffusion constant D (2.39) rescaled by the free-particle self-diffusion constant D_0 as a function of packing fraction ϕ for different persistence times τ_p. Dashed lines correspond to fits to (3.1). These were obtained at fixed $\gamma = 3$. Parameter values: $N = 1024$, $D_0 = 1$, (a) $\tau_p = 10^{-2}$, (b) $\tau_p = 10^2$..

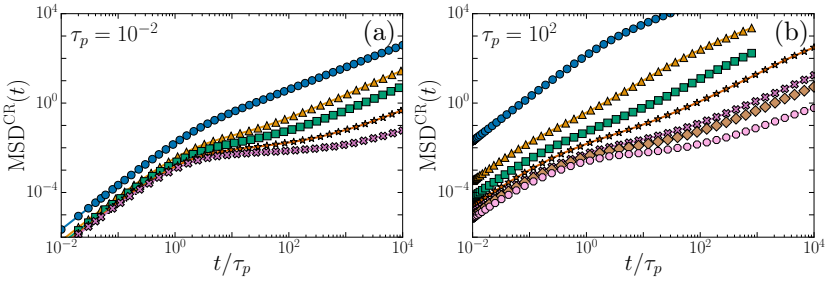

Figure 3.2: Cage-relative mean squared displacement $\mathrm{MSD}^{\mathrm{CR}}(t) = \left\langle |\Delta^{\mathrm{CR}}\boldsymbol{r}_i(t)|^2 \right\rangle$ (2.44). Parameter values: $N = 1024$, $D_0 = 1$, (a) $\tau_p = 10^{-2}$, (b) $\tau_p = 10^2$. Packing fractions are identical to Fig. 3.1.

dynamics slows down as ϕ is increased. This can be seen through the emergence of an intermediate subdiffusive regime (also referred to as *plateau* [144]), in between the initial ballistic regime and eventual diffusive regime, which extends further as ϕ is increased. This regime corresponds to caging [79, 82] and as a consequence the effective self-diffusion constant $D(\phi)$ drops significantly with respect to its $\phi \to 0$ limit D_0. At large persistence time ($\tau_p = 10^2$), we recover a similar scenario, with the emergence and extension of an intermediate subdiffusive regime, and the associated drop in $D(\phi)$. A major difference however resides in the fact the velocity variance v^2 (2.38) also drops significantly. This has major consequences for the relaxation dynamics which we will explore in Chap. 4.

As in equilibrium systems, the determination of a critical packing fraction for dynamic arrest is ambiguous [162]. We will give an estimation of this liquid-glass boundary $\phi_c(\tau_p)$ by fitting the effective diffusion constant $D(\phi)$ to an algebraic form inspired by mode-coupling theory,

$$D(\phi) \sim (\phi_c(\tau_p) - \phi)^\gamma, \tag{3.1}$$

at large ϕ. We stress that this boundary represents a lower bound for the real critical packing fraction [162]. Indeed, if we had the computational ability and/or time to simulate the steady state of denser liquids then this limit would shift to larger packing fractions. We plot in Fig. 3.1(c) the diffusion constant as a function of the packing fraction $D(\phi)$ for different persistence times τ_p alongside with the fit to (3.1). All the systems have the same free-particle self-diffusion constant D_0, therefore their rescaled diffusion constant $D(\phi)/D_0$ have to go to 1 as $\phi \to 0$. We observe, in the range of persistence times explored here, that the critical packing fraction ϕ_c decreases with increasing τ_p. However, this may not always be the case, depending on the specific value of D_0 [81].

Not all glasses vitrify in the same way, and this is qualitatively evaluated by their fragility [67, 122, 163]. Strong glasses solidify gradually, and their relaxation time τ_α follows an Arrhenius law $\log \tau_\alpha \sim 1/T$ (where T is the temperature). Fragile glasses solidify more abruptly, in a super-Arrhenius fashion. A study on athermal AOUPs found that fragility would increase with increased persistence time τ_p [79]. It would be possible to study fragility in our system, not as a function of temperature but as a function of packing fraction ϕ. Fig. 3.1(c) seems to indicate that the decrease in effective diffusion constant is faster (and thus systems are more fragile) as the persistence time is increased, possibly because both the intermediate-time localisation and the drop in the velocity variance decrease the diffusion constant. This behaviour should be mirrored by the relaxation time τ_α even though we should expect deviation from the Stokes-Einstein law and thus that D and τ_α are not exactly inversely proportional [67, 79]. Because of the lack of data, especially at very high relaxation time τ_α, we were not able to quantitatively characterise the fragility of our system with varying persistence time τ_p.

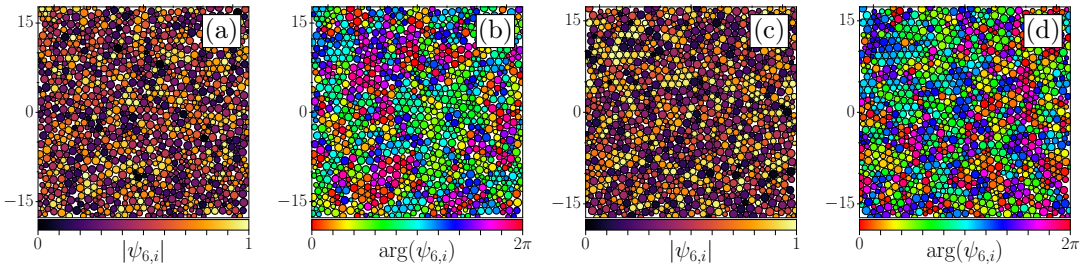

Figure 3.3: Snapshots of the hexatic order parameter $\psi_{6,i}$ (2.28). (a, c) Modulus of hexatic order parameter $|\psi_{6,i}|$. (b, d) Argument of the hexatic order parameter $\arg(\psi_{6,i})$. Parameter values: $N = 1024$, $D_0 = 1$, $\tau_p = 10^2$, (a, b) $\phi = 0.84$, (c, d) $\phi = 0.8825$.

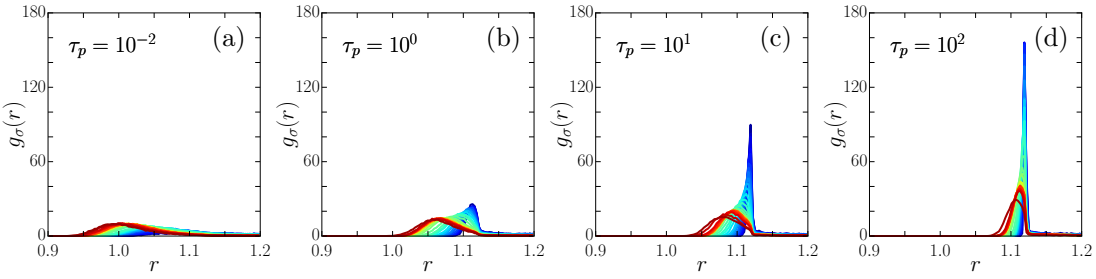

Figure 3.4: Rescaled pair distribution function $g_\sigma(r)$ (3.2) at fixed persistence time. In each plot, packing fraction increases from the rightmost curve (blue) to the leftmost curve (red). Parameter values: $N = 1024$, $D_0 = 1$, (a) $\tau_p = 10^{-2}$: $\phi = 0.1$ to 1.1, (b) $\tau_p = 10^{0}$: $\phi = 0.1$ to 0.98, (c) $\tau_p = 10^{1}$: $\phi = 0.1$ to 0.94, (d) $\tau_p = 10^{2}$: $\phi = 0.1$ to 0.89.

As in equilibrium, this transition from a liquid of polydisperse particles to an arrested solid is not accompanied by the emergence of hexatic or translational order [52, 132]. In order to (qualitatively) compare the evolution of structural order and dynamics, we plot in Fig. 3.3 the hexatic order parameter $\psi_{6,i}$ (2.28) for two large-persistence systems ($D_0 = 1$, $\tau_p = 10^2$) at two different densities: $\phi = 0.84$ ($D = 6 \times 10^{-3}$) and $\phi = 0.8825$ ($D = 6 \times 10^{-8}$). Here, a decrease of 5 orders of magnitude of the diffusion constant $D(\phi)$ is not accompanied by a significant change in the correlations of the hexatic order parameter, and thus the system remains isotropic. We quantitatively probe the structure of the disordered liquid with the pair correlation function $g(r)$ (2.32). The position of the first peak of $g(r)$ is associated to the distance of the first shell of close neighbours while its width informs us about the inherent disorder in the system [132]. It is common practice for binary systems (*i.e.* polydisperse systems with two different diameters) to decompose $g(r)$ into different correlations between pairs of particles with constrained diameters [79, 144]. Our own system is continuously polydisperse therefore such an analysis in not possible. We therefore consider a rescaled pair distribution function based on the interaction range

$$g_\sigma(r) = \frac{1}{2\pi r}\frac{L^2}{N^2}\sum_{i=1}^{N}\sum_{j\neq i}\langle\delta(r - |\boldsymbol{r}_j - \boldsymbol{r}_i|/\sigma_{ij})\rangle\,, \tag{3.2}$$

such that the position of the first peak informs us about how deep neighbouring particles are into their interaction potential.

We plot in Fig. 3.4 the rescaled pair distribution function $g_\sigma(r)$ (3.2) for increasing packing fraction ϕ from right to left, and increasing persistence time τ_p from left to right. As τ_p is increased, the first peak of $g_\sigma(r)$ both shifts to larger distances and becomes narrower. This is already explained by the fact that as τ_p increases at fixed D_0, the self-propulsion force ξv_0 becomes smaller and thus particles appear stiffer and penetrate less each others and the peak shifts to larger distances [81]. Moreover, there is an increased adhesion as particles become more persistent, resulting in an enhanced peak [81]. More surprisingly, we observe that at large persistence time, the height of the peak strongly decreases with increasing packing fraction ϕ. We observe a weak increase of the height of the peak at small persistence time. This rules out the development of translational order with increasing ϕ, as the latter would on the contrary enhance the peaks of the pair distribution [51].

For the persistence times we have considered, we always measured $\phi_c(\tau_p) > \phi_{\rm loc}^{\rm max}(\tau_p)$, which implies that the dense cluster of MIPS, even at high persistence time, is not a solid as observed for monodisperse systems [46, 49]. We bring further evidence of this by characterising the dynamics of the dense cluster of MIPS, via the self-intermediate scattering function F_s (2.40), as a function of the persistence time τ_p. In order to consider only

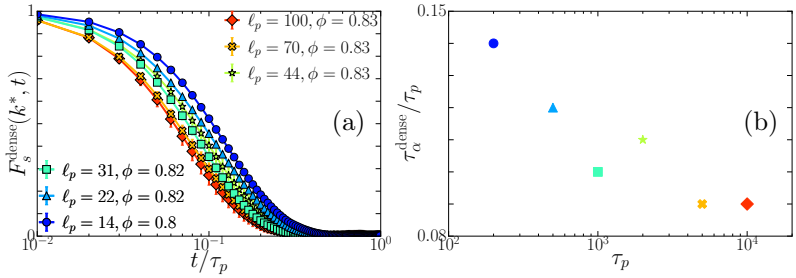

Figure 3.5: (a) Self-intermediate scattering function $F_s^{\rm dense}$ (2.40) in the bulk dense phase of phase-separated systems. (b) Relaxation time $\tau_\alpha^{\rm dense}$ (2.42) in the bulk dense phase of phase-separated systems, rescaled by the persistence time τ_p as a function of the persistence time τ_p. Parameter values: $N = 16384$, $D_0 = 1$. Markers and colours correspond to the systems in both panels.

particles belonging to the bulk of the dense phase, we simulate systems at packing fractions $\phi \lesssim \phi_{\rm loc}^{\rm max}(\tau_p)$ and compute for the ensemble of particles i the local packing fraction $\phi_{\rm loc}(\boldsymbol{r}_i(t), a = 5)$ at time t. We identify all particles which, at some time t, have a local packing fraction $\phi_{\rm loc} < 0.30$, and particles which are at a distance smaller than $d = 20$ of the former at time t. The resulting set of particles is subtracted from the ensemble of particles and we compute the self-intermediate scattering function $F_s^{\rm dense}$ (2.40) only considering the remaining particles. We checked qualitatively on simulation snapshots that the remaining ensemble of particles does not contain gas bubbles. We plot in Fig. 3.5(a) these scattering functions. We observe in the bulk region of the dense cluster of MIPS that movement on the scale of the interparticle distance happens on time scales which are smaller than the persistence time, *i.e.* $\tau_\alpha \lesssim \tau_p$. Moreover, the ratio τ_α/τ_p decreases with increasing persistence time (see Fig. 3.5(b)), indicating that the dynamics in the dense cluster of MIPS becomes faster *on the scale of* τ_p as the latter increases.

3.3 Conclusion: phase diagram

We use the packing fraction boundaries of the MIPS region, and the critical packing fraction for the non-equilibrium glass transition (see Fig. 3.1(c)), to plot the phase diagram of our system in Fig. 3.6.

The most exciting feature in this phase diagram is that, because regions of phase-separated systems and arrested systems do not overlap, it is possible to observe a disordered flowing liquid at large persistence time $\tau_p \gg \tau_0$ and moderate packing fraction $\phi_{\rm loc}^{\rm max} < \phi < \phi_c$.

We expect the specific value of D_0 to change the shape of the non-equilibrium glass transition line [81, 82] and also the shape of the MIPS boundary [76]. However, the separation of the MIPS and glass regions should hold. This conclusion comes from the fact that the dynamics in the MIPS dense cluster on the one hand (which we consider to be representative of the dynamics of the bulk system with the same packing fraction $\phi_{\rm loc}^{\rm max}$), and the dynamics close to dynamical arrest on the other hand, correspond to two different limits. Fig. 3.5 shows that, for the former, movements over the scale of the interparticle distance $r_{\rm nn} \sim 1$ happens on time scales $\tau_\alpha \lesssim \tau_p$. Fig. 3.1(a, b) shows that on the contrary, close to dynamical arrest, movement over the scale of $r_{\rm nn}$ happens on time scales at which the initial propulsions have decorrelated, thus $\tau_\alpha \gg \tau_p$. Therefore, MIPS and the arrested glass regions should remain distinct irrespectively of our free-particle self-diffusion constant D_0,

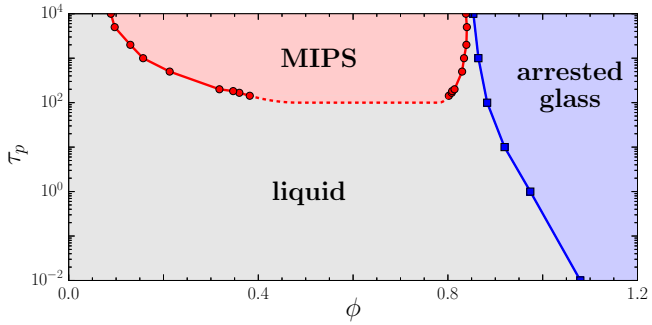

Figure 3.6: Phase diagram at $D_0 = 1$. We only sketch the critical point of MIPS, its precise characterisation requiring a more detailed analysis [159].

and the features of our phase diagram thus do not depend on D_0.

We now seek to explore the behaviour and properties of the dense and persistent active liquid. We will review in Chaps. 4, 5 the limit $\tau_\alpha \gg \tau_p$ on the path to dynamical arrest, and is Chap. 6 the limit $\tau_\alpha \lesssim \tau_p$.

4 | Structural relaxation in dense and persistent liquids

Activity is at the origin of non-equilibrium behaviours such as macroscopic phase separation in the absence of attractive potential (MIPS) [1, 46, 109, 125, 127] and mesoscopic velocity correlations [35, 88, 103, 156]. These phenomena have non-trivial influence on the dynamics of dense systems of self-propelled particles. Persistent forces propel particles against each other resulting in more localised neighbourhoods of particles [81]. In monodisperse systems this leads to the formation of ordered solids [46, 49, 51]. In passive polydisperse systems, enhancement of the structure is generally associated with slower dynamics, predicted for example by theories such as the mode-coupling theory (MCT) [64]. In active polydisperse systems, this enhancement of the structure is accompanied by the emergence of velocity correlation which, on the contrary, fluidifies the system [78, 81, 164]. Other theories such as an active version of random first-order transition (RFOT) theory [83, 87] have sought to capture the influence of activity on the non-equilibrium glass transition. The major issue in these theories is that, at large persistence, it is difficult to disentangle (non-linear) crowding effects at the origin of the slowing down and the propulsion-induced collective motion of particles [83].

We propose a microscopic study of the slow structural relaxation of dense systems of persistent self-propelled particles to tackle the question: how do non-equilibrium velocity correlations influence the slow dynamical relaxation close to the glass transition? We will first explore the properties of the emerging velocity correlations in the large-persistence limit. We will then discuss the mechanisms of relaxation available to dense systems of self-propelled particles in this limit.

Some of the results of this Chapter were published in Ref. [158].

Contents

4.1 Emerging velocity correlations

We have identified the existence of a dense liquid at large persistence $\tau_p \gg \tau_0$ (see Sec. 3.3). In this Section, we discuss several of its non-equilibrium properties.

We plot in Fig. 4.1(a) the scaled velocity variance $v^2/2v_0^2$ (2.38, 2.10) as a function of the persistence time τ_p and the packing fraction ϕ. In Fig. 4.1(b), we compare the distributions of velocities Prob(v) (2.59) for different ϕ at large persistence ($D_0 = 1$, $\tau_p = 10^3$). In equilibrium systems, velocities are spatially uncorrelated and

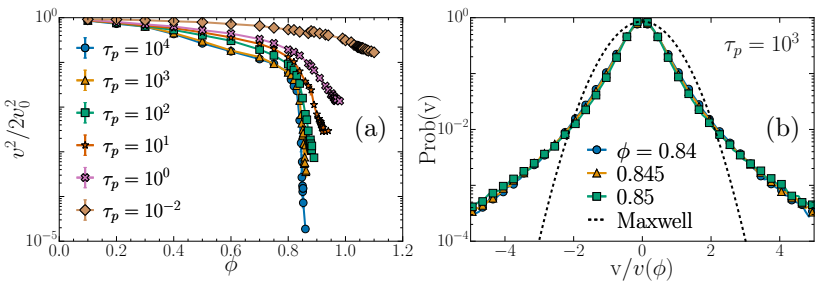

Figure 4.1: (a) Scaled velocity variance $v^2/2v_0^2$ (2.38, 2.10) as a function of the persistence time τ_p and the packing fraction ϕ. (b) Distributions of velocities Prob(v) (2.59) for different ϕ at large persistence. Parameter values: $D_0 = 1$, (a) $N = 1024$, (b) $N = 4096$, $\tau_p = 10^3$.

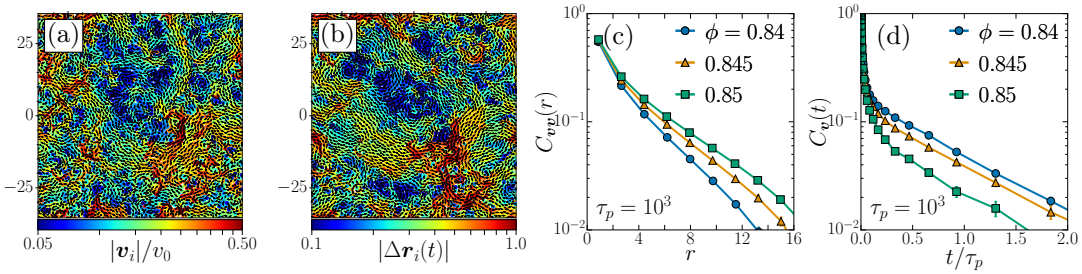

Figure 4.2: (a) Snapshot of the velocity field at time $t = 0$. Colours indicate the norm and arrows their direction. (b) Snapshot of the displacement field at time $t/\tau_p = 0.11$ (MSD$(t) = 0.16$). Colours indicate the norm and arrows their direction. (c) Velocity correlations in space $C_{\boldsymbol{vv}}(r)$ (2.57). (d) Velocity correlations in time $C_{\boldsymbol{v}}(t)$ (2.58). Parameter values: $N = 4096$, $D_0 = 1$, $\tau_p = 10^3$, (a, b) $\phi = 0.84$.

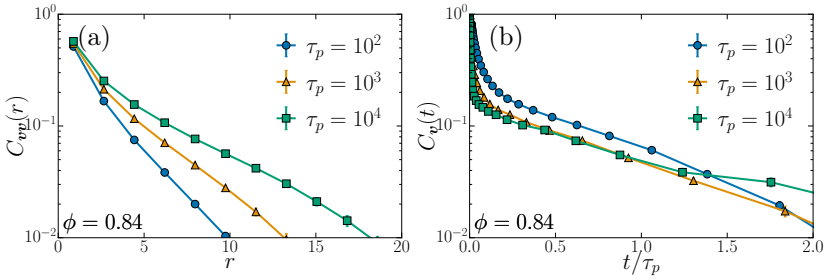

Figure 4.3: (a) Velocity correlations in space $C_{\boldsymbol{vv}}(r)$ (2.57). (b) Velocity correlations in time $C_{\boldsymbol{v}}(t)$ (2.58). Parameter values: $N = 4096$, $D_0 = 1$, $\phi = 0.84$.

obey the Maxwell distribution with a variance v^2 (2.38) independent of the packing fraction ϕ. The situation is very different in persistent systems, where both the variance and the shape of the distribution are modified. First, the variance $v^2(\phi)$ decreases sharply with ϕ (see Fig. 4.1(a)). We have previously shown that persistent particles stick to each other, which causes an enhancement of the structure (see Sec. 3.2). Another consequence of this sticking is that particles are able to arrest each other and thus the variance of the velocity decreases. At large ϕ and τ_p, we thus observe that $v^2 \ll 2v_0^2 = \langle |\boldsymbol{p}_i|^2 \rangle$, hence the velocity term is negligible in (2.15). Second, the velocity distributions are strongly non-Maxwellian with much broader tails (see Fig. 4.1(b)), even though a normal distribution is expected both for interacting equilibrium particles and for non-interacting Ornstein-Uhlenbeck particles. Our observation of these fat-tailed distribution with reduced variance is consistent with the expectation that v^2 is coupled to the local curvature of the interaction potential [156, 157]. Hence the measured distributions reveal the non-trivial influence of many-body interactions in persistent liquids.

As predicted in the literature [35, 36, 78, 79, 88, 103], persistent propulsions in the homogeneous liquid produce spatial velocity correlations, which we quantify in Fig. 4.2(c) via the velocity correlation in space (2.57). The data clearly reveal the existence of correlations extending over a length scale $\xi_{\boldsymbol{v}}$ which grows with ϕ and τ_p (see Fig. 4.3(a)). The corresponding real-space correlations extend over several particle diameters, as illustrated in Fig. 4.2(a). We use the velocity autocorrelation function $C_{\boldsymbol{v}}(t)$ (2.58) to characterise time fluctuations. Fig. 4.3(b) shows that these decay over a timescale that depends strongly on the persistence time τ_p (and weakly on ϕ, see Fig. 4.2(d)).

Such correlated velocity patterns have no equilibrium analogue. They can be rationalised via the coupling of collective elastic modes and highly-persistent active forces [35] (see Sec. 2.4). At equilibrium, excitation of these elastic modes by thermal fluctuations affects displacements in two-dimensional passive glasses, a phenomenon known as Mermin-Wagner fluctuations [141, 165]. In order to assess the effect of these fluctuations, it is useful to consider the displacements of the particles with respect to their initial neighbours (their *cage*) (2.44), and compute their variance, *i.e.* the cage-relative MSD. The comparison between the MSD and its cage-relative counterpart (see Figs. 3.1(a, b), 3.2) reveals that these two quantities are fairly similar. We thus conclude that the relaxation motion of particles in dense systems is not controlled primarily by long wavelength modes. This also confirms that (absolute) displacements are appropriate observables for characterising structural relaxation of the liquid.

4.2 Microscopic relaxation

We have identified the existence of decreased velocity variance and extended velocity correlations in dense and persistent systems. In this Section, we explore the consequences of these for the microscopic relaxation of persistent systems close to dynamical arrest.

On increasing density, the system becomes crowded, and diffusive motion sets in over a large timescale $\tau_\alpha(\phi)$ that increases rapidly with increasing ϕ. This is evidenced by the important change (in log scale) of the time scale of decorrelation of the dynamical overlap Q (2.43) in Fig. 4.5(a, b). At equilibrium, particle dynamics is triggered by infrequent thermally activated relaxation events characterised by a broad distribution of energy barriers, reflecting a rugged energy landscape [52]. This physical picture survives for modest values of the persistence time, as in Fig. 3.1(a), except that activated dynamics is now driven by a non-equilibrium coloured noise, as recently studied in simpler active situations [166, 167]. Therefore, glassy dynamics for weak persistence qualitatively resembles passive systems [79, 82].

The physics is radically different when the persistence time is large. Since particles are always in contact at these high densities, the natural time scale for relaxation is the two-particle interaction time τ_0. This contrasts with relatively dilute systems, where one should consider the collision time [129]. This opens a time window, $\tau_0 \ll t \ll \tau_p$, where particle dynamics is nearly arrested and $|\boldsymbol{v}_i| \ll |\boldsymbol{p}_i|$ (see Sec. 4.1). The forces stemming from particle interactions then nearly balance the self-propulsion forces, and the system is close to mechanical equilibrium. Such configurations correspond to local minima of an effective potential energy [168, 169]

$$U_{\rm eff}(\{\boldsymbol{r}_1,\dots,\boldsymbol{r}_N\},\{\boldsymbol{p}_1,\dots,\boldsymbol{p}_N\}) = U(\{\boldsymbol{r}_1,\dots,\boldsymbol{r}_N\}) - \sum_{i=1}^{N}\left(\boldsymbol{p}_i - \frac{1}{N}\sum_{j=1}^{N}\boldsymbol{p}_j\right)\cdot\boldsymbol{r}_i, \tag{4.1}$$

which depends on both positions and propulsions. Because $U_{\rm eff}$ evolves slowly over a timescale $\tau_p \gg \tau_0$, a mechanical equilibrium at time t may be unstable at time $t+\tau_p$, because the propulsion forces will have significantly evolved via (2.16). This activity-induced loss of mechanical equilibrium triggers fast particle rearrangements [34] (on a timescale $\sim \tau_0$), as the system relaxes towards a new minimum of $U_{\rm eff}$. This effect is illustrated in Fig. 4.4(c), which shows the squared gradient of $U_{\rm eff}$ as a function of time. The succession of spikes correspond to rearrangement events. These results demonstrate that the intermittent dynamics at large τ_p constitutes a different relaxation mechanism than the activated relaxation events at weak persistence [52, 53, 135].

Intermittent dynamics between mechanical equilibria superficially resembles plasticity in slowly sheared amorphous solids in which smooth elastic deformations are interrupted by sudden plastic rearrangements [58]. In this regime, the spatially correlated velocity field at $t=0$ does not dictate the displacements associated with structural relaxation. To see this, note the weak correlations between Fig. 4.4(a) showing the velocity at time $t=0$ and Fig. 4.4(b) showing the displacement field over time $t\sim\tau_\alpha$. These snapshots should be contrasted with the analogous ones for the persistent liquid (see Figs. 4.2(a, b)), where velocities and displacements are strongly correlated. (The time scales were chosen such that the MSD is similar in both cases.) In fact, the displacement field in the glassy case (Fig. 4.4(c)) results from the accumulation of smaller particle rearrangements. We will explore the analogy with sheared amorphous solids further in Chap. 5.

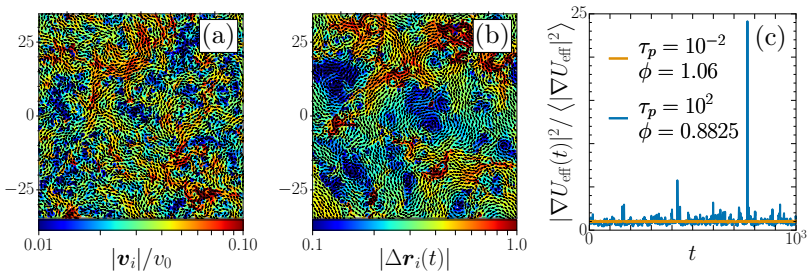

Figure 4.4: (a) Snapshot of the velocity field at time $t=0$. Colours indicate the norm and arrows their direction. (b) Snapshot of the displacement field at time $t/\tau_p = 200$ (MSD$(t) = 0.13$). Colours indicate the norm and arrows their direction. (c) Time series of the squared gradient of effective potential energy $|\nabla U_{\rm eff}(t)|^2 = (1/N)\sum_{i=1}^{N}|\boldsymbol{v}_i(t)|^2$ rescaled by its time-averaged value. Parameter values: $D_0 = 1$, (a, b) $N = 4096$, $\tau_p = 10^2$, $\phi = 0.8825$, (c) $N = 1024$.

4.3 Dynamical heterogeneity

We have established that elementary relaxation events were of a different nature in dense passive systems and dense persistent systems. At equilibrium, the global relaxation process is heterogeneous, and even more so as the relaxation time increases [52, 54, 59]. We will explore how the heterogeneity of this process is affected by non-equilibrium velocity correlations.

While it might be desirable to analyse relaxation events individually, τ_p is finite in our simulations, so changes in U_{eff} (4.1) are not quasistatic. This makes individual rearrangements hard to characterise, a problem which is familiar from equilibrium supercooled liquids [54]. Hence we analyse the dynamics using tools from that context. We start with the non-Gaussian parameter [144, 155]

$$\alpha_2(t) = \frac{(1/N)\sum_{i=1}^{N}\left\langle|\Delta \boldsymbol{r}_i(t)|^4\right\rangle}{2\left((1/N)\sum_{i=1}^{N}\left\langle|\Delta \boldsymbol{r}_i(t)|^2\right\rangle\right)^2} - 1, \tag{4.2}$$

which is zero when the distribution of particle displacements is Gaussian, and greater than 0 for fat-tailed distribution. In the small-persistence ($\tau_p = 10^{-2}$) liquid (see Fig. 4.5(c)), we recover the equilibrium behaviour [144–146]. The distribution of velocities is Gaussian, and so is the small-time displacement distribution. Then the distribution is maximally non-Gaussian around the relaxation time scale τ_α. The maximum height of α_2 increases with increasing τ_α (which increases with increasing packing fraction ϕ) which indicates increasing dynamical heterogeneity. At large times, information about the initial positions is lost, and the distribution of displacements is again Gaussian. In the persistent moderate-density liquid (see Fig. 4.5(d), $\phi \lesssim 0.87$) the dominant source of heterogeneity is the correlated velocities which decay on the time scale τ_p. Hence $\alpha_2(t)$ decays monotonically from the non-Gaussian value for the velocity distribution at $t = 0$ to the Gaussian diffusive limit at $t \gg \tau_p$. For larger ϕ, $\alpha_2(t)$ starts off similar to the active liquid, but it increases again for $t > \tau_p$, leading to a maximum at a much longer timescale $\tau_\alpha \gg \tau_p$. This peak shows that the slow relaxation dynamics is strongly non-Gaussian, supporting the picture of intermittent transitions [146] between minima of U_{eff}.

To quantify the collective nature of the dynamics we study the dynamical susceptibility [54] (2.48)

$$\chi_4(t,a) = N\left[\langle Q^2(t,a)\rangle - \langle Q(t,a)\rangle^2\right], \tag{4.3}$$

where Q is the dynamical overlap (2.43). We plot these susceptibilities as functions of both the length scale a and time scale t in Fig. 4.6, for both a small-persistence ($\tau_p = 10^{-2}$) and a large-persistence ($\tau_p = 10^2$) dense liquid. We superimpose on this plot a line showing the standard deviation of displacements as a function of time. As a dynamical susceptibility, $\chi_4(t,a)$ is related to the typical number of particles involved in some correlated motion. Here we have chosen this motion to be a displacement greater than length a over time t. In

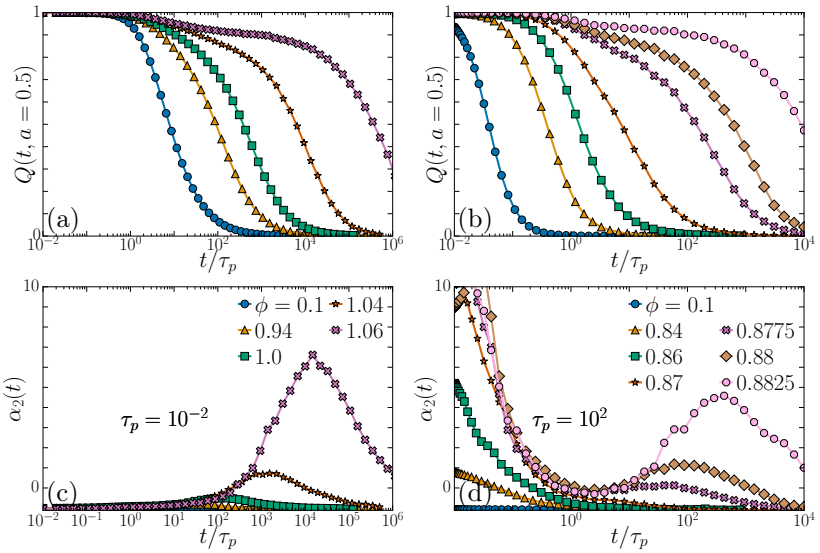

Figure 4.5: (a, b) Dynamical overlap as a function of time $Q(t,a)$ (2.43) for length scale $a = 0.5$ and different packing fractions ϕ at fixed τ_p. (c, d) Non-Gaussian parameter of displacements as a function of time $\alpha_2(t)$ (4.2) for different packing fractions ϕ at fixed τ_p. Parameter values: $N = 1024$, $D_0 = 1$, (a, c) $\tau_p = 10^{-2}$, (b, d) $\tau_p = 10^2$.

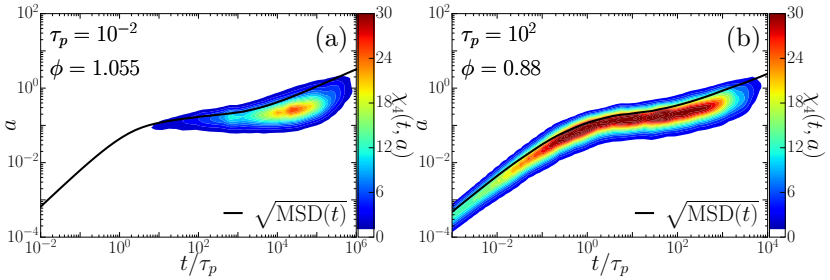

Figure 4.6: Dynamical susceptibility as a function of length and time $\chi_4(t, a)$ (4.3) superimposed with the standard deviation of displacement as a function of time $\sqrt{\text{MSD}(t)}$ (2.36). Parameter values: $N = 1024$, $D_0 = 1$, (a) $\tau_p = 10^{-2}$, $\phi = 1.055$, (b) $\tau_p = 10^2$, $\phi = 0.88$.

dense passive systems, $\chi_4(t, a)$ is only sizeable (*i.e.* it reveals significant correlations between displacements) if $t \sim \tau_\alpha$ and a is close to the typical cage size [170], thus capturing the cooperative nature of activated relaxation. This time scale and this length scale can be identified in the plot: these are respectively the average height in the intermediate subdiffusive regime (*i.e.* caging regime), and the crossover time to the diffusive regime. This is confirmed by Fig. 4.6(a). In dense persistent systems, $\chi_4(t, a)$ is large at all times up to τ_α, and is maximised for a given t for $a \sim \sqrt{\Delta r^2(t)}$. These data quantitatively confirm that, due to velocity correlations, particle displacements are spatially correlated over a broad range of time scales in very persistent glassy systems. This contrasts with results at low persistence, where the short-time correlations are absent, similar to the passive case.

4.4 Conclusion: large-persistence dense active liquid

We confirmed that at small persistence time $\tau_p \ll \tau_0$, the behaviour of the system is equilibrium-like. On the opposite limit, for $\tau_p \gg \tau_0$, we observe the emergence of extended velocity correlations, with a correlation length scale which increases with ϕ and τ_p, and a correlation time scale which scales with τ_p and depends weakly on ϕ. This is consistent with the existing literature [35, 103]. Given the question posed in the introduction to this Chapter, we now summarise how these non-equilibrium velocity correlations influence relaxation.

At large density, the dynamical arrest of these persistent liquids ($\tau_\alpha \gg \tau_p$) is accompanied by complex spatio-temporal correlations, spanning a range of length and time scales, whose origin differs qualitatively from active glasses analysed so far. At small times $t \ll \tau_p$, the exploration by a given particle of the cage formed by its neighbours (β-relaxation) is replaced with the coherent motion of particles alongside their neighbours, following their velocity correlations. At large times $t \sim \tau_\alpha \gg \tau_p$, cage escapes ($\alpha$-relaxation) are replaced with intermittent activity-induced rearrangements.

While slow dynamics are ubiquitous in crowded systems (both active and passive), a simple replacement of thermal noises by highly-persistent propulsions thus dramatically changes the mechanisms by which a liquid explores its energy landscape. These results provide further evidence that very active glasses are novel states of matter, with distinct properties from equilibrium glasses [34, 168, 171]. We will explore in Chap. 5 how the intermittent dynamics of the persistent active glass can be understood by analysing the idealised limit of large τ_p [169].

5 | Activity-driven dynamics

We established that, in large-persistence ($\tau_p \gg \tau_0$) dense systems, neighbouring particles which are propelled against each other tend to stick [81, 82] (see Sec. 3.2). A first consequence of this is the emergence of extended velocity correlations [35, 36, 78, 79, 88, 103] (see Sec. 2.4). A second consequence is that, close to dynamical arrest, intermittent elementary rearrangements do not result from activation events (see Sec. 4.2). They rather are the consequence of an activity-driven destabilisation of an effective potential [168, 169]. Despite this difference in nature, we recover heterogeneous relaxation dynamics on time scales $\tau_\alpha \gg \tau_p$ (see Sec. 4.3).

The study of large-persistence systems close to dynamical arrest is computationally challenging. First, because $\tau_p < \infty$, it is impossible to study individual rearrangements. Second, because the equations of motion are integrated on a time scale $\delta t \lesssim \tau_0$ while the relaxation time scale is $\tau_\alpha \gg \tau_p \gg \tau_0$, it is extremely arduous to directly simulate these steady state of these systems with conventional methods. To tackle both problems, a recent method was devised, *activity-driven dynamics* (ADD) [168, 169], which quasistatically simulates the dynamics of athermal self-propelled particles in the limit of $\tau_p \to \infty$. This enables us to study the microscopic relaxation in extremely persistent active matter close to dynamical arrest.

In this Chapter, we will first show that ADD relaxation is built on two fundamental processes as in other athermal quasistatic methods such as *athermal quasistatic shear* (AQS) [58]. These are smooth elastic deformations, where the particles deform weakly near an energy minimum in response to the slowly-varying self-propulsion forces, and sudden plastic rearrangements or avalanches in which a local minimum of the energy landscape becomes unstable, forcing the system towards a new one. We characterise these two processes in detail, including quantitative comparisons with AQS. We then explore how particles move and relax in the steady states of ADD. As we might expect for a dense disordered system with slow dynamics, we find cooperative heterogeneous relaxation. We analyse this motion using a range of techniques borrowed from passive glassy systems [54], including distributions of particle displacements, correlation functions tailored for structural relaxation, and four-point susceptibilities.

Some of the results of this Chapter were published in Ref. [172].

Contents

5.1 Effective quasistatic dynamics

In this Section, we describe the principle and implementation of ADD. We will first discuss how taking the $\tau_p \to \infty$ leads to intermittent dynamics, and how ADD exploits this to approximate the effective dynamics. Taking this limit reduces by one the number of control parameters, as a matter of simplicity we will also only consider fixed number density $\rho = 1.2$. We will discuss this choice in Sec. 5.1.2 which details how this method is used in practice.

5.1.1 Intermittent dynamics and activity-driven dynamics

The central ideas are first that, in the presence of fixed propulsion forces and absence of thermal excitations, the system will converge to a force-balanced configuration in a finite time of order $\tau_r \gtrsim \tau_0$ [168, 169], at the condition that these propulsion forces are not too strong. (For larger forces, the system yields and there is no convergence to any mechanical equilibrium [34, 173, 174].) Then, setting a large yet finite persistence time $\tau_p \gg \tau_r$, propulsion forces are constant on time scales $\tau_r \lesssim t \ll \tau_p$. Therefore, the system is able to reach a force-balanced state in a time of order τ_r, and the system configuration remains almost constant until the propulsion forces change significantly, which requires a time of order τ_p. Eventually, these forces will change sufficiently to destabilise the force-balanced state, at which point the system must switch to a new force-balanced configuration, which involves significant particle motion.

The resulting intermittent dynamical motion has several important consequences. First, it means that standard simulation methods become inefficient because they require a time step $\delta t \lesssim \tau_0 \ll \tau_p$. ADD circumvents this problem by replacing the explicit dynamical integration over times of order $\tau_r \gtrsim \tau_0$ with an energy minimisation step. This offers a computational speedup of order τ_p/τ_0, which is large in extremely persistent active matter. Second, the intermittent mechanism of ADD relaxation (which involves long quiescent periods punctuated by large sudden motions) means that these systems share similarities with other physical systems where athermal quasistatic motion is relevant. These include amorphous solids under athermal quasistatic shear (AQS) [58], and active matter systems undergoing an athermal quasistatic random displacement (AQRD) protocol [38].

In all these contexts, a system evolves in response to potential gradients and the potential evolves quasistatically: the resulting motion is mostly quasistatic, but sudden relaxation events are triggered when the local minimum of the potential deforms into a saddle point. Such events are known as avalanches, because large-scale motion can be triggered after an infinitesimal local change [175–177].

In addition to similarities with AQS and AQRD, the ADD method is also related to the athermal quasistatic random force (AQRF) protocol of Ref. [38]. However, ADD is distinct from all these methods. Specifically, both AQS and AQRD displace particles along a fixed driving direction and particles move orthogonally to the drive to minimise their interaction energy. This leads to sustained stick-slip motion, including avalanches. By contrast, AQRF applies forces with fixed direction. These are changed smoothly, which generates avalanches. However, increasing the force amplitude eventually drives the system through a yielding threshold [34, 173, 174], after which mechanical equilibrium is no longer reached and the system "flows". The essential features of ADD are that it controls the forces on particles (contrarily to AQS and AQRD), and that the directions of these forces change randomly with time while their typical strength remains constant (contrarily to AQRF). The result is a dynamical non-equilibrium steady state that exhibits stick-slip motion. This corresponds to the large-τ_p limit of the steady states previously observed in active matter, which also show highly intermittent motion [34] (see Sec. 4.2).

5.1.2 Implementation

We focus here on extremely persistent systems where $\tau_p \gg \tau_r \gtrsim \tau_0$. In this limit, it is convenient to introduce a rescaled time variable as

$$t' = t/\tau_p \,. \tag{5.1}$$

We also rescale the propulsion by defining $\tilde{\boldsymbol{p}}_i = \boldsymbol{p}_i/v_0$, with v_0 the self-propulsion velocity (2.10). It is convenient to work in the centre-of-mass frame so we write $\overline{\tilde{\boldsymbol{p}}} = (1/N)\sum_i \tilde{\boldsymbol{p}}_i$ and $\overline{\boldsymbol{r}} = (1/N)\sum_i \boldsymbol{r}_i$, which are the propulsive force acting on the particles' centre of mass and the position of the latter. In the centre-of-mass frame, (2.15, 2.16) become

$$\frac{1}{\tau_p}\frac{\mathrm{d}\boldsymbol{r}'_i}{\mathrm{d}t'}(t') = -\nabla_i U(t') + v_0\,[\tilde{\boldsymbol{p}}_i(t') - \overline{\tilde{\boldsymbol{p}}}(t')], \tag{5.2}$$

$$\frac{\mathrm{d}\tilde{\boldsymbol{p}}_i}{\mathrm{d}t'}(t') = -\tilde{\boldsymbol{p}}_i(t') + \sqrt{2}\,\boldsymbol{\eta}'_i(t'), \tag{5.3}$$

where $\boldsymbol{r}'_i = \boldsymbol{r}_i - \overline{\boldsymbol{r}}$ is the position relative to the centre of mass, and $\boldsymbol{\eta}'_i$ is a zero-mean Gaussian white noise in the rescaled time variables, that is, $\boldsymbol{\eta}'_i = \sqrt{\tau_p}\boldsymbol{\eta}_i$, which ensures that the components of $\boldsymbol{\eta}'_i$ satisfy $\langle \eta'_{i,\alpha}(t'_1)\eta'_{j,\beta}(t'_2)\rangle = \delta_{ij}\delta_{\alpha\beta}\delta(t'_1 - t'_2)$.

To arrive at the ADD limit, we take the limit $\tau_p \to \infty$ at fixed v_0. For large τ_p, (5.2) describes very fast relaxation to configurations with perfect force balance, which satisfy

$$\nabla_i U_{\mathrm{eff}} = 0, \tag{5.4}$$

where

$$U_{\rm eff} = U - v_0 \sum_j [\tilde{\boldsymbol{p}}_j(t') - \overline{\tilde{\boldsymbol{p}}}(t')] \cdot \boldsymbol{r}_j \tag{5.5}$$

is the same effective potential as (4.1), and corresponds to the original potential energy of the interacting particle system, tilted by the active forces. Hence, as $\tau_p \to \infty$, the system is almost always in a local minimum of $U_{\rm eff}$, as captured mathematically by (5.4).

The dynamics of our model can be simulated directly in the ADD limit [169], we summarise here the method for achieving this. The steady state distribution of the propulsions $\tilde{\boldsymbol{p}}_i$ factorises across particles (2.8), with

$$\text{Prob}(\tilde{\boldsymbol{p}}_i) = \frac{1}{2\pi} \exp\left(-\frac{1}{2}|\tilde{\boldsymbol{p}}_i|^2\right), \tag{5.6}$$

and we use this to randomly initialise the $\tilde{\boldsymbol{p}}_i$. In each step of the ADD simulation, the propulsion dynamics in (5.3) is first integrated with time step $\delta t'$ using Euler method

$$\tilde{\boldsymbol{p}}_i(t' + \delta t') = (1 - \delta t')\tilde{\boldsymbol{p}}_i(t') + \sqrt{2\,\delta t'}\,\tilde{\boldsymbol{\eta}}'_i, \tag{5.7}$$

where $\tilde{\boldsymbol{\eta}}'_i = (\tilde{\eta}'_{i,x}, \tilde{\eta}'_{i,y})$ are two random numbers drawn from a Gaussian distribution with zero mean and unit variance. Next one integrates (5.2), which requires that $U_{\rm eff}$ (5.5) is minimised by steepest descent, holding the $\tilde{\boldsymbol{p}}_i$ fixed. To increase computational efficiency, we replace this steepest descent by a faster conjugate gradient minimisation, using the GPL-licensed ALGLIB C++ library [178]. This is much more efficient than steepest descent, but it may generally lead to different local minima [179]. We find that the differences between conjugate gradient and steepest descent algorithms are significant only in steps for which the system moves far from its initial position. For these individual steps, we then automatically revert to steepest descent, as originally proposed in Ref. [169]. That is, we choose a threshold in the mean-squared displacement $(1/N)\sum_i |\delta \boldsymbol{r}_i|^2 > 0.1$ to identify minimisation steps with large total displacements. If this occurs during conjugate gradient minimisation then we restart the minimisation step and use steepest descent for that particular step. We stress that each of these minimisation step requires on average 10^2-10^3 force evaluations. It is thus numerically challenging to explore both large systems and the large times needed to reach steady state. We will therefore show data for $N \leq 2000$.

We highlight that the continuity of the second derivative of the potential is a necessary condition for the convergence of our conjugate gradient algorithm. This condition is not satisfied by the WCA potential (2.17). We will substitute it with a regularised inverse power law $1/r^{12}$ pairwise additive potential [180] with

$$U_{ij} = \varepsilon \left[\frac{1}{(r_{ij}/\tilde{\sigma}_{ij})^a} + c_0 + c_1(r_{ij}/\tilde{\sigma}_{ij})^2 + c_2(r_{ij}/\tilde{\sigma}_{ij})^4\right] \Theta(r_c - r_{ij}/\tilde{\sigma}_{ij}), \tag{5.8a}$$

$$\tilde{\sigma}_{ij} = \frac{\sigma_i + \sigma_j}{2}(1 - 0.2|\sigma_i - \sigma_j|), \tag{5.8b}$$

$$a = 12,\ r_c = 1.25,\ c_0 = -\frac{8 + a(a+6)}{8r_c^a},\ c_1 = \frac{a(a+4)}{4r_c^{a+2}},\ c_2 = -\frac{a(a+2)}{8r_c^{a+4}}. \tag{5.8c}$$

As with WCA (2.17), this is a purely repulsive soft interaction potential which diverges at the origin. The coefficients c_0, c_1, and c_2 make the potential and its first two derivatives continuous at the cut-off distance r_c , and the pair interaction is slightly non-additive to improve the glass-forming ability of the system.

The ADD construction is valid for self-propulsion velocities v_0 below an N-dependent yielding threshold $v_0^*(N)$. The potential $U_{\rm eff}$ is not bounded below so steepest descent may not converge to a local minimum, instead the particles could continue to move along their self-propulsion directions. This happens for $v_0 > v_0^*$. The rheology and phase behaviour of the system above this threshold is explored in Ref. [174]. In order to estimate the yielding threshold as a function of the system size $v_0^*(N)$, we start standard molecular dynamics simulations from random initial configurations which satisfy $\nabla_i U \approx 0$, and set constant propulsions with distribution (2.8) and variance $2v_0^2$. For each system size N and self-propulsion velocity v_0, we perform 100 simulations up to time $t_{\rm f} = 500\tau_0$ (note that Ref. [169] considered times $t \leq 250\tau_0$ for their steepest-descent minimisation). We finally check how many of these simulations have a velocity standard deviation $\sqrt{\left\langle (1/N)\sum_{i=1}^N |\boldsymbol{v}_i(t_{\rm f})|^2 \right\rangle} > 10^{-6}$. The latter are considered as simulations which are still flowing [173]. We obtain the following rough estimates at $\rho = 1.2$ by determining for each N at which v_0 half of the simulations are still flowing: $v_0^*(N = 500) \approx 1.7$, $v_0^*(N = 1024) \approx 1.4$, $v_0^*(N = 2000) \approx 1.2$, $v_0^*(N = 4096) \approx 1.1$. Given these systematic finite-size effects, it would be desirable to simulate even larger systems. However, we emphasize that a single time step for ADD is much more expensive than a single time step in a standard molecular dynamics simulation, because it requires many evaluations of the interparticle forces to converge the energy minimisation. This stems from the intrinsic

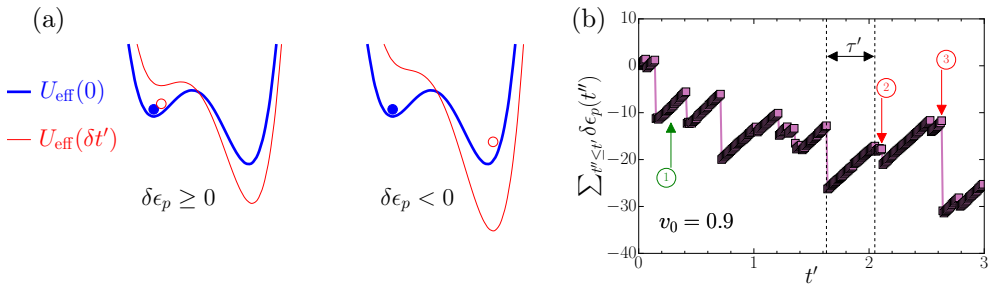

Figure 5.1: (a) Sketch of the effective potential energy landscape $U_{\rm eff}$ in (5.5) at times 0 (thick blue line) and $\delta t'$ (thin red line). The system initially rests in a minimum of $U_{\rm eff}(0)$ (filled blue circle). After $\delta t'$, the system rests in a minimum of the new landscape $U_{\rm eff}(\delta t')$, and it is displayed in the initial landscape (open red circle). We distinguish elastic events ($\delta\epsilon_p \geq 0$) for which the systems remains close to its original position, and thus the potential energy in $U_{\rm eff}(0)$ increases, and plastic events ($\delta\epsilon_p < 0$) for which a rearrangement occurs. (b) Accumulated variations of the effective potential energy, $\sum_{t''\leq t'} \delta\epsilon_p(t'')$. We identify elastic branches made of successive elastic events (*e.g.* event ①) as ascending lines, and plastic events (*e.g.* events ② and ③) as instantaneous large drops. Parameter values: $N = 1024$, $v_0 = 0.9$, $\delta t' = 10^{-2}$, purple square symbols separated by $\delta t'$.

difficulty of simulating systems with well-separated time scales ($\tau_p/\tau_0 \to \infty$). This limit is inaccessible using standard methods: it can be simulated using ADD, but there is still a significant cost.

In the ADD dynamics for $v_0 < v_0^*$, each step starts with the system in a local minimum of $U_{\rm eff}$ with positions and propulsions $(\{\boldsymbol{r}_1^0, \dots, \boldsymbol{r}_N^0\}, \{\boldsymbol{p}_1^0, \dots, \boldsymbol{p}_N^0\})$, and evolves to a new minimum with positions and propulsions $(\{\boldsymbol{r}_1, \dots, \boldsymbol{r}_N\}, \{\boldsymbol{p}_1, \dots, \boldsymbol{p}_N\})$. This can happen in two ways, as sketched in Fig. 5.1(a). In the simplest case, a small change in propulsion forces changes the local minimum of $U_{\rm eff}$ perturbatively, leading to small displacements. This will be called an elastic step. However, the change in propulsive forces can also destabilise the local minimum at $(\{\boldsymbol{r}_1^0, \dots, \boldsymbol{r}_N^0\}, \{\boldsymbol{p}_1^0, \dots, \boldsymbol{p}_N^0\})$, leading to a non-perturbative change in the configuration. This is called a plastic step.

To distinguish these two cases, we compute the change in effective potential in one step:

$$\delta\epsilon_p = U(\{\boldsymbol{r}_1, \dots, \boldsymbol{r}_N\}) - U(\{\boldsymbol{r}_1^0, \dots, \boldsymbol{r}_N^0\}) - v_0 \sum_i (\tilde{\boldsymbol{p}}_i^0 - \overline{\tilde{\boldsymbol{p}}^0}) \cdot (\boldsymbol{r}_i - \boldsymbol{r}_i^0). \tag{5.9}$$

This sign convention is opposite to that of Ref. [169]. We will denote $\delta\boldsymbol{r}_i = \boldsymbol{r}_i - \boldsymbol{r}_i^0$ the single-step displacement of particle i. Note that the propulsions in this equation are those of the state before the ADD step, with the consequence that perturbative changes in the positions lead to positive $\delta\epsilon_p$ as the system moves away from the minimum of the associated $U_{\rm eff}$. Hence, we identify elastic steps as those with $\delta\epsilon_p \geq 0$ while those with $\delta\epsilon_p < 0$ are plastic, as illustrated in Fig. 5.1(a). We define τ' as the time between two consecutive plastic events. We discuss these two types of step separately in detail in Sec. 5.2.

As well as the system parameters, a numerical simulation of ADD also requires a choice of time step $\delta t'$. As usual, this should be small enough to mimic the limit $\delta t' \to 0$, but large enough to ensure computational efficiency. In practice, we perform ADD simulations (using steepest descent as the minimisation algorithm) for different time steps $\delta t'$. We then compute the average squared displacement $d^2_{\rm rms}$, separately for elastic and plastic steps. For elastic steps, we expect the trivial scaling $d^2_{\rm rms} \sim \delta t'$ [169]. For plastic steps, we observe on the contrary that $d^2_{\rm rms}$ plateaus at small time steps $\delta t'$ and is an increasing function of $\delta t'$ at large $\delta t'$. We choose the optimal $\delta t'$ as the time step when $d^2_{\rm rms}$ starts to deviate from its low-time-step limit.

As for performances, we compare minimisation procedures with respect to their number of force evaluations, which we expect to be the most time-consuming part of the algorithm. We report that (for $v_0 = 0.9$, $N = 1024$, $\delta t' = 10^{-2}$) on average 93% of steps are elastic and 7% are plastic. Compared to standard steepest descent (SD), our conjugate gradient (CG) algorithm [178] is on average 93-fold faster on elastic steps and 22-fold faster on plastic steps. We compute the following total acceleration from SD to CG

$$\frac{p^{\rm SD}_{\rm plastic}\overline{N}^{\rm SD}_{\rm plastic} + p^{\rm SD}_{\rm elastic}\overline{N}^{\rm SD}_{\rm elastic}}{p^{\rm CG}_{\rm plastic}\overline{N}^{\rm CG}_{\rm plastic} + p^{\rm CG}_{\rm elastic}\overline{N}^{\rm CG}_{\rm elastic}} \approx 64\text{-fold} \tag{5.10}$$

where p^α_β denotes the proportion of β (= plastic or elastic) steps using algorithm α (= SD or CG), and $\overline{N}^\alpha_\beta$ denotes the average number of force evaluations in β steps using algorithm α.

We have taken the limit $\tau_p \to \infty$ and will only consider fixed number density $\rho = 1.2$. We are thus left with two control parameters: the number of particles N and the self-propulsion velocity v_0. For fixed v_0, we expect

the behaviour to be robust with respect to ρ, as long as ρ is not too large (complete jamming) or too small (no force balanced states, *i.e.* flow).

5.2 Analysis of individual events

A typical trajectory from ADD is shown in Fig. 5.1(b). It consists of sequences of elastic steps ($\delta\epsilon_p$ is positive and $O(\delta t')$), interspersed with instantaneous plastic events ($\delta\epsilon_p$ is negative and $O(1)$). Such behaviour is familiar from AQS simulations of sheared glasses [58] as well as from AQRD simulations [38] and the non-equilibrium dynamics of the random-field Ising model (RFIM, where the plastic events would be identified as avalanches) [177].

This Section analyses the properties of the elastic and plastic steps, including a quantitative comparison with AQS. We take $v_0 = 0.9$ throughout this section. This is a practical choice: on the one hand it is far enough from the threshold v_0^* to keep the system from moving too much between minimisations, on the other hand smaller values of v_0 lead to slower dynamics and the numerics become more challenging.

5.2.1 Elastic steps

A representative snapshot of the displacement field obtained during an elementary elastic step of the ADD dynamics is shown in Fig. 5.2(a). We observe highly heterogeneous displacements, with wide variations in amplitude and clear large-scale correlations resembling both non-affine displacement in sheared athermal glasses [149] and collective swirling motion in active matter [35] (see Sec. 4.1).

Elastic steps can be analysed under the assumption that the updated propulsive forces move the minimum of U_{eff} perturbatively, in a way similar to AQS [58, 149]. We will use this approximation to derive analytic predictions for the elastic displacements and their spatial correlations.

The states before and after the elastic step are both force balanced, so for all i

$$\delta\left[-\nabla_i U + v_0(\tilde{\boldsymbol{p}}_i - \bar{\tilde{\boldsymbol{p}}})\right] = 0, \tag{5.11}$$

where δ indicates the change in a time increment $\delta t'$. In the limit of $\delta t' \to 0$, we can use a harmonic approximation so the equation above can be written as

$$\delta\left[-\frac{\partial}{\partial r_{i\gamma}}U + v_0(\tilde{p}_{i\gamma} - \bar{\tilde{p}}_\gamma)\right] = -\sum_{j,\delta} H_{i\gamma,j\delta}\delta r_{j\delta} + \Xi_{i\gamma} = 0, \tag{5.12}$$

where Greek indices are used for spatial dimensions and Latin indices for particles, and where we have introduced $\mathbb{H}$ the Hessian matrix (2.56) of U whose coefficients are

$$H_{i\gamma,j\delta} = \frac{\partial^2}{\partial r_{i\gamma}\partial r_{j\delta}}U, \tag{5.13}$$

and introduced $\boldsymbol{\Xi}_i$

$$\begin{aligned}\Xi_{i\gamma} &= v_0(\delta\tilde{p}_{i\gamma} - \delta\bar{\tilde{p}}_\gamma)\\ &= v_0\left(-\tilde{p}_{i\gamma}\delta t' + \sqrt{2\,\delta t'}\eta'_{i\gamma} - \delta\bar{\tilde{p}}_\gamma\right),\end{aligned} \tag{5.14}$$

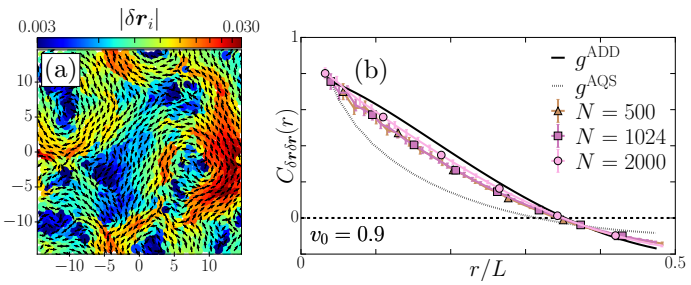

Figure 5.2: (a) Snapshot of displacements for a single elastic step (① in Fig. 5.1). Colours indicate the norm and arrows their direction. (b) Corresponding displacement correlation function $C_{\delta\boldsymbol{r}\delta\boldsymbol{r}}(r)$, defined on the model of velocity correlations (2.57) where the single-step displacement $\delta\boldsymbol{r}_i$ replaces the velocity $\boldsymbol{v}_i$, for various N values. Solid (resp. dotted) line: evaluation of (5.22) (resp. (5.23)) with sums across the range $0 < m^2 + n^2 < 40^2$ and a suitably chosen overall prefactor. Parameter values: $v_0 = 0.9$, $N = 1024$, $\delta t' = 10^{-2}$.

which is the analogue of the affine force in the AQS setting of Ref. [58], where the term $\delta\bar{\tilde{\boldsymbol{p}}}$ only ensures $\sum_i \boldsymbol{\Xi}_i = 0$ so that we stay in the centre-of-mass frame.

We solve (5.12) for the displacements $\delta r_{i\gamma}$. We first invert this relation to write

$$\delta r_{i\gamma} = \sum_{j,\delta} (H^{-1})_{i\gamma,j\delta} \Xi_{j\delta}. \tag{5.15}$$

The Hessian matrix $\mathbb{H}$ is symmetric and real-valued thus, by virtue of the spectral theorem, there exists an orthonormal basis of eigenvectors $\boldsymbol{e}_a$, associated with eigenvalues Λ_a, that diagonalises it:

$$H_{i\gamma,j\delta} = \sum_a \Lambda_a e_{a,i\gamma} e_{a,j\delta}. \tag{5.16}$$

Introducing the projection of the affine force along eigenvector $\boldsymbol{e}_a$,

$$\Xi_a = \sum_{j,\delta} \Xi_{j\delta} e_{a,j\delta} \tag{5.17}$$

and employing the diagonalised form of the Hessian, (5.15) then becomes

$$\delta r_{i\gamma} = \sum_a \Xi_a \Lambda_a^{-1} e_{a,i\gamma}. \tag{5.18}$$

Here we have implicitly omitted eigenvectors with zero eigenvalues $\Lambda_a = 0$: these correspond to translations, which are explicitly excluded from $\delta r_{i\gamma}$ as we work in the centre-of-mass frame.

To evaluate (5.18) approximately, we follow Ref. [58] in assuming the eigenvectors of $\mathbb{H}$ are the longitudinal ($||$) and transverse ($\perp$) plane wave eigenstates of the Navier operator [149, 153] for the displacement field in an elastic medium, with the associated eigenvalues proportional to the square of the wavevector,

$$a \equiv (m, n, \alpha), \quad \Xi_a \equiv \Xi^\alpha_{mn}, \tag{5.19a}$$

$$e_{a,i\gamma} \approx \exp(\mathrm{i}\boldsymbol{k}_{mn} \cdot \boldsymbol{r}_i)\, \hat{k}^\alpha_{mn\gamma}/N, \quad \Lambda_a \approx \lambda^\alpha (m^2 + n^2)/N \tag{5.19b}$$

where $\alpha = ||, \perp$ is the polarisation direction, $\boldsymbol{k}_{mn} = (2\pi m/L, 2\pi n/L)$ is the wavevector, $\hat{\boldsymbol{k}}^{||}_{mn} = \boldsymbol{k}_{mn}/|\boldsymbol{k}_{mn}|$, and $\hat{\boldsymbol{k}}^{\perp}_{mn} = \hat{\boldsymbol{z}} \wedge \hat{\boldsymbol{k}}^{||}_{mn}$. The displacement field (5.18) can then be written as

$$\delta r_{i\gamma} = \sum_{m,n,\alpha} \Xi^\alpha_{mn} \frac{e^{\mathrm{i}\boldsymbol{k}_{mn}\cdot\boldsymbol{r}_i} \hat{k}^\alpha_{mn\gamma}}{\lambda^\alpha (m^2 + n^2)} \tag{5.20}$$

where the third sum is over the two polarisation $\alpha = ||, \perp$.

It is then possible to compute the spatial correlation function

$$\begin{aligned} g^{\mathrm{ADD}}(\boldsymbol{r}) &\propto \langle \delta\boldsymbol{r}_i \cdot \delta\boldsymbol{r}_j\, \delta(\boldsymbol{r} - (\boldsymbol{r}_j - \boldsymbol{r}_i)) \rangle \\ &= \sum_{m,n,\alpha} \frac{\left\langle |\Xi^\alpha_{mn}|^2 \right\rangle}{(\lambda^\alpha (m^2 + n^2))^2} e^{\mathrm{i}\boldsymbol{k}_{mn}\cdot\boldsymbol{r}}, \end{aligned} \tag{5.21}$$

where we have checked numerically that the projections of the affine force $\boldsymbol{\Xi}_i$ on the eigenmodes of the Hessian $\mathbb{H}$ behave as uncorrelated random numbers, with a variance $\left\langle |\Xi^\alpha_{mn}|^2 \right\rangle$ independent of the specific mode. We finally take the orientational average of (5.21) to write

$$g^{\mathrm{ADD}}(r) \propto \sum_{m,n} \frac{J_0\left(2\pi\sqrt{m^2+n^2}\, r/L\right)}{(m^2+n^2)^2}, \tag{5.22}$$

where J_0 is the zeroth-order Bessel function of the first kind. Our result is quantitatively different from the corresponding correlation function for sheared amorphous solids [149]

$$g^{\mathrm{AQS}}(r) \propto \sum_{m,n} \frac{J_0\left(2\pi\sqrt{m^2+n^2}\, r/L\right)}{m^2+n^2}\,. \tag{5.23}$$

The difference between (5.22, 5.23) arises because affine forces $\boldsymbol{\Xi}_i$ in AQS are derived from pair potentials: the force exerted by particle i on particle j is equal and opposite to the one exerted by particle j on particle i.

Hence, the affine forces on different particles are necessarily correlated in AQS. Still, both functions correspond to scale-free correlations, with the only relevant length scale being the system size L itself. Qualitatively, this behaviour is visible already from the system-spanning vortices in the displacement field shown in Fig. 5.2(a).

We compute the displacement correlation numerically in Fig. 5.2(b). The collapse with r/L for three different system sizes shows that correlations scale with the system size for the range of sizes we have investigated, and are close to the analytical prediction (5.22). These correlations are negative at large r/L. The small difference between the prediction and the measurement may be attributed to the plane wave hypothesis, which can in principle be tested [181]. We have also checked that the above correlation functions are consistent with the correlations computed from purely harmonic steps, i.e. with displacements determined by solving (5.12) exactly. This establishes another parallel to Ref. [149].

The scaling with system size of the displacement correlations that we find is consistent with the arguments obtained for finite persistence time in Ref. [35]. In that case, the dynamics along elastic trajectory segments produces displacement (or equivalently velocity) correlations on a length scale that diverges as $\sim \sqrt{\tau_p}$ for large persistence times. As our analysis takes $\tau_p \to \infty$ from the start, this limit translates into displacement correlations on the largest length scale available, *i.e.* the system size.

5.2.2 Plastic steps

Particle displacements for two representative plastic steps are shown in Figs. 5.3(a,b). The qualitative picture has again many similarities with AQS: the displacements in any single plastic event can be interpreted as sequences of localised yielding events [58, 169]. That is, a plastic step happens when a local minimum of U_{eff} develops an unstable direction, causing local motion. However the elastic perturbation due to this event perturbs the system over large length scales and can create further unstable directions in other parts of the system. This leads to a cascade or avalanche of localised yielding events. We describe these plastic events here and discuss similarities and differences with AQS.

We find that plastic avalanches display a broad range of sizes and can involve a few localised particles, as in Fig. 5.3(a), or a greater number of particles distributed across the system as in Fig. 5.3(b), or even the whole system. To characterise the participation in each plastic event, we identify the number S of particles with significant changes in their local environments. In Ref. [169] this identification was carried out by thresholding particle displacements, but such a criterion neglects the fact that particles may collectively move large distances

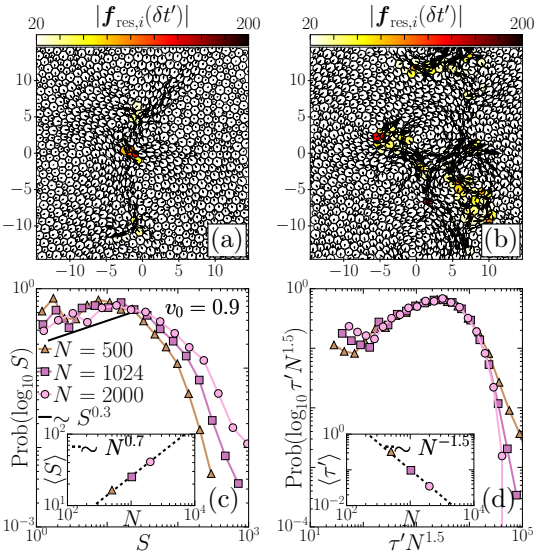

Figure 5.3: (a, b) Snapshots showing the movement of particles in the two plastic events marked ② and ③ in Fig. 5.1, with participation $S = 19$ and $S = 102$, respectively. Displacements are magnified 5 times and superimposed onto a colormap of the residual force $|\boldsymbol{f}_{\text{res},i}|$ that highlights rearranging particles. (c) Log-distribution of the participation S in plastic events, for three system sizes N and time steps $\delta t'(N = 500) = 2 \times 10^{-3}$, $\delta t'(N = 1024) = 10^{-3}$, $\delta t'(N = 2000) = 5 \times 10^{-4}$. The solid black line corresponds to a scaling $P(S) \sim P(\log_{10} S)/S \sim S^{0.3-1} = S^{-0.7}$. Inset shows the evolution of the mean $\langle S \rangle$ with N. (d) Log-distribution of times τ' between consecutive plastic events. Inset shows the evolution of the mean $\langle \tau' \rangle$ with N. Scaling exponents are subject to significant uncertainties and the numbers provided are indicative. Parameter values: $N = 1024$, $v_0 = 0.9$, $\delta t' = 10^{-2}$.

without changing their local environment. Here, we use instead the residual force $\boldsymbol{f}_{\mathrm{res},i}$ [182, 183] (see App. A for definition) as an indicator of rearrangements. This force is zero if and only if displacements result from a harmonic response of the system to the change in propulsion forces. If a localised avalanche takes place, particles that are far from the avalanche tend to respond elastically, leading to very low residual forces, whereas rearranging particles in the core of the avalanche have large residual forces. This is illustrated in Fig. 5.3(a,b). We then define the avalanche size S as the number of particles for which $|\boldsymbol{f}_{\mathrm{res},i}(\delta t')| > 20$, determined after careful analysis of the distributions of $\boldsymbol{f}_{\mathrm{res},i}$ (see App. A).

Fig. 5.3(c) shows the resulting broad distribution of $\log_{10} S$ for three system sizes. The small events can be attributed to local yielding, in which the remainder of the system reacts elastically with particles moving collectively to accommodate the local rearrangement [169, 183]. At low values of S, the distributions overlap for different system sizes, with a behaviour compatible with $P(S) \sim S^{-\tau}$ with $\tau \approx 0.7$. (We use the notation τ here, which is standard in the literature [184], τ does not indicate a time scale.) Given the small range of system sizes studied here, it is difficult to provide a very precise estimate of τ, but it is clearly distinct from the values found in AQS simulations of sheared glasses where values in the range $\tau \approx 1.2 - 1.5$ have been reported [176, 184].

Turning to the behaviour at large S we observe that larger avalanches with $S \sim N$ are more frequent for larger systems, suggesting that these are also important in ADD. Correspondingly, the inset in Fig. 5.3(c) shows that the average event size $\langle S \rangle$ scales as N^{γ} with $\gamma \approx 0.7$, showing that the mean avalanche size is indeed controlled by large avalanches that are limited by the system size only. In other words, the avalanches observed during plastic events also lead to scale-free dynamic relaxation events.

Fig. 5.3(d) shows the distribution of waiting times τ' between consecutive events. The average time decreases with system size as $\langle \tau' \rangle \sim N^{-1.5}$. If localised yielding events happened independently in different parts of a large system, one would have a more trivial dependence on the system size, $\langle \tau' \rangle \sim N^{-1}$: together with the N-dependence of $\langle S \rangle$, this is another indication of long-ranged correlations, on the scale of the system size.

Such scaling behaviour hints at critical phenomena. The force threshold $v_0^*(N)$ for yielding decreases with N in our simulations, which is presumably also due to long-range correlations [34, 173]. Since we increase N at fixed v_0 while staying always below $v_0^*(N)$, some of the dependence on N may arise because the larger systems are closer to yielding. Indeed, larger systems support larger events, which tend to relax the system more quickly (compare Fig. 5.7(b) below).

While the ADD plastic events share similarities with those of AQS, there are also some important differences to emphasise. In particular, in ADD there is no preferred direction and the system is isotropic (apart from a possible influence of the periodic boundary conditions, which we expect to be very weak). In AQS, on the other hand, rotational symmetry is broken because the system is always sheared in the same direction. As a result, localised plastic events eventually organise into a line of slip, which leads to a subextensive scaling of event sizes $\langle S \rangle \sim L \sim \sqrt{N}$ in the steady state [58, 185]. These correlations also cause a reduction in the frequency of plastic events: the typical time (accumulated strain) between consecutive events scales as $\langle \tau' \rangle \sim 1/L \sim 1/\sqrt{N}$ (we recall it would be $\sim 1/N$ for independent events [58]).

In short, ADD in its elastic steps produces displacements that are correlated on the scale of the system size L, in agreement with predictions for finite τ_p [35]. However, the master curve for displacement correlations against r/L is different from the AQS case [149] because the local "affine" forces $\boldsymbol{\Xi}_i$ lack the correlations that are present for AQS [186]. For plastic events, the isotropy of ADD also leads to larger event sizes S and shorter inter-event times. The next question to be addressed is how the individual particles move in the active fluid, when observed over multiple time steps.

5.3 Microscopic dynamics

Since ADD is a computational tool to explore particle motion in dense active fluids, it is natural to study dynamical relaxation in ADD trajectories. To this end, we use observables developed for the analysis of relaxation in dense glassy systems [54]. Such measurements have also been used to describe particle motion in sheared and active glasses, which all display heterogeneous and cooperative dynamics.

5.3.1 Mean squared displacement

Fig. 5.4(a) shows the MSD (2.36) for different values of the self-propulsion velocity v_0. In the steady state, the MSD is nearly diffusive at all times. The self-diffusion constant at large times roughly decreases by an order of magnitude between $v_0 = 0.9$ and $v_0 = 0.8$. However, there is no feature in the average displacements that would allow identification of a characteristic relaxation time scale or length scale. This is in contrast to the classic two-step relaxation scenario found in many glassy systems [52, 132], but resembles the diffusive behaviour found in AQS simulations of sheared systems [187].

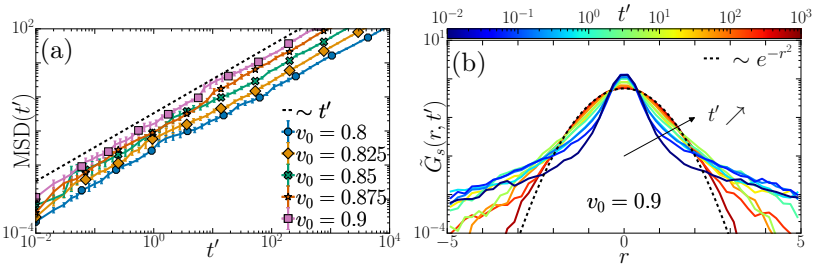

Figure 5.4: (a) Mean squared displacement (2.36) for different values of the self-propulsion velocity v_0. (b) Distribution of displacements (2.46) scaled by the MSD $\tilde{G}_s(r,t') = (1/N)\sum_{i=1}^{N}\langle\delta(r-\Delta r_{i,x}(t')/\mathrm{MSD}(t')) + \delta(r-\Delta r_{i,y}(t')/\mathrm{MSD}(t'))\rangle$ at different t'. Dashed line corresponds to a normal distribution. Parameter values: $N = 1024$, $v_0 = 0.9$, $\delta t' = 10^{-2}$.

Although the MSD displays seemingly trivial behaviour, the displacement distributions have significant structure. Fig. 5.4(b) shows the corresponding distribution $G_s(r)$ of the x and y-components of the particle displacements, scaled by the root mean-squared displacement, at $v_0 = 0.9$. These distributions differ strongly from Gaussian behaviour, which is only recovered in the large time limit, $t' \to \infty$. At small times $t' \ll 1$ (with of course $t' \geq \delta t'$), the displacement distribution has a narrow central peak with heavy tails. The width of these tails decreases with increasing time, and the distribution approaches a Gaussian form. For supercooled liquids, we would expect the small time distribution to be nearly Gaussian due to short-time thermal dynamics, with fat tails developing only as the system starts to relax. The tails appear when a significant number of particle rearrangements has taken place [146, 155]. The difference between ADD and thermal dynamics at short times is easily explained by the athermal quasistatic nature of ADD dynamics. Moreover, the participation in plastic events has a broad distribution [Fig. 5.3(c)]. As a result, the fat tails arising from structural relaxation are visible already after a single time step $\delta t'$ and arise from avalanches. In AQS simulations, similar heavy-tailed distributions also appear at early times due to plastic avalanches [187]. In both ADD and AQS we expect that nearly-exponential tails appear at intermediate times, as a generic result of the stochastic nature of avalanches [146].

To gain more insight into the dynamics, we decompose the displacements into separate contributions from elastic and plastic events. We define the elastic (resp. plastic) displacement of a particle between 0 and t' as the sum of its displacements over all elastic (resp. plastic) steps between these two times. We plot in Fig. 5.5(a) the MSDs from these contributions at $v_0 = 0.9$. Both of them show a crossover between two diffusive scaling regimes, *i.e.* both have $\mathrm{MSD}(t') \sim t'$ at short and at long times but with different prefactors. Despite the complex time dependences of the separate contributions, their sum in the total MSD appears nearly linear (recall Fig. 5.4).

To connect the elastic and plastic displacements to the distribution $G_s(r)$ in Fig. 5.4(b), we fit the central peak of $G_s(r)$ to a Gaussian distribution with standard deviation $\mathrm{std}(t')$ such that the associated mean-squared displacement is $\mathrm{MSD}(t') = 2\,\mathrm{std}^2(t')$. Fig. 5.5(a) compares this effective MSD to the elastic and plastic contributions. At small times, the central peak of G_s is compatible with the variance of elastic displacements, while at large times it is compatible with plastic displacements. Our interpretation is that for small times, displacements in elastic branches populate the narrow central part of the displacement distribution, while the displacements of rearranging particles populate the tails. At large times, plastic displacements dominate elastic

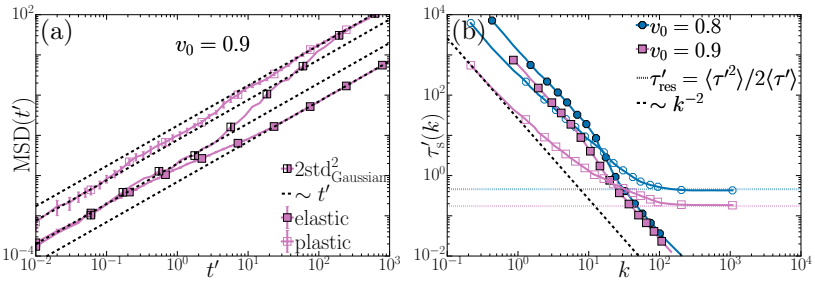

Figure 5.5: (a) Elastic and plastic contributions to the MSD, together with the MSD predicted from a Gaussian fit of the central part of G_s. (b) Wave-vector-dependent relaxation time $\tau'_s(k)$ (2.41) extracted from elastic and plastic displacements (colours and symbols as in (a)). Parameter values: $N = 1024$, $\delta t' = 10^{-2}$, (a) $v_0 = 0.9$.

displacements, and the whole displacement distribution is close to Gaussian, therefore its variance is dictated by plastic displacements.

5.3.2 Single-particle correlation functions

The MSD and the distribution G_s yield useful information about the dynamics. However, MSD measurements can sometimes be dominated by a subset of fast moving particles. To investigate this, we computed the self-intermediate scattering function $F_s(k, t')$ (2.40) and analyse the k-dependent relaxation time scale $\tau'_s(k)$ (2.41).

We plot $\tau'_s(k)$ for both elastic and plastic displacements in Fig. 5.5(b). Fickian diffusion would correspond to the scaling $\tau'_s(k) \sim k^{-2}$ [138]. Elastic displacements show two distinct diffusive scalings, at small and at large length scales (resp. small and large time scales). At small times, elastic displacements are computed over a single elastic trajectory segment, thus the corresponding diffusive behaviour derives from the balance between the Ornstein-Uhlenbeck driving on the one hand and the restoring forces on the other hand [150, 188]. At large times, elastic displacements are computed over many elastic trajectory segments separated by multiple plastic events. We expect the displacements over these different elastic trajectory segments to be independent, therefore the sum of all these displacements produces a diffusive behaviour distinct from that of single branch displacements. It is noteworthy that, in the hypothetical absence of plastic events, we do not expect the initial diffusive behaviour to extend to time scales larger than the Ornstein-Uhlenbeck driving correlation time τ_p.

The small and large length scale behaviour are also different for plastic displacements. These displacements are indeed diffusive at large length scales but they show a relaxation time scale $\tau'_s(k)$ that plateaus at small length scales. This plateau corresponds to the typical time for a plastic event to occur, and can be computed from the statistics of the inter-event times τ' as the residual time $\tau'_{\text{res}} = \langle \tau'^2 \rangle / (2\langle \tau' \rangle)$ [189]. Therefore, at times $t' \lesssim \tau'_{\text{res}}$ the plastic MSD is likely dominated by a small subset of particles.

It is noteworthy that this result is robust to changes in v_0 (see Fig. 5.5(b)). The residual time τ'_{res} changes by a factor of ~ 2.5 between $v_0 = 0.9$ and $v_0 = 0.8$, distinct from the factor of 10 observed for the self-diffusion constant. Moreover, since the diffusion constant drops more rapidly than the residual time increases, the typical length scale above which the plastic movement appears Fickian [138] decreases with decreasing v_0 – which is opposite to what we would expect for a supercooled liquid approaching the glass transition.

The displacement fields in the plastic events of Figs. 5.3(a, b) show that particles that are not involved in rearrangements can move away from their initial position without relaxing their local structure. But neither the MSD nor $F_s(k, t')$ can detect whether single particle translations actually correspond to changes in the local structure or not. To focus on this aspect of structural relaxation, we use the bond breaking correlation function $C_{\text{b}}(t')$ (2.45) where the parameter $A_1 = 1.25$ is the cutoff defining initial neighbours, and $A_2 = 1.5$ quantifies the distance they are required to separate before the correlation function decays This function obeys $C_b(t' = 0) = 1$, by definition, and it quantifies at time t' the average fraction of neighbours lost since $t' = 0$. This way, it efficiently disentangles rearrangements from displacements that do not relax the local structure.

Fig. 5.6 shows $C_{\text{b}}(t')$ for several values of v_0. The relaxation time scale τ'_b of C_{b} roughly increases by an order of magnitude between $v_0 = 0.9$ and $v_0 = 0.8$, mirroring the decrease of the self-diffusion constant. Moreover, $\tau'_b \gg 1$, so structural relaxation happens long after self-propulsion forces have fully decorrelated from their initial values which occurs for $t' \sim 1$. The correlation function is stretched, which suggests that structural relaxation is temporally heterogeneous [132]. In addition, it is remarkable that the MSD at the time τ'_b where local structure becomes fully decorrelated is greater than unity. This is again very different from thermal glasses where the escape from the cage also coincides with structural relaxation. Here instead particles travel comparatively larger distance without necessarily relaxing the structure, which can be seen as a consequence of the swirling motion observed in snapshots such as Fig. 5.2(a) (for elastic events) or Fig. 5.3(a,b) (for plastic ones).

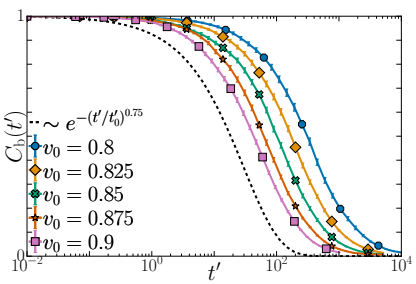

Figure 5.6: Bond breaking correlation function $C_{\text{b}}(t')$ (2.45) for different values of the self-propulsion velocity v_0. Parameter values: $N = 1024$, $\delta t' = 10^{-2}$.

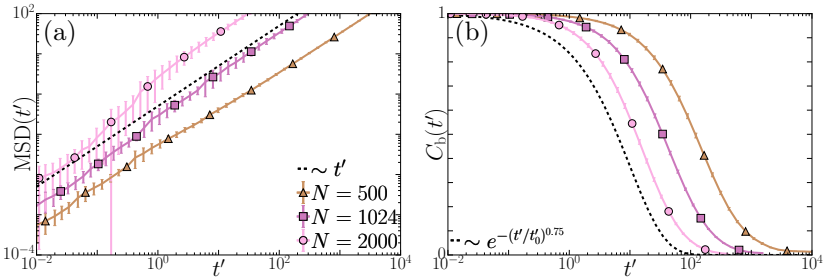

Figure 5.7: (a) Mean-squared displacement (2.36) and (b) bond-breaking correlation function $C_b(t')$ (2.45) for different N. Parameter values: $v_0 = 0.9$, $\delta t'(N = 500) = 2 \times 10^{-3}$, $\delta t'(N = 1024) = 1 \times 10^{-3}$, $\delta t'(N = 2000) = 5 \times 10^{-4}$.

We finally show the dependence of the dynamics on system size N. Fig. 5.7 shows the MSD and the bond breaking correlation function for a fixed $v_0 = 0.9$ but different values of N. For all values of N studied, the MSD is diffusive at large times and the relaxation of $C_{\rm b}(t')$ is stretched. Strikingly, however, both functions strongly depend on the system size with no sign of a saturation at some large N value. As N increases, the particles move faster, resulting in an MSD that is larger and a time correlation function that decreases faster. Since we have simulated three system sizes, it is not easy to determine a precise scaling of the self-diffusion constant and the relaxation time τ'_b with N. There are two sources for the system size dependence of the dynamics as discussed above: the frequency and size of the plastic events both increase with N, recall Fig. 5.3. Thus, in the ADD regime, the dynamics is always sensitive to the system size, as a result of the large persistence time limit. This is again in good analogy with the AQS dynamics where the self-diffusion constant also changes with system size [190].

5.3.3 Dynamical heterogeneity

In glassy fluids, one generally expects complex heterogeneous dynamics, where spatial fluctuations around the average dynamical behaviour are important for understanding the relaxation dynamics [54] (see Sec. 4.3). The system considered here also has this feature. It is illustrated in the snapshots of Figs. 5.8(a-d) which show maps of a single-particle analogue of the bond-breaking correlation function (2.45). This is defined as

$$C_{{\rm b},i}(t') = \frac{\sum_j \Theta(A_1 - \hat{r}_{ij}(0))\,\Theta(A_2 - \hat{r}_{ij}(t'))}{\sum_j \Theta(A_1 - \hat{r}_{ij}(0))}, \tag{5.24}$$

and represents the fraction of bonds of particle i that have been broken up to time t'. Just like its global analogue, this function decays from unity to zero as the environment of particle i decorrelates from its initial state.

The definition of a local relaxation function in (5.24) allows us to visualise in real space how the initial structure of the system relaxes as dynamics proceeds. The main observation in the snapshots of Fig. 5.8 is that the spatial distribution of relaxed particles, at any given time, reveals strong spatial correlations in the local dynamics.

While similar observations of spatially correlated dynamics are quite generic in dense amorphous materials, the time series shown in Fig. 5.8(a-d) reveals additional features beyond the mere existence of correlations. We

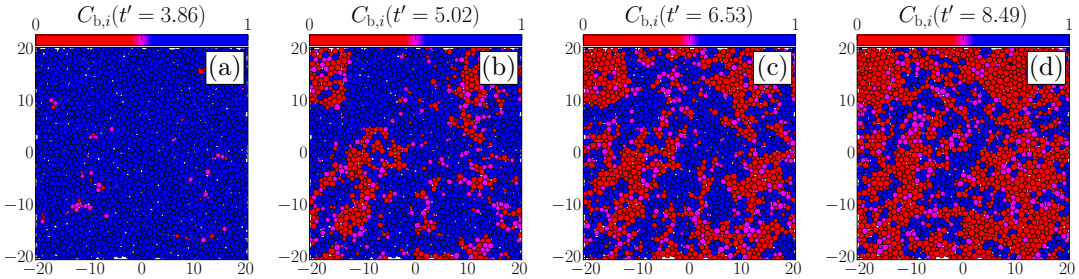

Figure 5.8: (a-d) Snapshots of the system highlighting the local bond breaking correlation $C_{{\rm b},i}$ (5.24) between time $t' = 0$ and a lag time of (a) $t' = 3.86$ (124 plastic events, $C_{\rm b} = 0.89$), (b) $t' = 5.02$ (196 plastic events, $C_{\rm b} = 0.65$), (c) $t' = 6.53$ (252 plastic events, $C_{\rm b} = 0.52$), (d) $t' = 8.49$ (355 plastic events, $C_{\rm b} = 0.41$). Parameter values: $N = 2000$, $v_0 = 0.9$, $\delta t' = 5 \times 10^{-4}$.

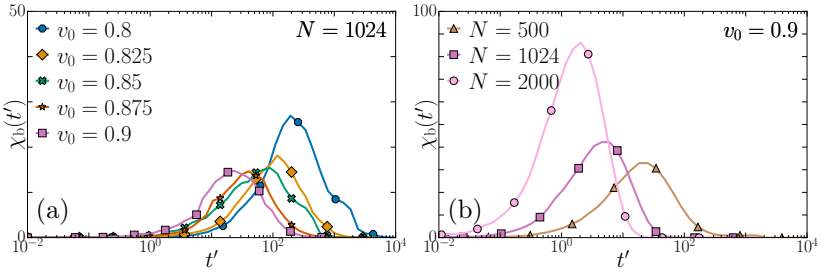

Figure 5.9: (a) Bond breaking dynamical susceptibility $\chi_b(t')$ (5.25) for different self-propulsion velocities v_0 with $N = 1024$ and $\delta t' = 10^{-2}$. (b) Bond breaking dynamical susceptibility $\chi_b(t')$ (5.25) for different N. Parameter values: (a) $N = 1024$, $\delta t' = 10^{-2}$, (b) $v_0 = 9$, $\delta t'(N = 500) = 2 \times 10^{-3}$, $\delta t'(N = 1024) = 1 \times 10^{-3}$, $\delta t'(N = 2000) = 5 \times 10^{-4}$.

observe that at short times (Fig. 5.8(a)), only a few particles have relaxed, and the spatial structure of the $C_{b,i}$ reveals the very few underlying plastic events that have taken place in this particular trajectory. At larger times (Figs. 5.8(b, c)), one sees that additional structural relaxation events tend to happen in the close vicinity of previous ones. These observations have also been made in slowly relaxing supercooled liquids at equilibrium and this effect is known as dynamical facilitation [143, 191]. At the microscopic level, these effects must correspond to spatio-temporal correlations between successive plastic events. Close to the relaxation time τ_α (Fig. 5.8(a-d)), we can clearly identify fast regions where particles have been involved in numerous rearrangements and have relaxed their local initial structure. We also see slow regions where particles' local environments remain the same. Finally, at long times all particles have $C_{b,i} \approx 0$ and one recovers a homogeneous picture. It is noteworthy that despite the absence of shear to organise plastic activity into anisotropic structures (namely, shear bands [58]), correlations spontaneously emerge between the plastic centres.

The extent of these dynamical spatial correlations can be quantified via the dynamical susceptibility (2.48)

$$\chi_{\rm b}(t') = N[\langle C_b(t')^2\rangle - \langle C_b(t')\rangle^2] \,. \tag{5.25}$$

where C_b is the bond-breaking correlation function (2.45). This function is plotted for different values of the self-propulsion velocity v_0 in Fig. 5.9(a), and for different numbers of particles N in Fig. 5.9(b). As usual, $\chi_{\rm b}$ shows a peak at the time close (but not exactly equal) to $\tau'_{\rm b}$ where C_b starts to decrease [142], indicating that the dynamics is most heterogeneous around these times. The slowdown of the dynamics with decreasing v_0 or N (Figs. 5.6, 5.7) is reflected in the corresponding increase of this peak time. Moreover, the height of the peak tells us about the typical number of particles involved in correlated clusters in Fig. 5.8 [54]. At fixed N, the dynamical slowdown is accompanied by an increased cooperativity of the relaxation, as is observed for liquids approaching the glass transition [170]. This situation is different when the self-propulsion velocity v_0 is kept fixed: the dynamics speeds up with increasing N but it also becomes more cooperative with a larger dynamical susceptibility. Recall that ADD is defined by taking the limit $\tau_p \to \infty$ at fixed N: as a consequence, the length scale that characterises velocity fluctuations is slaved to the system size, and diverges for large N. The global correlation function $C_{\rm b}$ and its fluctuations $\chi_{\rm b}$ both change systematically with N, revealing that the long-time relaxation dynamics is also sensitive to the system size, presumably because of a cooperativity length scale that diverges with N.

These observations provide further evidence that spatially heterogeneous dynamics is very generic in dense and disordered fluids. A major difference with equilibrium supercooled liquids is the system size dependence observed for the dynamical heterogeneity, indicating a diverging correlation length. This is attributed to the quasi-static nature of the dynamics, as also found in AQS simulations [187]. In addition, the slow growth of dynamical correlations with time (see Fig. 5.9) reveals the role of dynamic facilitation. Whereas facilitation has been described before in equilibrium dynamics [143, 191, 192], much less is understood about its consequences for sheared and active systems. Our findings suggest that facilitation could also be a very generic feature characterising the relaxation dynamics of dense and disordered fluids, and this clearly deserves further study in the context of driven amorphous materials.

5.4 Conclusion: relaxation in extremely persistent active matter

The efficient implementation of activity-driven dynamics (ADD) [168, 169] enables us to study the relaxation of dense systems of self-propelled particles in which the persistence time τ_p is large compared to the microscopic time $\tau_r \gtrsim \tau_0$ that the system needs to reach an arrested state for a given set of self-propulsion forces. On time

scales $t = t'\tau_p$ of the order of the persistence time, the dynamics then becomes intermittent (see Fig. 5.1). In the absence of rearrangements, the system reacts elastically to changes in the self-propulsion forces. The resulting movements are correlated on the length scale of the system (see Fig. 5.2). Consecutive elastic events may be interrupted by plastic events that trigger instantaneous rearrangements. The participation in these events has a broad distribution. Outside of the plastic core forming these avalanches, the remainder of the system moves collectively to accommodate the rearranging regions (see Fig. 5.3).

Relaxation of the whole structure happens through the accumulation of many of these plastic events. This relaxation dynamics is nearly diffusive at all times (Fig. 5.4) and spatially heterogeneous (Fig. 5.8), implying that plastic events are not independent and tend to concentrate where they have already happened, in a fashion reminiscent of dynamic facilitation.

We expect our results to be transferable from two dimensions to three dimensions, as are the salient features of the physics of glasses [141] and cooperative motion in dense active matter [124].

The limit of large persistence $\tau_p \to \infty$ is taken at fixed number of particles N and there is thus a dynamical length scale that scales with the system size. As a consequence, the average dynamics of the system and its fluctuations all depend on the system size (see Figs. 5.7, 5.9).

At fixed v_0 we would also expect quantitative changes as ρ is increased: avalanches should become rarer but the evolution of their distribution remains uncertain. Also interesting to study in the future will be the connection between plasticity in ADD and approaches to yielding in passive materials that argue in favour of a mechanism based on fluctuating energy barriers [193] rather than effective thermal activation over fixed barriers [194–199].

We established that the relaxation dynamics in ADD is nearly diffusive at all times. However, this overall diffusive behaviour is the sum of two different kinds of displacements: plastic motion, which is diffusive on time scales larger than the residual time τ_{res} (*i.e.* the typical time between two plastic event), and elastic motion which is diffusive on time scales smaller than τ_p and time scales larger than τ_{res} with two different diffusion coefficients. We found that τ_{res} increases with decreasing self-propulsion velocity v_0, but to the best of our computational abilities we only accessed the regime $\tau_{\text{res}} \lesssim \tau_p$ (see Fig. 5.5(b)). At fixed N, we may expect that the typical time between plastic events $\tau_{\text{res}} \gg \tau_p$ in the limit $v_0 \to 0$. This separation of time scales would imply that on times $\tau_p \ll t \ll \tau_{\text{res}}$ the memory of the initial propulsion forces is lost but no significant relaxation event (*i.e.* plastic event) took place. We thus expect that particles will remain close to their initial position for some time before diffusing away on time scales $t \gtrsim \tau_{\text{res}}$. We would then recover a two-step relaxation scenario, with β-relaxation corresponding to the diffusive elastic exploration of a potential energy minimum. We recall that, due to the limit $\tau_p \to \infty$ taken at finite N, elastic displacements are correlated on the length scale of the system. Therefore, the distance travelled by particles before losing memory of their orientations may itself depend on the system size. However, since these are large wave-length fluctuations (as are Mermin-Wagner fluctuations [141]), it is possible that for large N these large fluctuations lead to relaxation events [139], which comes in contradiction with the hypothesis $\tau_{\text{res}} \gg \tau_p$. Further explorations are needed to validate this scenario and the nature of the very slow dynamics emerging in this limit.

6 | Large-persistence mesoscopic flow

We introduced three fundamental time scales (see Sec. 2.5). First there is the persistence time τ_p which is the characteristic time scale of evolution of the propulsion forces. Then there is the interaction time τ_0 (1 in our units) which sets the time scale to relax two-particle interactions. Finally there is the emergent relaxation time scale τ_α (2.42), which is the typical time scale for displacements over a length scale of order 1 to happen.

We established that, in dense systems of AOUPs for which $\tau_p \gg \tau_0$, there exist a velocity correlation length $\xi_{\boldsymbol{v}}$ which increases with increasing persistence time τ_p, and a velocity correlation time $\tau_{\boldsymbol{v}} \sim \tau_p$ [35, 36, 78, 79, 88, 103, 158] (see Sec. 4.1). Schematically these quantities indicate that two particles within a $\xi_{\boldsymbol{v}}$-radius at initial time will have a similar movement for a time of order τ_p as a consequence of these correlations.

Close to dynamical arrest, $\tau_\alpha \gg \tau_p$ (see Sec. 3.2). This implies that the displacements of particles on length scales of order 1 typically happen after both the propulsions and the velocities have decorrelated. Thus these displacements and the initial velocities are uncorrelated. On the contrary, close to the phase-separated region of the phase diagram, $\tau_\alpha \lesssim \tau_p$ (see Sec. 3.2). This suggests that displacements of order 1 are correlated with the initial velocities. We recall that this velocity field has many vortices which scale with $\xi_{\boldsymbol{v}}$ (see Secs. 2.4, 4.1). Thus particles are able to move distances of order 1, *i.e.* perform a mesoscopic flow, coherently with their neighbours.

The emergence of mesoscopic coherent flow from microscopic interactions bears strong similarities with the family of active systems described as *turbulent* [10, 93, 94, 100]. In our specific case, these flows appear in the absence of explicit aligning interactions [34, 39]. In this Chapter, we will describe how these flows take place, from the initial velocity field to the eventual structural relaxation. We will first characterise the static velocity correlations in moderately dense systems of persistent AOUPs. We will then explore how these initial velocity correlations lead to actual movement, on the scale of the interparticle distance, using single- and multi-particle correlations. Finally, we will show how the properties of the initial velocity field influence the long-time mixing dynamics of the system.

Some of the results of this Chapter were published in Ref. [200].

Contents

6.1 Static velocity correlations

In this Section, we characterise the velocity field of dense persistent systems of AOUPs at a given time t. We will quantify velocity correlations by computing the velocity correlation length $\xi_{\boldsymbol{v}}$, and study the features of the velocity correlation function.

The velocity field of dense and persistent system (see Fig. 6.1(a)) is complex, with many *jets* (regions with aligned velocities) and *swirls* (or *vortices*, regions with velocities orthogonal to the radius to a single point). Moreover the velocity is greatly heterogeneous (note the colour bar in logarithmic scale). Jets, swirls, and heterogeneous velocities are generic features in dense systems of persistent self-propelled particles [35, 124]. We will show however that the specific scaling of our velocity correlations, as well as the dynamics of our systems, are novel features. We quantify the extension of these structures in the velocity field with the velocity correlation function $C_{\boldsymbol{vv}}(r)$ (2.57). We introduce the velocity correlation length $\xi_{\boldsymbol{v}}$ by thresholding the correlation function $C_{\boldsymbol{vv}}(\xi_{\boldsymbol{v}}) = 10^{-2}$. We plot the correlation lengths and the correlation functions for different values of the persistence time τ_p in Figs. 6.1(b, c) and rescale the distance with the correlation length. The correlation length varies gradually and shows no sign of saturation at large persistence, therefore it could in principle be tuned to any desired value by tweaking the properties of the propulsion force [35]. The good collapse of the curves in Fig. 6.1(c) indicates that $\xi_{\boldsymbol{v}}$ is a relevant quantity to describe the velocity field. We highlight that the

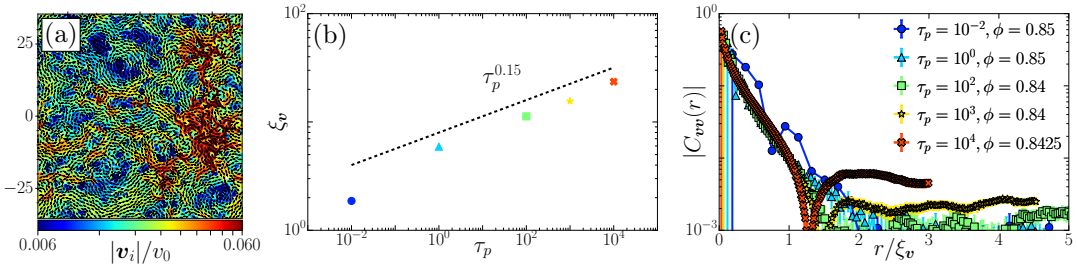

Figure 6.1: (a) Velocity snapshot. (b) Velocity correlation length $\xi_{\boldsymbol{v}}$ as a function of the persistence time τ_p. (c) Velocity correlations $C_{\boldsymbol{vv}}(r)$ (2.57) as functions of the distance, rescaled by the velocity correlation length $\xi_{\boldsymbol{v}}$, for different persistence times τ_p. Parameter values: $D_0 = 1$, (a) $N = 4096$, $\tau_p = 10^4$, $\phi = 0.8425$, (b, c) $N = 16384$.

growth of our correlation length $\xi_{\boldsymbol{v}}$ with the persistence time τ_p is slower than the expected $\sim \tau_p^{1/2}$ behaviour [35, 88, 103, 104], we will comment on this point below.

In order to discriminate velocity correlations between jets and swirls, it is useful to consider the velocities in the direction joining two particles (longitudinal correlations, $\alpha = ||$) or orthogonal to this direction (transverse correlations, $\alpha = \perp$)

$$C^{\alpha}_{\boldsymbol{vv}}(r) = \left\langle \frac{\sum_{i,j=1}^{N} v_i^{\alpha j} v_j^{\alpha i}\, \delta(r - r_{ij})}{\sum_{i,j=1}^{N} \delta(r - r_{ij})} \right\rangle \tag{6.1}$$

where $\hat{\boldsymbol{e}}_{ij} = (\boldsymbol{r}_j - \boldsymbol{r}_i)/r_{ij}$, and the longitudinal and transverse components of the velocities are $v_i^{||j} = \boldsymbol{v}_i \cdot \hat{\boldsymbol{e}}_{ij}$ and $v_i^{\perp j} = (\boldsymbol{v}_i \wedge \hat{\boldsymbol{e}}_{ij}) \cdot \hat{\boldsymbol{z}}$. These correlation functions are related by $C_{\boldsymbol{vv}}(r) = C^{||}_{\boldsymbol{vv}}(r) + C^{\perp}_{\boldsymbol{vv}}(r)$. It is noteworthy that there is no one-to-one correspondence between between the real-space decomposition of the velocity correlations and Fourier-space decomposition of velocity fluctuations (as computed *e.g.* in Refs. [39, 103]). These correlation functions are plotted in Fig. 6.2. Longitudinal correlations are the most extended, with significant correlations on the scale of the system size at our highest persistence time $\tau_p = 10^4$. Transverse velocity correlations quickly decay to negative values, and these negative correlations grow with increasing τ_p. This is consistent with the emergence of swirl patterns [14]. Both longitudinal and transverse correlations increase with the persistence time τ_p indicating that both jets and swirls tend to get larger as τ_p is increased.

As a matter of comparison to hydrodynamic descriptions of these systems, it is useful to introduce a velocity field

$$\boldsymbol{v}(\boldsymbol{r}) = \sum_{i=1}^{N} \boldsymbol{v}_i\, \delta(\boldsymbol{r} - \boldsymbol{r}_i). \tag{6.2}$$

We quantify the spatial correlations of the velocity field in Fourier space by introducing the kinetic energy spectrum [89, 100] (see App. B for properties)

$$E(k) = \frac{2\pi}{L^2} k \left\langle |\tilde{\boldsymbol{v}}(\boldsymbol{k})|^2 \right\rangle, \tag{6.3}$$

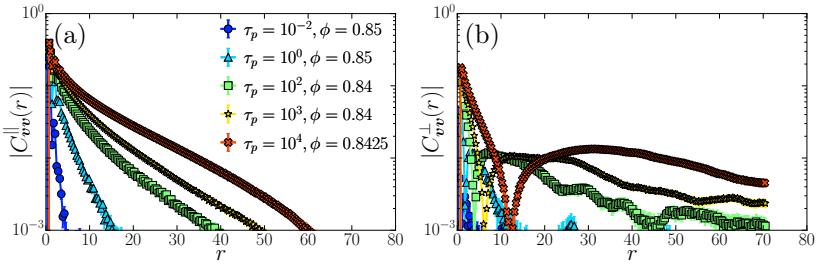

Figure 6.2: (a) Longitudinal and (b) transverse velocity correlations (6.1) for different persistence times τ_p. Parameter values: $N = 16384$, $D_0 = 1$.

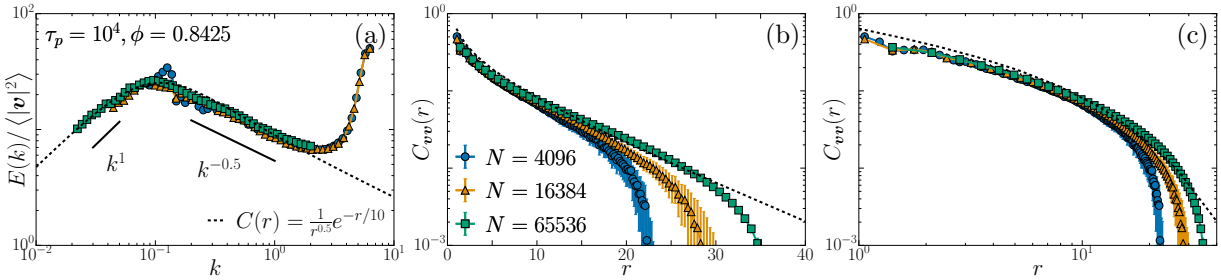

Figure 6.3: (a) Energy sprectum $E(k)$ (6.3) overlaid with prediction of energy spectrum from correlation function $C(r) \sim r^{-0.5}e^{-r/10}$ (B.21). (b, c) Velocity correlation function in real space $C_{\boldsymbol{vv}}(r)$ (2.57) plotted in (b) linear scale and (c) semilog, overlaid with $C(r)$. Parameter values: $D_0 = 1$, $\tau_p = 10^4$, $\phi = 0.8425$.

where $k = |\boldsymbol{k}|$ is the wave-vector norm, and we denote

$$\begin{aligned}\tilde{\boldsymbol{v}}(\boldsymbol{k}) &= \int \mathrm{d}^2\boldsymbol{r}\, e^{-\mathrm{i}\boldsymbol{k}\cdot\boldsymbol{r}}\boldsymbol{v}(\boldsymbol{r}) \\ &= \sum_{i=1}^{N} \boldsymbol{v}_i e^{-\mathrm{i}\boldsymbol{k}\cdot\boldsymbol{r}_i}\end{aligned} \tag{6.4}$$

the Fourier transform of the velocity field. For systems with inertia, the energy spectrum $E(k)$ provides information about the scales at which kinetic energy is accumulated [100]. This link is lost in overdamped systems, even though $E(k)$ is still related to the velocity correlation function via Fourier transform. The energy spectrum has the celebrated universal Kolmogorov scaling $E(k) \sim k^{-5/3}$ in inertial turbulence [89], while there is no universal scaling applicable to all models of active turbulence [94] (except for nematic turbulence [98]). We plot $E(k)$ in Fig. 6.3(a). There is a regime crossover around the wavevector norm $k^* = 2\pi/\xi_{\tilde{\boldsymbol{v}}}$. On large length scales $k \ll \xi_{\tilde{\boldsymbol{v}}}$, the energy spectrum $E(k) \sim k$, indicating that fluctuations of the velocities on lengths larger than $\xi_{\tilde{\boldsymbol{v}}}$ are scale-independent $\langle|\tilde{\boldsymbol{v}}(\boldsymbol{k})|^2\rangle \sim$ cst, and thus are uncorrelated. Therefore $\xi_{\tilde{\boldsymbol{v}}}$ has (alongside $\xi_{\boldsymbol{v}}$) the meaning of a correlation length. On smaller length scales, the energy spectrum scales as $E(k) \sim k^{-\alpha}$ with $\alpha \approx 0.5$, which behaviour is interrupted at very small length scales due to the microscopic structure of the liquid [103]. This scaling is different than what had been reported and predicted for dense and persistent systems of self-propelled particles, *i.e.* $\alpha = 1$ [35, 103, 104]. It is also different from previous works on active turbulence [94] which observe $\alpha \geq 1$. We note however the exponent is close to the one measured ($\alpha \approx 0.6$) for inertial ABPs at low density [39], even though we do not think these flows have the same origin.

We fit $E(k)$ with the spectrum derived from a correlation function $C_{\boldsymbol{vv}}(r) \sim r^{-(1-\alpha)}e^{-r/\xi_{\tilde{\boldsymbol{v}}}}$ (B.21), with $\alpha = 0.5$ and $\xi_{\tilde{\boldsymbol{v}}} = 10$. Were this the exact form of $E(k)$, it would indicate self-similar structure of the velocity field up to the length $\xi_{\tilde{\boldsymbol{v}}}$ [201]. We obtain good qualitative but not quantitative agreement with this fit. Simulations of larger systems with larger correlation lengths $\xi_{\tilde{\boldsymbol{v}}}$ (in comparison to the typical distance between particles) are needed to confirm the self-similar structure we hypothesise.

We highlight that the definitions of $\xi_{\tilde{\boldsymbol{v}}}$ and $\xi_{\boldsymbol{v}}$ are different: the former comes from fitting the spectrum $E(k)$, and the latter comes from thresholding the correlation $C_{\boldsymbol{vv}}(r)$. Thus, $\xi_{\tilde{\boldsymbol{v}}}$ informs us about the long-distance decay of velocity fluctuations, while $\xi_{\boldsymbol{v}}$ gives information about the strength of the correlations at a given distance. These do not have to be equal, *e.g.* adding translational noise to the system decreases the correlations in absolute value (and so decrease $\xi_{\boldsymbol{v}}$) but the correlations decay at large distance on the same scale $\xi_{\tilde{\boldsymbol{v}}}$ [202]. We observe quantitative discrepancy, by a factor of 2 to 3 for $\tau_p = 10^4$, however both lengths grow with increasing τ_p. We did not measure $\xi_{\tilde{\boldsymbol{v}}}$ systematically, therefore we do not know if its scaling with τ_p is identical to $\xi_{\boldsymbol{v}}$ or if it is closer to the expected $\sim \tau_p^{1/2}$ behaviour [35, 88, 103, 104]. We stress that we use relatively modest densities compared to *e.g.* Refs. [35, 103], thus a possible cause for the slower increase of the correlation length with τ_p may be that elastic moduli have a strong dependence on the persistence time.

Velocity correlations decay exponentially on distances of the scale of $\xi_{\tilde{\boldsymbol{v}}}$ [202]. At large distance, the correlation function is negative. This is a consequence of the constraint $\sum_{i=1}^{N} \boldsymbol{v}_i = 0$ in a finite-size system [203]. We plot in Fig. 6.3(b, c) the velocity correlation function in real space $C_{\boldsymbol{vv}}(r)$ (2.57) for system sizes ranging from $N = 4096$ to $N = 65536$. We recall that Fig. 6.3(a) indicated that features of the correlation function on scales smaller than the correlation length $\xi_{\tilde{\boldsymbol{v}}}$ did not depend on the system size. (It should be a necessity that $L > \xi_{\tilde{\boldsymbol{v}}}$ though.) In real space, we confirm that the correlation functions on scales lower and comparable to $\xi_{\tilde{\boldsymbol{v}}}$ are not affected by the system size. As N increases, the distance at which the correlation function becomes negative shifts steadily to larger distances. We expect that in the limit $N \to \infty$, the positive exponential decay of the correlation functions extend to $L \to \infty$.

6.2 Motion of a single particle and relative motion of neighbours

We showed that, due to velocity correlations at large persistence, first the picture of cage escapes constituting the elementary relaxation process is no longer valid, and then the movement of particles is collective on several time and length scales (see Secs. 4.3, 5.3.2). Therefore, as for the analysis of dynamical heterogeneity, the complete description of structural relaxation necessitates multi-particle correlations. In this Section, we combine both single- and two-particle descriptors in order to establish how static velocity correlations translate into motion.

We introduce the mean squared separation and the mean squared displacement difference

$$S^2(t) = \left\langle \frac{\sum_{i,j=1;i\neq j}^{N} r_{ij}(t)^2\,\theta_{ij}}{\sum_{i,j=1;i\neq j}^{N}\theta_{ij}} \right\rangle, \tag{6.5}$$

$$D^2(t) = \left\langle \frac{\sum_{i,j=1;i\neq j}^{N} |\Delta\boldsymbol{r}_j(t) - \Delta\boldsymbol{r}_i(t)|^2\,\theta_{ij}}{\sum_{i,j=1;i\neq j}^{N}\theta_{ij}} \right\rangle, \tag{6.6}$$

where we have defined the cut-off function $\theta_{ij} = \Theta(A_1 - |\boldsymbol{r}_j(0) - \boldsymbol{r}_i(0)|/\sigma_{ij})$, with $A_1 = 1.15$ defining the rescaled distance below which particles are considered initially neighbouring or bonded (see (2.45)). For two particles which were neighbours at $t = 0$, $S^2(t)$ varies with the distance between them at later times while $D^2(t)$ varies with the distance these particles have travelled away from each other. At large times, both are diffusive (2.39)

$$S^2(t), D^2(t) \underset{t\to\infty}{\sim} 2\mathrm{MSD}(t) \underset{t\to\infty}{\sim} 8Dt \tag{6.7}$$

which is also expected in inertial turbulence when particles eventually lose memory of their initial separation [204, 205]. On smaller times, in inertial turbulence and consistently with the scaling of the scale-dependent relative movement in Kolmogorov's theory [204], the separation is predicted to grow super-diffusively $S^2(t) \sim t^3$ [204, 206]. We compare these dynamical functions and the single-particle MSD (2.36) in Fig. 6.4. We observe 3 different regimes which we describe below.

- At small times, particles follow their initial velocities, the movement is ballistic, MSD $\sim t^2$. The squared relative displacement is also ballistic $D^2 \sim t^2$ and satisfies $D^2(t) < 2\mathrm{MSD}(t)$ which indicates that there are (positive) correlations between neighbours' velocities (the latter relation would be an equality otherwise).

- The MSD deviates from the ballistic scaling t^2 around a time τ_c. This indicates that part of the initial velocity correlation is lost around this time. We attribute this effect to "collision" with neighbours: the initial velocity of a given particle leads it towards an other particle, their interaction force grows until it significantly affects the velocity. In this regime, both the MSD and D^2 are superdiffusive. We note however that the former grows faster than the latter, indicating that the displacement of the particle in the centre-of-mass frame grows faster than its displacement in its neighbour's frame. Moreover, we note that S^2 remains of order 1 up to $t \sim \tau_p$, meaning that initial neighbours are most likely still neighbours. We conclude from these observations that this regime constitutes an "advection" regime: particles travel long distances (of order 1 at least) *with* their initial neighbours. We call these coherently moving ensembles of particles *correlation patches*.

- At τ_p the propulsion dynamics $\boldsymbol{p}_i$ decorrelates, and thus the 1-particle dynamics becomes diffusive as memory of the initial velocity is lost. We recall that at large times both S^2 and D^2 have to be equal to twice the MSD (6.7). At τ_p, both quantities are below 2MSD, they then go through a superdiffusive

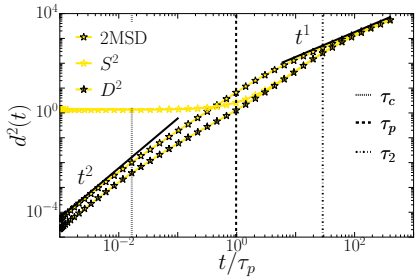

Figure 6.4: Mean squared displacement (2.36), mean squared separation S^2 (6.5), and mean squared displacement difference (6.6). Parameter values: $N = 1024$, $D_0 = 1$, $\tau_p = 10^3$, $\phi = 0.84$.

regime up to time τ_2. This superdiffusion of two-particle quantities is reminiscent of the superdiffusion of pair dispersion in inertial turbulence [204, 206]. This is the end of the advective regime, S^2 departs from 1, indicating that initially neighbouring particles start to separate. For times $t > \tau_2$, there is no information left about the initial state of the system. We highlight that this time is of the same order of the decay time of the bond breaking correlation (2.45), confirming that all initial bonds have been lost.

A natural question which arises is to know if the intermediate superdiffusive behaviour of the MSD corresponds to an actual power-law regime t^β with $1 < \beta < 2$, or if it is a smooth crossover between the ballistic and diffusive regimes. In the former case, this could indicate *e.g.* Lévy-flight-like behaviour [49]. We can analyse the MSD through the velocity autocorrelation function $C_{\boldsymbol{v}}(t)$ (2.58) (of which it is a double integral), and through its instantaneous log-slope

$$\beta(t) = \frac{\partial}{\partial \log t} \log \mathrm{MSD}(t) = \frac{2t}{\mathrm{MSD}(t)} \left\langle \boldsymbol{v}_i(t) \cdot \Delta \boldsymbol{r}_i(t) \right\rangle , \tag{6.8}$$

which satisfies $\beta(t \to 0) = 2$ (ballistic regime) and $\beta(t \to \infty) = 1$ (diffusive regime). We may expect that $\beta(t)$ plateaus for $\tau_c < t < \tau_p$ in the hypothesis that this intermediate regime is a true power-law regime. We plot in Fig. 6.5(a, b) the velocity autocorrelation function and the MSD. The former decays in a two-step fashion, on time scales which coincide with τ_c and τ_p. We propose as an ansatz that this decay correspond to the sum of two exponentials, one for each time scale, and we fit the correlation function to the following form

$$C_{\boldsymbol{v}}^{\mathrm{fit}}(t) = \nu e^{-t/\tau_c} + (1-\nu) e^{-t/\tau_p}, \tag{6.9}$$

where there are two fitting parameters: the collision time τ_c and the relative importance of the two exponentials $0 < \nu < 1$. A hypothetical setting where this kind of correlation emerges is if the velocity of the particle were the sum of two independent stochastic processes. For example, the first process could be the ensemble velocity of the particle's correlation patch, and the second its velocity in the frame moving with the patch. The first process would decorrelate over time scale τ_p and the second τ_c. We use the fit (6.9) to compute the associated MSD and log-slope of the MSD, which we additionally plot in Fig. 6.5. We observe that $\beta(t)$ oscillates (see Fig. 6.5(c)), which is qualitatively consistent with the velocity autocorrelation function being the sum of two exponential functions, but not quantitatively. To confirm this behaviour, we would need to simulate systems with a larger time scale separation between τ_c and τ_p.

Initially neighbouring particles start to separate around time τ_p, however we do not expect the pace of this separation to be homogeneous in time as we explain below. Particles move together, over large distances, in patches of length $\xi_{\boldsymbol{v}}$ where their velocities are correlated. Moreover, particles belonging to the same patch will separate slower than particles belonging to different patches. Consider the ensemble of bonded particles at some initial time, and the time needed for all these particles to eventually fall in separate patches, *i.e.* to reach a separation of order $\xi_{\boldsymbol{v}}$. If the initial correlation patches are large then there are few bonded particles belonging to different patches and the time to break all bonds will be large. On the contrary, if these initial patches are small then the time to break bonds will be smaller. Therefore, the heterogeneity of the correlation patches should translate into an heterogeneity of the dynamics leading particles to fall in separate patches. To capture

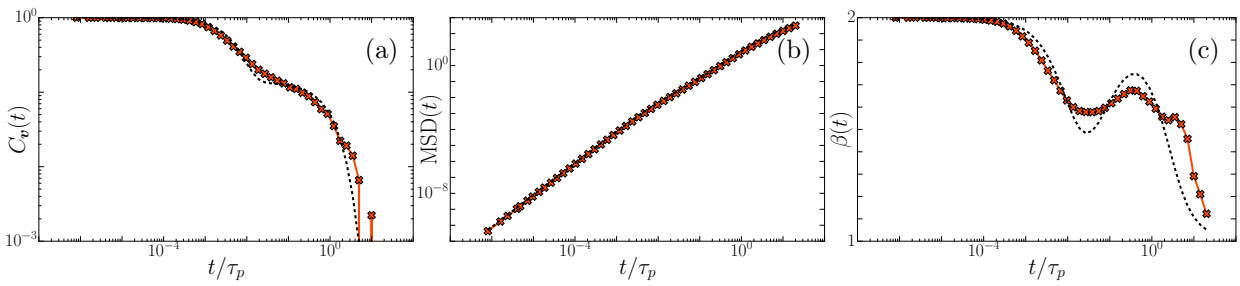

Figure 6.5: (a) Velocity autocorrelation function $C_{\boldsymbol{v}}(t)$ (2.58), (b) mean-squared displacement (2.36) , and (c) log-slope of the MSD $\beta(t)$ (6.8). We fit $C_{\boldsymbol{v}}(t)$ to (6.9) and plot in dashed line the associated quantities. Parameter values: $N = 4096$, $D_0 = 1$, $\tau_p = 10^4$, $\phi = 0.8425$.

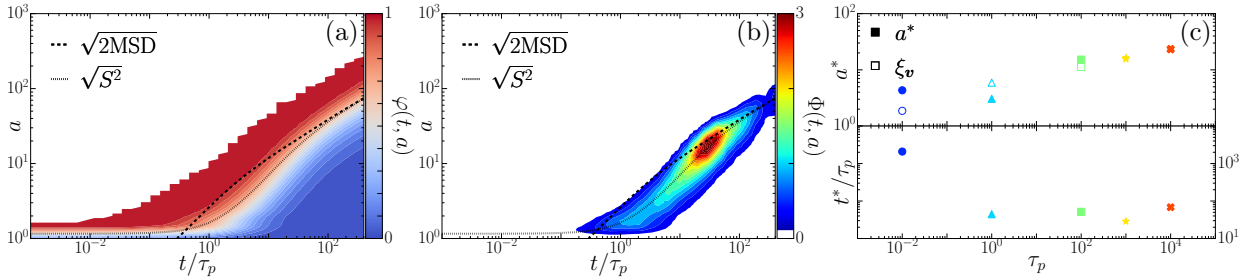

Figure 6.6: (a) Mean separation overlap $\varphi(t,a)$ (6.10c). (b) Variance of the mean separation overlap $\Phi(t,a)$ (6.10d). (c) Length scale a^* and time scale t^* of maximum $\chi_{S^2}(t,a)$ for systems at different persistence time τ_p. Parameter values: $N = 1024$, $D_0 = 1$, (a, b) $\tau_p = 10^3$, $\phi = 0.84$, (c) colours and markers correspond to the same τ_p and ϕ as Fig. 6.1(c).

this, we introduce the variance Φ of the mean separation overlap

$$\varphi_{ij}(t,a) = \Theta(a - r_{ij}(t)) \tag{6.10a}$$

$$\overline{\varphi}(t,a) = \frac{\sum_{i,j=1;i\neq j}^{N} \varphi_{ij}(t,a)\,\theta_{ij}}{\sum_{i,j=1;i\neq j}^{N} \theta_{ij}} \tag{6.10b}$$

$$\varphi(t,a) = \langle \overline{\varphi}(t,a) \rangle \tag{6.10c}$$

$$\Phi(t,a) = N\mathrm{Var}\left(\overline{\varphi}(t,a)\right) \tag{6.10d}$$

where $\mathrm{Var}(\ldots) = \langle (\ldots)^2 \rangle - \langle \ldots \rangle^2$ denotes a variance, and we will focus on the time scale t^* and the length scale a^* where it is maximum $\Phi(t^*,a^*) = \max_{t,a} \Phi(t,a)$. It bears similarity with the previously defined time- and length-scale dependent dynamical susceptibility χ_4 (4.3), with the important difference that Φ is the variance of an average of two-particle quantities, therefore $\Phi(t^*,a^*)$ cannot be read as a typical number of particles involved in correlated motion (contrarily to $\chi_4(t^*,a^*)$). We will see however that the coordinates (t^*,a^*) are relevant for the dynamics, as shown below. We show first how we can infer the time $t(a)$ of maximum Φ at fixed length a, and then discuss the information revealed by the length a^* at which Φ is globally maximal.

Consider a length scale $a \gtrsim 1$, and a pair i, j of bonded particles (*i.e.* $\theta_{ij} = 1$). We expect $r_{ij}(t \to 0) \sim 1$ (particles are initially bonded) and $r_{ij}(t \to \infty) \gg a$ (particles diffuse away from each other). Therefore $\varphi_{ij}(t,a)$ is, for all pairs and all initial times, equal to 1 (resp. 0) for very small (resp. large) t. As a consequence, the variance Φ cancels for both limits $\Phi(t \to 0, a), \Phi(t \to \infty, a) \approx 0$. We showed, for the dynamical susceptibility χ_4 (4.3), that it was maximum for a time scale $t(a)$ where displacements are typically of the order of a, as seen by $\sqrt{\mathrm{MSD}(t(a))} \approx a$ (see Fig. 4.6). Analogously, we expect that the variance Φ will be maximum for a time scale $t(a)$ at which separations $r_{ij}(t(a))$ are typically of the order of a. This is confirmed by Fig. 6.6(b) where, at fixed a, $\Phi(t,a)$ peaks at a time $t(a)$ for which $\sqrt{S^2(t(a))} \approx a$.

For a given length scale a, $\Phi(t(a),a)$ characterises the width of the distribution of $\overline{\varphi}(t(a),a)$ (6.10b) when considering different starting configurations. We hypothesized that the heterogeneity of the velocity field translates into the heterogeneity of the time needed to make all initially bonded particles fall into separate patches. We thus expect that $\Phi(t(a),a)$ will be maximum for the scale $\xi_{\boldsymbol{v}}$ corresponding to the typical patch size. This is confirmed in Fig. 6.6(c) which shows that a^* is comparable to $\xi_{\boldsymbol{v}}$. We conclude that $t(a^*)$ is the typical time at which initially neighbouring particles eventually end up in different correlation patches. We thus use $\tau_2 = t(a^*)$ as a definition for the time at which D^2 and S^2 eventually diffuse. While the velocity correlation length $\xi_{\boldsymbol{v}}$ consistently increases with increasing τ_p, we note that the ratio τ_2/τ_p remains almost constant at large τ_p (see Fig. 6.6(c)) which suggests that it is τ_p which controls the dynamics.

6.3 A new class of active turbulence

Within the existing symmetry classification of active-turbulent systems [94], the natural comparison with our system is polar turbulence with dry friction, *e.g.* Ref. [31]. These models do not distinguish between the polarisation (self-propulsion vector) and the velocity which are considered aligned. This is not the case in our model where, on the contrary, velocities and propulsions can be different and generally are. The velocity correlations at the origin of the chaotic advection are an emerging phenomenon, in the presence of steric interactions, and do not derive from spatial correlations of the self-propulsion forces.

However, these extended correlations come at the (computational) expense of a very large persistence time $\tau_p \gg \tau_0$ and finely tuned packing fraction ϕ to avoid MIPS or dynamical arrest (see Fig. 3.6). This limitation

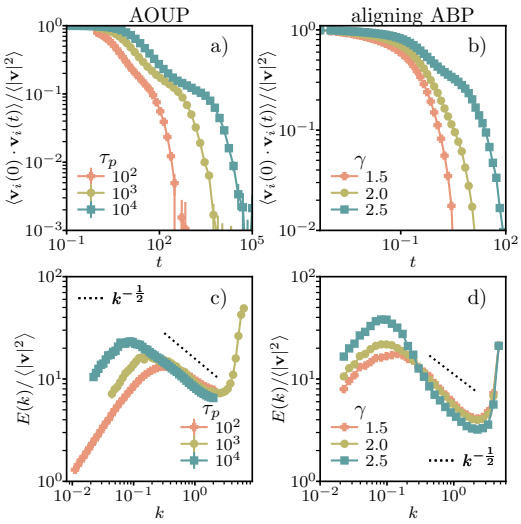

Figure 6.7: Comparison of (top) velocity autocorrelation functions $C_{\boldsymbol{v}}(t)$ (2.58) and (bottom) kinetic energy spectra $E(k)$ (6.3), between (left) AOUPs at different persistence times τ_p, and (right) ABPs with alignment at different alignment strength γ. Taken from Ref. [200], Fig. 2.

motivates the use of a second model of self-propelled particles, this time with weak alignment. We introduce a model of ABPs (2.5) with the same interaction potential U and we add an alignment term to (2.5b)

$$\dot{\theta}_i = \sqrt{2/\tau_p}\,\eta_i + \frac{\gamma}{n_i}\sum_{j=1;i\neq j}^{N} \sin(\theta_j - \theta_i)\,\Theta(2 - |\boldsymbol{r}_j - \boldsymbol{r}_i|), \tag{6.11}$$

where $n_i = \sum_{j=1;i\neq j}^{N}\Theta(2-|\boldsymbol{r}_j-\boldsymbol{r}_i|)$ is the number of neighbours interacting with i, and γ sets the alignment strength. We will refer to this model as aABP. We mean by weak alignment that γ is small enough so that the system does not display long-range propulsion correlations (*i.e.* the system is not in a polar ordered state). Simulations for this model were performed by Juliane Klamser [200].

The aligning interactions generate long persistence times, even if isolated particles decorrelate quickly ($\tau_p = 1$ for these aABPs). This model is not exempt of spatial propulsion correlations, however these are short-ranged, and over a length scale which is significantly smaller than the velocity correlation length $\xi_{\boldsymbol{v}}$. This confirms the emerging nature we described for these velocity correlations, at odd with the mechanism of correlated propulsions described by existing continuum theories [31]. We plot in Fig. 6.7 the velocity autocorrelation functions and the energy spectra for both models. First these show that, in both models, there is a two-step decay of velocity autocorrelations, first at the collision time τ_c and then at the persistence time, which is an emerging quantity in the aABP model. Then these also show that we can tune the velocity correlation length by varying model parameters, the persistence time τ_p for AOUPs and the alignment strength γ for aABPs.

We provide a qualitative picture of the dynamics by "dyeing" particles according to their position at some initial time $t_0 = 0$ in the steady state, and watching them spread over time, see Fig. 6.8. At small times $t \lesssim \tau_p$ the rainbow pattern is deformed over the length scale of the correlation length, consistently with the picture of correlation patches moving with respect to each other. At larger times $t \gtrsim \tau_p$ these patches decorrelate from their initial shapes and different groups move together. The resulting distortion of the pattern, with mutually

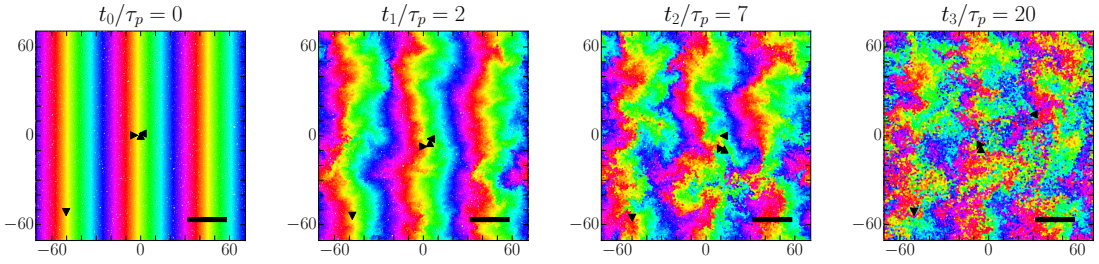

Figure 6.8: Time-series of a turbulent-like system. Colours are fixed at initial time. Black solid line has length $\xi_{\boldsymbol{v}}$. Parameter values: $N = 16384$, $D_0 = 1$, $\tau_p = 10^4$, $\phi = 0.8425$

invading branches that stretch and fold over a range of length scales, resembles advective mixing (see times t_1, t_2). Only at large times particles diffuse into regions of different colours which eventually blends the dyes (see time t_3). We highlight with three tracer particles (▲, ►, ◄), all initially close, that particle pairs can be either advected large distances together over these large times or be separated almost immediately. An additional tracer particle (▼) shows a particle whose displacement remains small along this time lapse, confirming the important heterogeneity of the movement. These time-dependent patterns are qualitatively similar to the ones observed in the aABP model [200] (see Figs. 4(a, d)) and to the chaotic advection created in time periodic flows [207]. Finally, we stress that the emerging mesoscale chaotic flows happens over large but finite length and time scales which are both controlled by the persistence time τ_p.

Therefore we observe in two different models of dense active matter the emergence of persistence-induced mesoscopic flow, with identical scalings of the velocity correlations. These observations hint at a possible universal nature of these correlations and of the dynamical behaviour we described. We thus argue for a new class of active turbulence, not captured by the classification of Ref. [94], where crowding and persistent motion play a central role in creating chaotic collective motion. This new class should encompass diverse models where crowding is important, such as vibrated disks [208], self-aligning self-propelled particles [5, 209], or self-propelled Voronoi models of confluent tissues [210].

6.4 Conclusion: persistence-induced mesoscopic flow

We reported that the mesoscale chaotic flows characteristic to active turbulence are observable in one of the simplest active matter model: overdamped athermal self-propelled particles in the absence of aligning interactions. Mesoscale velocity correlations emerge from the competition between persistent forcing and crowding. The associated velocity pattern displays jets and swirls, reminiscent of multiscale flow patterns in inertial turbulence, with a characteristic length scale $\xi_{\boldsymbol{v}}$ which is controlled by the persistence time τ_p. At moderate density, particles are able to move along these velocity correlations over a time scale comparable to τ_p, resulting in a complex collective flow in which particles are collectively advected along the velocity field (see Fig. 6.8). At large times $t \gg \tau_p$ the memory of the initial velocity field is lost and the movement is diffusive.

The correlations we report are distinct from what had been previously reported in the literature for dense persistent active matter [35, 88, 103, 104]. Part of this discrepancy may be attributed to the failure of the hypothesis of a persistent perturbation around a minimum of the interaction potential U [35, 88]. Indeed our analysis shows that the structure evolves on time scales smaller than the persistence time τ_p. However, as we were not able to check our model against the approximations of hydrodynamic theories [103, 104], it remains unknown if an extension of the latter could include our results. Furthermore, these correlations are distinct from the correlations observed in other models of active turbulence [31, 94]. This may indicate that our model belongs to a distinct class of turbulent models, in which crowding plays a central role.

7 | Dense and persistent monodisperse systems

We expect dense monodisperse systems of self-propelled particles to display order, either orientational or translational, at large packing fraction ϕ [46, 47, 49]. Previous studies have shown that this would impact in a non-trivial way the relaxation dynamics of the system [49–51]. In this Chapter, we apply the methodology we have developed to understand the relaxation of persistent polydisperse particles to characterise how these mechanisms are affected by the emergence of order.

Some of the results of this Chapter were extracted from previous unpublished work by Daniel Vågberg [211], and some others are related to ongoing experimental work in collaboration with the groups of Olivier Dauchot and Denis Bartolo.

Contents

7.1 Phase diagram of monodisperse AOUPs

We first map the phase behaviour of monodisperse AOUPs as a function of the persistence time τ_p and the packing fraction ϕ, and at constant free-particle self-diffusion constant D_0, similarly to mapping in the polydisperse case (see Chap. 3). At a given persistence time, as introduced in Sec. 2.3.1.2, we compute the packing fraction $\phi_6(\tau_p)$ at which the hexatic order correlation function $C_{\psi_6\psi_6}(r)$ (2.30) goes from an exponential to an algebraic decay indicating quasi-long-range orientational order, and the packing fraction $\phi_g(\tau_p)$ at which the translational order correlation function $|1 - g(r)|$ (2.32) goes from an exponential to an algebraic decay indicating quasi-long-range translational order. Similarly to Sec. 3.1, the boundary of the MIPS region are determined via the inspection of the distribution of the local packing fraction ϕ_{loc} (2.26).

We plot in Fig. 7.1 the phase diagram of monodisperse AOUPs interacting via a WCA potential at constant $D_0 = 0.1$. As previously reported for polydisperse AOUPs (see Fig. 3.6), MIPS emerges when the persistence length ℓ_p is large compared to the typical interparticle distance [1, 46, 109, 125, 127, 129]. At large ϕ, the system first transitions to an hexatic solid, and then to an ordered solid [46, 47, 49], and thus $\phi_g(\tau_p) > \phi_6(\tau_p)$ for all τ_p. Moreover, both transition packing fractions shift to significant larger values as τ_p is increased, which may explain why Ref. [51] does not observe an hexatic phase at lower densities. It is also noteworthy that for $\ell_p \gtrsim 1$ (*i.e.* $\tau_p \gtrsim 10$) the transition to the solid regime (with quasi-long-range translational order) was not

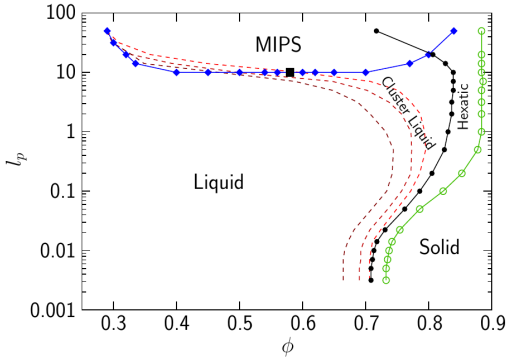

Figure 7.1: Phase diagram for monodisperse AOUPs at constant free-particle self-diffusion constant $D_0 = 0.1$, in the space spanned by the persistence length $\ell_p = \sqrt{D_0\tau_p}$ (2.12) on the y-axis and the packing fraction ϕ on the x-axis. Dashed lines are isolines of $\phi_6^{\mathrm{loc}} = (1/N)\sum_{i=1}^{N}\langle|\psi_{6,i}|\rangle$. Taken from Ref. [211].

observed due to the difficulty of simulating the steady state of the system at these large densities. In addition to these phases, there is a crossover *cluster liquid* region, in between MIPS and the hexatic phase, in which large dense hexatic clusters are formed while global order remains low. These clusters are unstable, they coalesce and separate quickly, so that the system remains fluid. These observations are consistent with the experimental work of Ref. [51]. Finally, in the domains of large persistence corresponding to the emergence of MIPS, increasing τ_p stabilises the hexatic phase, as seen by the late decrease of $\phi_6(\tau_p)$ with increasing τ_p for $\ell_p \gtrsim 10$. In this limit, the hexatic domain transition line crosses MIPS, indicating that the dense MIPS cluster is an hexatic phase, consistently with the result of Ref. [46].

In the cluster liquid region, both conditions of crowding and persistent propulsions are met, and thus velocity correlations should be important. Analogously to our investigation of the influence of these correlations to the approach to dynamical arrest in polydisperse systems (see Chap. 4), we may investigate their influence on the dynamics of monodisperse systems close to the hexatic and solid transitions.

7.2 Static correlations

To avoid phase separation, we focus on persistent systems ($D_0 = 0.1$, $\tau_p = 250$) with a moderate persistence length ($\ell_p = 5$). However, at small packing fraction ($\phi \approx 0.70$, Fig. 7.2(a, b)), we observe large density fluctuations due to the proximity of the MIPS critical point.

Fig. 7.2(a, c, e, g) shows the argument of the hexatic order parameter $\arg(\psi_6)$ (2.28) for each particle in systems with increasing packing fraction ϕ. The hexatic order correlation length ξ_{ψ_6}, which characterises the width of single-colour patches (which we will call *hexatic patches*), grows with increasing ϕ, until it spans the whole system at $\phi = 0.87$. At this density, spatial correlations of ψ_6 reach a non-zero plateau (see Fig. 7.3(b)) indicating that orientational order is long-range as in a solid phase. This phase still contains small defective regions in the form of vacancies (*i.e.* one to a few lattice sites missing within the perfect crystal arrangement), as well as large defective regions where the orientation of the hexatic order mismatches and where the order itself (both orientational and translational) is low. The distance between these defects is the distance over which the order of the structure is correlated, it should thus correspond to the translational order correlation length ξ_g. The existence of such a length is incompatible with a two-dimensional solid phase in which translational order correlations are scale-free. As the packing fraction ϕ is increased, we observe that defects are concentrated in the boundaries between regions of distinct hexatic orientation. Moreover these regions are exempt of free dislocations and the dynamics within them is mostly arrested or concentrated in fault lines. Therefore these regions may be considered as small *crystallites* surrounded by liquid defective regions.

Fig. 7.2(b, d, f, h) shows the velocity field with increasing ϕ. This field is correlated over a length scale $\xi_{\boldsymbol{v}}$, and this length increases with ϕ (see Fig. 7.3(c)). Qualitatively, we observe at moderately large densities ($\phi \lesssim 0.82$) that regions of coherent velocities (linearly correlated or forming swirls) are contained within hexatic patches. In the hexatic phase ($\phi = 0.87$), ξ_{ψ_6} is of the order of the system size L while $\xi_{\boldsymbol{v}}$ is smaller. We note that the velocity correlation length $\xi_{\boldsymbol{v}}$ is itself finite in a perfect crystal [88], we may thus expect that it remains finite (and lower) in less ordered solids. Therefore, there should be a hypothetical, density-dependent, maximum length scale for the velocity correlations, which the hexatic length ξ_{ψ_6} eventually exceeds at large ϕ. The translational order correlation length ξ_g is also expected to increase with ϕ. Where this length is finite (*i.e.* smaller than the system size) and characterises the distance between defects, it might be an upper limit to $\xi_{\boldsymbol{v}}$ if defects kill the persistence-induced velocity alignment mechanism. It is necessary to disentangle the role of these different length scales: in the disordered liquid, are distinct hexatic patches formed by unaligned velocities or are these patches the support for velocity correlations whose length they cannot exceed? in the hexatic phase, do velocity correlations create defects or are these defects obstacles to the extension of velocity correlation?

In order to bring answers to these questions, we manually fit the correlation functions $C_{\boldsymbol{vv}}(r)$ (2.57), $C_{\psi_6\psi_6}(r)$ (2.30), and $|1 - g(r)|$ (2.32), to exponential functions with scales $\xi_{\boldsymbol{v}}$, ξ_{ψ_6}, and ξ_g respectively. We report these lengths in Fig. 7.3(d). We observe up to $\phi \approx 0.82$ that the velocity correlation length $\xi_{\boldsymbol{v}}$ and the translational order correlation length ξ_g are identical and increase with packing fraction ϕ. On this same range of ϕ we observe that the hexatic correlation length ξ_{ψ_6} is significantly greater than the other two lengths. We may infer that in this regime the velocity correlations are cut by defects and thus do not scale larger than the translational order. At larger ϕ, in the regime where ξ_{ψ_6} is of the order of the system size, we observe that ξ_g increases significantly faster than $\xi_{\boldsymbol{v}}$, and these thus decouple. This is consistent with the expectation that ξ_g reaches the system size at large packing fraction ϕ (see Fig. 7.1). In this regime we thus have that orientational and translational order is conserved on the length scale of $\xi_{\boldsymbol{v}}$. At equivalent structure we should thus expect that $\xi_{\boldsymbol{v}}$ would increase with the persistence time τ_p.

Qualitatively, the dynamics of the system in the liquid phase shows that the lifespan of the cluster is larger

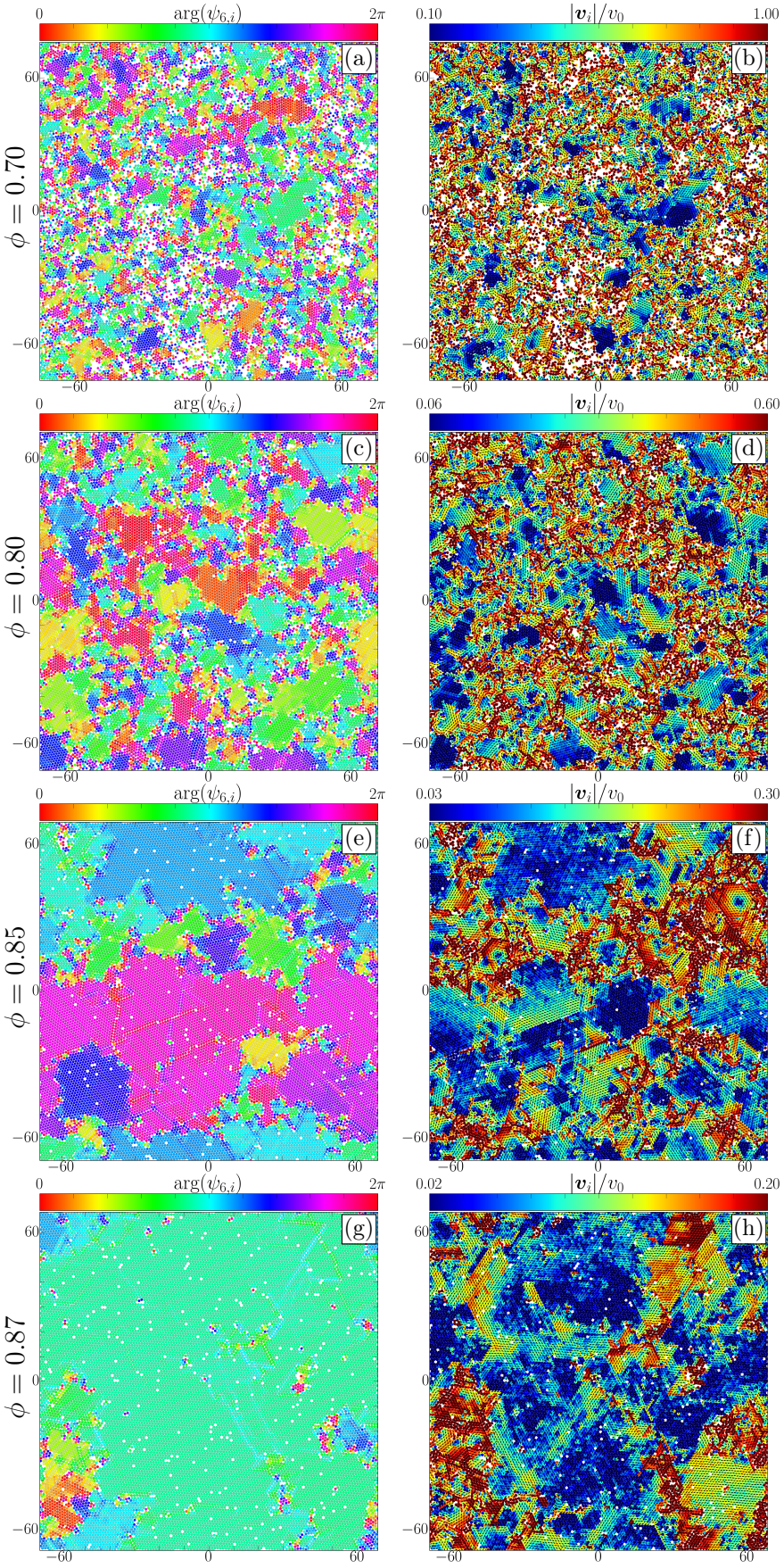

Figure 7.2: (a, c, e, g) Snapshots with colours corresponding to the argument of the hexatic order parameter $\arg(\psi_6)$ (2.28). (b, d, f, h) Velocity snapshots. Parameter values: $N = 16384$, $D_0 = 0.1, \tau_p = 250$.

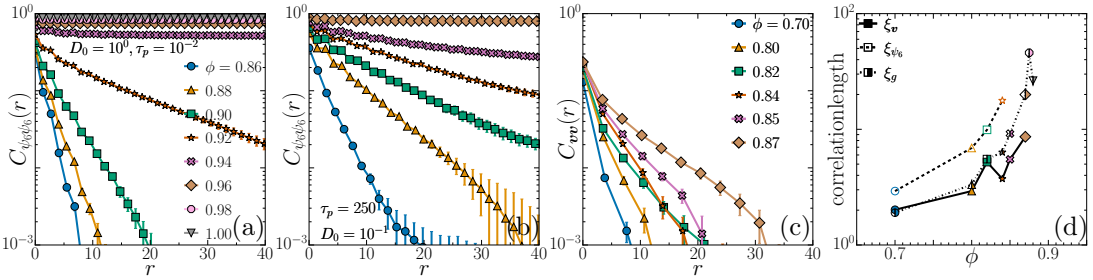

Figure 7.3: (a, b) Hexatic order parameter correlation function $C_{\psi_6\psi_6}(r)$ (2.30) for different packing fractions ϕ. (c) Velocity correlation function $C_{\boldsymbol{vv}}(r)$ (2.57) for different packing fractions ϕ. (d) Velocity correlation length $\xi_{\boldsymbol{v}}$, hexatic order correlation length ξ_{ψ_6}, and translational order correlation length ξ_g, as functions of the packing fraction ϕ. These are extracted from manual exponential fits of $C_{\boldsymbol{vv}}(r)$, $C_{\psi_6\psi_6}(r)$, and $|1 - g(r)|$ respectively. Parameter values: $N = 16384$, (a) $D_0 = 1$, $\tau_p = 10^{-2}$, (b-d) $D_0 = 0.1$, $\tau_p = 250$.

than the lifespan of velocity correlations (which scales with τ_p, see Chap. 4). Moreover, the absolute velocity in clustered regions is too low to significantly move clusters away from each other in the time scale of τ_p. It is noteworthy that this is in contrast with the situation described for large-persistence turbulent systems (see Chap. 6). We thus conclude that, in the liquid regime, hexatic clusters are the support to velocity correlations, *i.e.* the size of these clusters sets a maximum extent for velocity correlations, however the latter do not contribute significantly to the creation and melting of clusters. In the solid phase, we expect the velocity correlation length to assume its value for a perfectly ordered packing. This should be verified by comparing the influence of the persistence time τ_p on structural order and on $\xi_{\boldsymbol{v}}$.

7.3 Relaxation dynamics

Because these systems are far from equilibrium, there is no *a priori* reason for the emergence of structural order to correlate with a significant slowdown of the dynamics [49–51]. We thus now turn to quantitative dynamical descriptors of these dense ordered systems.

We plot in Fig. 7.4 the MSD (2.36) at different packing fractions ϕ, for small-persistence ($D_0 = 1$, $\tau_p = 10^{-2}$) and large-persistence ($D_0 = 0.1$, $\tau_p = 250$) systems. In the small-persistence case, we observe for packing fractions $\phi \gtrsim 0.94$ that the hexatic order correlations go to a plateau at large distance (see Fig. 7.3(a)), indicating a solid phase. We observe in the MSD that the transition to this solid phase is accompanied by the emergence of a subdiffusive regime, indicating a caging regime, similarly to the behaviour of dense disordered liquids close to the glass transition (see Chap. 3). In the large-persistence case, despite long-range hexatic order setting in at $\phi \gtrsim 0.87$ (see Fig. 7.3(b)), we do not observe any caging effect and the MSD goes smoothly from the initial ballistic to the eventual diffusive behaviour as it would in a simple liquid. We highlight that this behaviour was already reported in the case of athermal vibrated disks [51].

This simple MSD however hides an important heterogeneity in the relaxation process. Indeed we observe, at the largest packing fraction ϕ of our persistent system, that most particles are immobile in the crystal structure while large defective regions are very motile. It is the movement of these regions which relaxes the system. We show in Fig. 7.5 snapshots of the system at different times, highlighting the proportion of lost neighbours since initial time $C_{b,i}(t)$ (5.24) (Figs. 7.5(a, c, e, g)) and the argument of the hexatic order parameter $\arg(\psi_6)$ (2.28) (Figs. 7.5(b, d, f, h)) at the corresponding times. We observe at small times that the particles which have

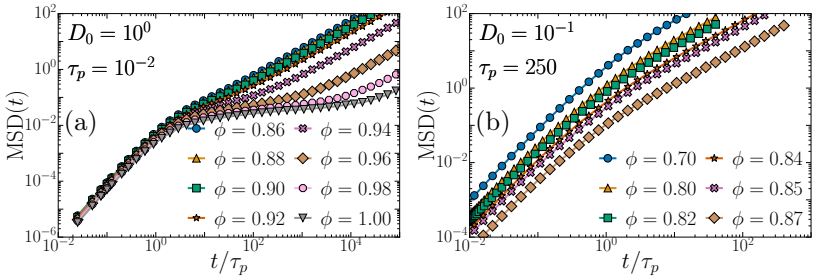

Figure 7.4: Mean squared displacement (2.36) for different packing fractions ϕ. Parameter values: $N = 16384$, (a) $D_0 = 1$, $\tau_p = 10^{-2}$, (b) $D_0 = 0.1$, $\tau_p = 250$.

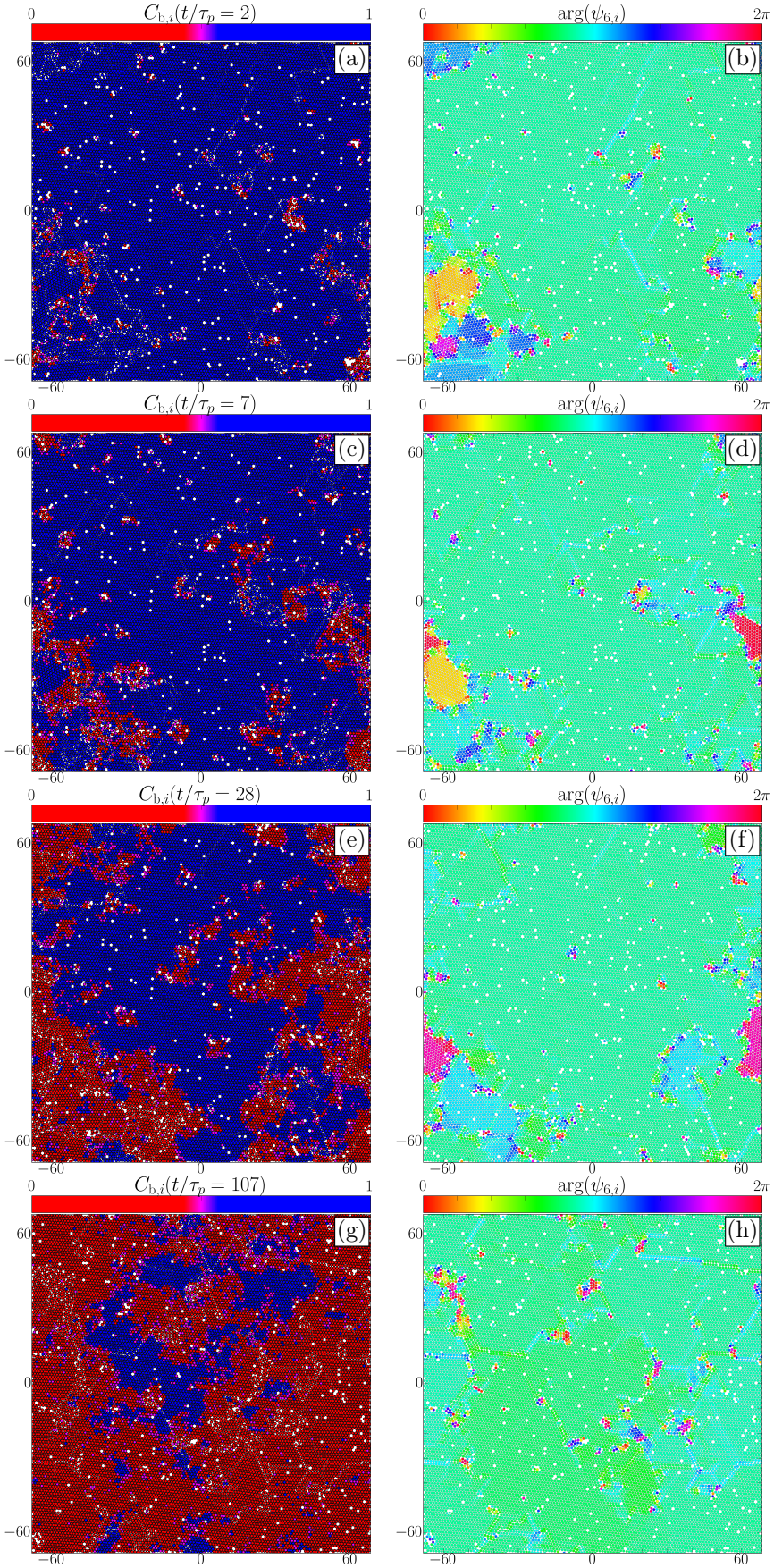

Figure 7.5: (a, c, e, g) Snapshots of the system highlighting the local bond breaking correlation $C_{\mathrm{b},i}$ (5.24) between time $t = 0$ and a lag time of (a) $t/\tau_p = 2$ ($C_{\mathrm{b}} = 0.96$), (c) $t/\tau_p = 7$ ($C_{\mathrm{b}} = 0.86$), (e) $t/\tau_p = 28$ ($C_{\mathrm{b}} = 0.64$), (g) $t/\tau_p = 107$ ($C_{\mathrm{b}} = 0.29$). (b, d, f, h) Snapshots of the argument of the hexatic order parameter $\arg(\psi_6)$ (2.28). Parameter values: $N = 16384$, $D_0 = 0.1$, $\tau_p = 250$, $\phi = 0.87$.

relaxed are located around the large defective regions. As time increases, these relaxed regions extend until the whole system is relaxed. This process of defects moving around the system, while other particles remain caged, conserves the global hexatic order. Therefore, even though the system is *structurally* a solid, it appears *dynamically* as a liquid [50, 51]. In other terms, the structure relaxes on time scales smaller (*i.e.* faster) than the global hexatic order. This process is reminiscent of dynamical facilitation and naturally leads to dynamical heterogeneity (compare to Fig. 5.8).

7.4 Conclusion: relaxation in dense monodisperse systems

Our model of isotropic self-propelled particles shows, in the monodisperse case at low persistence, a first transition with increasing packing fraction ϕ to an hexatic phase characterised by quasi-long-range orientational order and short-range translational order, and then a second transition at larger ϕ to a solid phase characterised by long-range orientational order and quasi-long-range translational order [46, 47, 49]. At large persistence time τ_p, it remains unclear if this two-step transition scenario holds.

At intermediate density ($\phi \approx 0.85$), the system is characterised by the presence of crystallites (within which both orientational and translational order is strongly correlated), immersed in a disordered fluid of defects (see Fig. 7.2(e)). Crystallites continuously coalesce and separate [51] over time scales larger than τ_p. The size of these crystallites sets an upper limit for the velocity correlation length (see Fig. 7.2(f), 7.3(d)).

At large density ($\phi \approx 0.87$), we find a phase with both long-range orientational order (as a solid phase) and short-range translational order (as a liquid or hexatic phase). We attribute the latter to the existence of large defective regions (see Fig. 7.2(g)). These regions are not localised dislocations as would be expected *e.g.* in an hexatic phase according to the KTHNY scenario, but rather active liquid bubbles. These are very motile and move across the system, thus relaxing the structure while preserving the global hexatic order (see Fig. 7.5). This process is akin to dynamical facilitation. As a consequence, the mean squared displacement (which is dominated by fast particles) shows no sign of caging, contrarily to low-persistence solid phases (see Fig. 7.4).

8 | Conclusion and perspectives

8.1 Summary

We introduced in Chap. 2 a model of isotropic self-propelled particles, namely active Ornstein-Uhlenbeck particles (AOUPs) (2.15, 2.16). We solve numerically the equations of evolution for the positions $\boldsymbol{r}_i$ and the propulsions $\boldsymbol{p}_i$, given the number of particles N, the polydispersity I, the free-particle self-diffusion constant D_0, the persistence time τ_p, and the packing fraction ϕ. This model has few control parameters, yet has a rich phenomenology. In the thermodynamic limit $N \to \infty$ at fixed I, the regimes corresponding to these different features may be understood by introducing a number of time and length scales and studying their relative importance. The time scales are: the interaction time τ_0 (1 in our units (2.14)) which sets the time scale to relax two-particle interactions, the persistence time τ_p (2.7) which sets the time scale over which the propulsion forces evolve, and the relaxation time τ_α (2.42) which sets the time scale over which the structure relaxes. The length scales are: the typical length between particles (of order 1), and the persistence length ℓ_p (2.12) which sets the typical length a particle travels before losing memory of its orientation. Equilibrium-like behaviour is found in the limit $\tau_p \ll \tau_0$ [22]. In the opposite limit, $\tau_p \gg \tau_0$, due to the coupling between density fluctuations and persistent forces [35, 103, 156], the system acquires several non-equilibrium properties: steeply decreasing velocity variance with increasing packing fraction, fat-tailed distributions of velocities, and mesoscale velocity correlations.

The introduction of polydispersity ($I = 0.2$ in our case) frustrates structural order, this enabled us to characterise the different disordered phases of AOUPs and their dynamics. We built in Chap. 3 the phase diagram of our model (see Fig. 3.6), in the polydisperse case, in the space spanned by the persistence time τ_p and the packing fraction ϕ. We identified three disordered phases: MIPS at moderate density and $\ell_p \gtrsim 1$ [1], the arrested glass at large ϕ [82], and the homogeneous liquid. In the arrested glass, $\tau_\alpha \gg \tau_p$ (see Fig. 3.1), while in MIPS $\tau_\alpha \lesssim \tau_p$ (see Fig. 3.5). The difference between these two limit regimes implies the existence of a dense homogeneous liquid phase at large persistence ($\tau_p \gg \tau_0$) whose dynamics interpolates from one to the other. This is in stark contract with monodisperse ($I = 0$) systems, where dense phases of persistent particles are orientationally and possibly translationally ordered [46]. We first studied the persistent liquid close to dynamical arrest ($\tau_\alpha \gg \tau_p$) and then the persistent liquid close to MIPS ($\tau_\alpha \lesssim \tau_p$).

We proposed in Chap. 4 a microscopic study of the dynamics in the homogeneous liquid on the path to dynamical arrest, in the limit $\tau_p \gg \tau_0$. First, we characterised the emerging velocity correlations. We established these extend over a length scale $\xi_{\boldsymbol{v}}$ which grows with the persistence time τ_p, and over a time scale $\tau_{\boldsymbol{v}} \sim \tau_p$ (see Figs. 4.2, 4.3). As a consequence of persistent forces, the system always sits close to a force-balanced configuration (see Fig. 4.1). This motivated the introduction of an effective potential energy U_{eff} (4.1) which is a function of both positions and propulsions, and whose local minima correspond to force-balanced configurations. In the equilibrium limit $\tau_p \ll \tau_0$, the dynamics may be mapped to a series of activated jumps between local minima of U [57]. In the persistent limit $\tau_p \gg \tau_0$, dynamics is intermittent (see Fig. 4.4): the system is in a force-balanced configuration $\nabla_i U_{\text{eff}} = 0$ which deforms smoothly with the evolution of propulsions $\boldsymbol{p}_i$ until this minimum is destabilised and the system quickly rearranges. This dynamics resembles plasticity in slowly sheared amorphous solids [34, 58]. Despite this difference in nature of the small-time $t \ll \tau_\alpha$ dynamics between the small- and large-persistence systems, both display important dynamical heterogeneities (see Figs. 4.5, 4.6), with movement over the time scale τ_α being correlated over increasing length scales as τ_α increases.

We took advantage of this effective potential representation to directly simulate the slow dynamics, from times $t \lesssim \tau_p$ to times $t \gtrsim \tau_\alpha$, in the limit $\tau_p \to \infty$ (see Chap. 5). To this effect, we used the activity-driven dynamics (ADD) algorithm [169] which is a quasistatic approximation of the dynamics in this limit. Similarly to other quasistatic methods such as athermal quasistatic shear (AQS) [58], ADD is decomposed into two elementary processes: sequences of elastic deformations in which the configuration of the system smoothly adapts to the evolution of propulsion forces, interrupted by plastic events which trigger instantaneous rearrangements (see Fig. 5.1). We denoted τ_{res} the typical time between two consecutive plastic events. During elastic deformations the movements of the particles are spatially correlated over the scale of the system (see Fig. 5.2). Plastic events take the form of avalanches, meaning that large-scale motion (including a large number of particles) may be triggered by an infinitesimal local change. We find that the participation in plastic events has a broad distribution and that these rearrangements trigger large elastic deformations far from their core (see Fig. 5.3(a, b)). Therefore, to characterise changes in the local structure around a given particle, we have to

take into account multi-particle quantities. To this effect we introduced the bond-breaking correlation function $C_b(t)$ which decorrelates over time τ_b [142]. We found that the dynamics slows down (see Fig. 5.6) and becomes more heterogeneous on the time scale of τ_b (see Figs. 5.8, 5.9(a)) as the self-propulsion velocity is decreased. We simulated the regime $\tau_{\rm res} \lesssim \tau_p$, in this case the dynamics is nearly diffusive at all times (see Fig. 5.4). In the regime $\tau_{\rm res} \gg \tau_p$, we may recover a two-step relaxation scenario, however to the best of our abilities we have not been able to simulate it. Finally, due to taking the limit of large persistence time $\tau_p \to \infty$ at fixed N, there is a dynamical length which scales with the system size. We thus find that the average dynamics of the system and its fluctuations both depend on N (see Figs. 5.7, 5.9(b)).

Turning to the persistent liquid close to MIPS (see Chap. 6), the limit $\tau_\alpha \lesssim \tau_p$ indicates that large displacements (of order at least 1) are correlated with the initial velocity field, the latter of which is correlated in space over a large length scale $\xi_{\boldsymbol{v}}$ in the limit $\tau_p \gg \tau_0$ (see Figs. 4.2(a, b)). We thus find the emergence of mesoscopic coherent flows in this regime. The velocity pattern, composed of large jets and swirls, is reminiscent of multi-scale flow patterns in inertial turbulence. We observe on time scales of several τ_p a chaotic and advective flow, which is characteristic of active turbulence [94] (see Fig. 6.8). In contrast to previous models displaying active turbulence, in particle dry polar models [100] which are the closest to our own model, velocity correlations are not the consequence of underlying alignment-induced propulsion correlations. Indeed, in our setting, velocity correlations emerge from the competition between crowding and persistent forces. We observe that these correlations, which are short-ranged, exhibit a scaling of the energy spectrum $E(k) \sim k^{-0.5}$ on small length scales (see Fig. 6.3). This behaviour is distinct from previously reported $E(k) \sim k^{-1}$ scaling in similar models [35, 103] and distinct from those reported for several active-turbulent systems [94]. However we do find a similar scaling for a model of aligning ABPs in the apolar regime where crowding is important in building velocity correlations (see Fig. 6.7). We thus hypothesize these models belong to a new class of active turbulence, not captured by the classification of Ref. [94], in which crowding plays a central role. Further research could elucidate if models as diverse as vibrated disks [208], self-aligning self-propelled particles [5, 209], or self-propelled Voronoi models of confluent tissues [210] display the same characteristics.

Given the question posed in the introduction (Chap. 1), *how does collective motion emerges from the competition between crowding and persistent forcing in isotropic active systems?*, we summarise in Fig. 8.1 our findings in the polydisperse case. In the limit $\tau_p \ll \tau_0$, we recover equilibrium-like dynamical heterogeneities on the time scale $\tau_\alpha \gg \tau_p$. At large persistence, $\tau_p \gg \tau_0$, extended velocity correlations emerge. We distinguish two forms of disordered collective motion. At large packing fraction, close to dynamical arrest, we observe similar dynamical heterogeneities on the time scale $\tau_\alpha \gg \tau_p$. At moderate density, close to MIPS, we observe mesoscopic flow with chaotic advection on the time scale $\tau_p \gtrsim \tau_\alpha$, similar to active turbulence. Due to the simplicity of the model, we expect the results we have presented to be generic over numerous active matter systems in which crowding effects compete with propulsion forces. More particularly, we think the various mechanisms we have described for the emergence of collective motion in simple active matter may inform the dynamics of more complex systems, *e.g.* dense self-propelled colloids [12, 13, 171] and dense cell tissues [5–7, 70].

In the monodisperse case, at small persistence time $\tau_p \ll \tau_0$, the disordered liquid transitions to an hexatic phase at large packing fraction ϕ, with quasi-long-range orientational order and short-range translational order

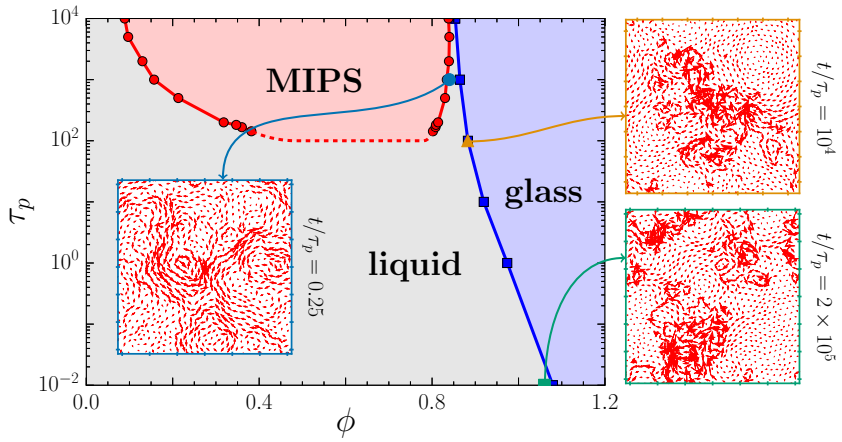

Figure 8.1: Phase diagram of polydisperse AOUPs ($I = 0.2$) for free-particle self-diffusion constant $D_0 = 1$ (see Fig. 3.6). We highlight for three distinct systems the displacements in the system over a time scale for which the MSD is of order 1. Blue circle: $\tau_p = 10^3, \phi = 0.84$. Yellow triangle: $\tau_p = 10^2, \phi = 0.8825$. Green square: $\tau_p = 10^{-2}, \phi = 1.06$.

(see Chap. 7). This picture evolves at moderate persistence ($\ell_p \lesssim 10$, $\tau_p \gg \tau_0$). For intermediate packing fractions ϕ, we find a cluster liquid phase in which small crystallites are formed but do not percolate into a system-wide ordered phase [211] (see Figs. 7.1, 7.2). At larger ϕ, the system develops long-range translational order, yet it features large defective regions which are active liquid bubbles (see Fig. 7.5). These bubbles move through the system to relax the entire structure while preserving the global hexatic structure. The presence of these large defects, different from isolated dislocations, is in contradiction with the KTHNY scenario. Further research should be devoted to the characterisation of these defective regions, such as the dependence of their density, size, and motility on the model parameters. It is also yet unknown how general this process may be within active matter models.

8.2 Future perspectives

Our work opens new questions on the behaviour of simple systems of self-propelled particles. Moreover, since experiments on self-propelled colloids are already available, in particular Janus colloids [10, 12, 13, 212, 213], our work offers new avenues for possible applications of these systems. We summarise in this Section some of these.

8.2.1 Coarsening of propulsions

We recall that persistence-induced velocity correlations do not necessitate propulsion alignment and thus emerge in the absence of propulsion force correlations [36, 88]. Yet it was reported that in infinitely-persistent systems, propulsion force correlations may emerge, even though there is no explicit aligning interactions [214].

Simulations with quenched self-propulsion force and started from an initial uncorrelated configuration show that when a given particle comes in contact with a new particle, these tend to travel longer times together if their propulsion directions are similar than if they are orthogonal. Through this sorting of neighbours, patches of particles with similar propulsions coarsen, and the system acquires finite-size propulsion correlations. To the best of our knowledge, there is no study of the steady state of these correlations in infinitely persistent systems, and in particular of the dependence of the propulsion correlation length on dynamical properties of the system and on the system size.

Moreover, it remains unclear if these correlations can emerge in finite-persistence systems. We hypothesize that this may be possible under two conditions. First, that there is a time scale τ_n characterising the time a particle needs to find neighbours with similar propulsions. This time, which should depend on dynamical properties of the system and possibly on the system size, must be smaller than the time over which the propulsions evolve, *i.e.* τ_p. Second, particles should stay significantly longer alongside particles with similar propulsions than alongside others. (In the infinitely-persistent case, the first condition is met because $\tau_p = \infty$, and we observe the second condition.) We have established that moderately dense persistent systems display chaotic mesoscopic flows in which, schematically, particles move in blocks with their neighbours over the time scale τ_p before creating new blocks and moving again. Particles deep within these blocks only exchange a few neighbours while particles on the outer rim quickly lose neighbours belonging to other blocks. This coherent movement brings the particles at a distance estimated by the standard deviation of displacement at τ_p from their initial positions, and this distance may be large compared to the interparticle distance (of order 1). In principle, this distance can be made as large as desired. This kind of flow may thus be a mechanism by which particles in the outer rim get to explore the system and find particles with similar orientations. This might be explored in future research.

8.2.2 Isotropic active turbulence in confinement

The ability to control the flow of simple active matter with external constraints has important practical applications such as drug delivery or material transport [215]. Recent experiments on two-dimensional confined microtubule-based active nematics [9] as well as aligning vibrated disks [216] show that confinement may induce regular spatiotemporal flow patterns. Concerning isotropic active matter, simulations of an effective one-dimensional system active Brownian particles (ABPs) showed that, in the regime where the persistence-induced velocity correlation length is of the size of the closed system, the whole system is able to move coherently in an ordered fashion [217]. Finally, using strong isotropic attraction within a system of two-dimensional ABPs, it was demonstrated that flocking may emerge in a system of isotropic monodisperse self-propelled particles [37]. In the polydisperse setting, where we have observed the emergence of active-turbulent flows, the interaction between the latter coherent dynamics and external confinement with increasingly complex geometries remains unexplored.

8.2.3 Using velocity correlations

The study of persistence-induced velocity correlations [35, 103, 156] relies on exponentially-decaying velocity autocorrelations (2.7). This is a very general hypothesis, which is verified for active Ornstein-Uhlenbeck particles, active Brownian particles, as well as run-and-tumble particles. However it could be possible to generate Gaussian-distributed propulsion forces whose autocorrelations decay slower or faster than exponential. This may be achieved by *e.g.* having the propulsion forces follow a continuous time random walk with appropriate waiting-time distributions [218]. There is a fundamental interest in this. First, scale-free velocity time autocorrelations might produce scale-free velocity spatial correlations. Second, fluctuations of the active force, which break equipartition of energy [35], may be used to stabilise crystalline packings in two dimensions [219].

References

[1] M. E. Cates and J. Tailleur, "Motility-Induced Phase Separation," Annual Review of Condensed Matter Physics **6**, 219–244 (2015).

[2] G. Parisi, P. Urbani, and F. Zamponi, *Theory of Simple Glasses: Exact Solutions in Infinite Dimensions* (Cambridge University Press, 2020).

[3] M. C. Marchetti, J. F. Joanny, S. Ramaswamy, T. B. Liverpool, J. Prost, M. Rao, and R. A. Simha, "Hydrodynamics of soft active matter," Reviews of Modern Physics **85**, 1143–1189 (2013).

[4] F. Schweitzer and J. Farmer, *Brownian Agents and Active Particles: Collective Dynamics in the Natural and Social Sciences*, 2nd ed., Springer Series in Synergetics (Springer, Berlin, New York, 2007).

[5] B. Szabó, G. J. Szöllösi, B. Gönci, Zs. Jurányi, D. Selmeczi, and T. Vicsek, "Phase transition in the collective migration of tissue cells: Experiment and model," Physical Review E **74**, 061908 (2006).

[6] M. Basan, J. Elgeti, E. Hannezo, W.-J. Rappel, and H. Levine, "Alignment of cellular motility forces with tissue flow as a mechanism for efficient wound healing," Proceedings of the National Academy of Sciences **110**, 2452–2459 (2013).

[7] S.-Z. Lin, W.-Y. Zhang, D. Bi, B. Li, and X.-Q. Feng, "Energetics of mesoscale cell turbulence in two-dimensional monolayers," Communications Physics **4**, 21 (2021).

[8] T. Sanchez, D. T. N. Chen, S. J. DeCamp, M. Heymann, and Z. Dogic, "Spontaneous motion in hierarchically assembled active matter," Nature **491**, 431–434 (2012).

[9] A. Opathalage, M. M. Norton, M. P. N. Juniper, B. Langeslay, S. A. Aghvami, S. Fraden, and Z. Dogic, "Self-organized dynamics and the transition to turbulence of confined active nematics," Proceedings of the National Academy of Sciences **116**, 4788–4797 (2019).

[10] D. Nishiguchi and M. Sano, "Mesoscopic turbulence and local order in Janus particles self-propelling under an AC electric field," Physical Review E **92**, 052309 (2015).

[11] F. Ginot, I. Theurkauff, D. Levis, C. Ybert, L. Bocquet, L. Berthier, and C. Cottin-Bizonne, "Nonequilibrium Equation of State in Suspensions of Active Colloids," Physical Review X **5**, 011004 (2015).

[12] N. Klongvessa, F. Ginot, C. Ybert, C. Cottin-Bizonne, and M. Leocmach, "Active Glass: Ergodicity Breaking Dramatically Affects Response to Self-Propulsion," Physical Review Letters **123**, 248004 (2019).

[13] N. Klongvessa, F. Ginot, C. Ybert, C. Cottin-Bizonne, and M. Leocmach, "Nonmonotonic behavior in dense assemblies of active colloids," Physical Review E **100**, 062603 (2019).

[14] J. L. Silverberg, M. Bierbaum, J. P. Sethna, and I. Cohen, "Collective Motion of Humans in Mosh and Circle Pits at Heavy Metal Concerts," Physical Review Letters **110**, 228701 (2013).

[15] N. Bain and D. Bartolo, "Dynamic response and hydrodynamics of polarized crowds," Science **363**, 46–49 (2019).

[16] M. Rubenstein, A. Cornejo, and R. Nagpal, "Programmable self-assembly in a thousand-robot swarm," Science **345**, 795–799 (2014).

[17] A. Cavagna, A. Cimarelli, I. Giardina, G. Parisi, R. Santagati, F. Stefanini, and M. Viale, "Scale-free correlations in starling flocks," Proceedings of the National Academy of Sciences **107**, 11865–11870 (2010).

[18] A. Cavagna and I. Giardina, "Bird Flocks as Condensed Matter," Annual Review of Condensed Matter Physics **5**, 183–207 (2014).

[19] H. Murakami, T. Niizato, T. Tomaru, Y. Nishiyama, and Y.-P. Gunji, "Inherent noise appears as a Lévy walk in fish schools," Scientific Reports **5**, 10605 (2015).

[20] A. P. Solon, J. Stenhammar, R. Wittkowski, M. Kardar, Y. Kafri, M. E. Cates, and J. Tailleur, "Pressure and Phase Equilibria in Interacting Active Brownian Spheres," Physical Review Letters **114**, 198301 (2015).

[21] A. P. Solon, Y. Fily, A. Baskaran, M. E. Cates, Y. Kafri, M. Kardar, and J. Tailleur, "Pressure is not a state function for generic active fluids," Nature Physics **11**, 673–678 (2015).

[22] É. Fodor, C. Nardini, M. E. Cates, J. Tailleur, P. Visco, and F. van Wijland, "How Far from Equilibrium Is Active Matter?" Physical Review Letters **117**, 038103 (2016).

[23] L. Caprini, A. Puglisi, and A. Sarracino, "Fluctuation–Dissipation Relations in Active Matter Systems," Symmetry **13**, 81 (2021).

[24] L. Tociu, É. Fodor, T. Nemoto, and S. Vaikuntanathan, "How Dissipation Constrains Fluctuations in Nonequilibrium Liquids: Diffusion, Structure, and Biased Interactions," Physical Review X **9**, 041026 (2019).

[25] R. N. Valani and D. M. Paganin, "Attractor-driven matter," Chaos: An Interdisciplinary Journal of Nonlinear Science **33**, 023125 (2023).

[26] A. Rabani, G. Ariel, and A. Be'er, "Collective Motion of Spherical Bacteria," PLoS ONE **8**, e83760 (2013).

[27] S. Garcia, E. Hannezo, J. Elgeti, J.-F. Joanny, P. Silberzan, and N. S. Gov, "Physics of active jamming during collective cellular motion in a monolayer," Proceedings of the National Academy of Sciences **112**, 15314–15319 (2015).

[28] L. M. Lemma, S. J. DeCamp, Z. You, L. Giomi, and Z. Dogic, "Statistical properties of autonomous flows in 2D active nematics," Soft Matter **15**, 3264–3272 (2019).

[29] T. Vicsek and A. Zafeiris, "Collective motion," Physics Reports **517**, 71–140 (2012).

[30] F. D. C. Farrell, M. C. Marchetti, D. Marenduzzo, and J. Tailleur, "Pattern Formation in Self-Propelled Particles with Density-Dependent Motility," Physical Review Letters **108**, 248101 (2012).

[31] H. H. Wensink and H. Löwen, "Emergent states in dense systems of active rods: From swarming to turbulence," Journal of Physics: Condensed Matter **24**, 464130 (2012).

[32] J. Tailleur and M. E. Cates, "Statistical Mechanics of Interacting Run-and-Tumble Bacteria," Physical Review Letters **100**, 218103 (2008).

[33] M. E. Cates and J. Tailleur, "When are active Brownian particles and run-and-tumble particles equivalent? Consequences for motility-induced phase separation," EPL (Europhysics Letters) **101**, 20010 (2013).

[34] R. Mandal, P. J. Bhuyan, P. Chaudhuri, C. Dasgupta, and M. Rao, "Extreme active matter at high densities," Nature Communications **11**, 1–8 (2020).

[35] S. Henkes, K. Kostanjevec, J. M. Collinson, R. Sknepnek, and E. Bertin, "Dense active matter model of motion patterns in confluent cell monolayers," Nature Communications **11**, 1405 (2020).

[36] L. Caprini, U. M. B. Marconi, and A. Puglisi, "Spontaneous velocity alignment in motility-induced phase separation," Physical Review Letters **124**, 078001 (2020).

[37] L. Caprini and H. Löwen, "Flocking without Alignment Interactions in Attractive Active Brownian Particles," Physical Review Letters **130**, 148202 (2023).

[38] P. K. Morse, S. Roy, E. Agoritsas, E. Stanifer, E. I. Corwin, and M. L. Manning, "A direct link between active matter and sheared granular systems," Proceedings of the National Academy of Sciences **118**, e2019909118 (2021).

[39] Y. Kuroda, H. Matsuyama, T. Kawasaki, and K. Miyazaki, "Anomalous fluctuations in homogeneous fluid phase of active Brownian particles," Physical Review Research **5**, 013077 (2023).

[40] J. U. Klamser, *Low-Dimensional Phase Transitions in and Outside Equilibrium*, Ph.D. thesis, Sorbonne Université (2018).

[41] B. I. Halperin and D. R. Nelson, "Theory of Two-Dimensional Melting," Physical Review Letters **41**, 121–124 (1978).

[42] U. Gasser, C. Eisenmann, G. Maret, and P. Keim, "Melting of Crystals in Two Dimensions," ChemPhysChem **11**, 963–970 (2010).

[43] E. Bernard, *Algorithms and Applications of the Monte Carlo Method: Two-dimensional Melting and Perfect Sampling*, Ph.D. thesis, École normale supérieure (2011).

[44] E. P. Bernard and W. Krauth, "Two-Step Melting in Two Dimensions: First-Order Liquid-Hexatic Transition," Physical Review Letters **107**, 155704 (2011).

[45] S. C. Kapfer and W. Krauth, "Two-Dimensional Melting: From Liquid-Hexatic Coexistence to Continuous Transitions," Physical Review Letters **114**, 035702 (2015).

[46] P. Digregorio, D. Levis, A. Suma, L. F. Cugliandolo, G. Gonnella, and I. Pagonabarraga, "Full phase diagram of active brownian disks: From melting to motility-induced phase separation," Physical Review Letters **121**, 098003 (2018).

[47] J. U. Klamser, S. C. Kapfer, and W. Krauth, "Thermodynamic phases in two-dimensional active matter," Nature Communications **9**, 5045 (2018).

[48] P. Digregorio, D. Levis, A. Suma, L. F. Cugliandolo, G. Gonnella, and I. Pagonabarraga, "2D melting and motility induced phase separation in Active Brownian Hard Disks and Dumbbells," Journal of Physics: Conference Series **1163**, 012073 (2019).

[49] G. S. Redner, M. F. Hagan, and A. Baskaran, "Structure and dynamics of a phase-separating active colloidal fluid," Physical Review Letters **110**, 055701 (2013).

[50] J. Bialké, T. Speck, and H. Löwen, "Crystallization in a Dense Suspension of Self-Propelled Particles," Physical Review Letters **108**, 168301 (2012).

[51] G. Briand and O. Dauchot, "Crystallization of self-propelled hard discs," Physical Review Letters **117**, 098004 (2016).

[52] L. Berthier and G. Biroli, "Theoretical perspective on the glass transition and amorphous materials," Reviews of Modern Physics **83**, 587–645 (2011).

[53] P. G. Debenedetti and F. H. Stillinger, "Supercooled liquids and the glass transition," Nature **410**, 259–267 (2001).

[54] L. Berthier, G. Biroli, J.-P. Bouchaud, L. Cipelletti, and W. van Saarloos, *Dynamical Heterogeneities in Glasses, Colloids, and Granular Media* (OUP Oxford, 2011).

[55] C. Scalliet, L. Berthier, and F. Zamponi, "Nature of excitations and defects in structural glasses," Nature Communications **10**, 5102 (2019).

[56] J.-P. Hansen and I. R. McDonald, *Theory of Simple Liquids*, 3rd ed. (Elsevier, Academic Press, Amsterdam, Boston, 2007).

[57] A. Heuer, "Exploring the potential energy landscape of glass-forming systems: From inherent structures via metabasins to macroscopic transport," Journal of Physics: Condensed Matter **20**, 373101 (2008).

[58] C. E. Maloney and A. Lemaître, "Amorphous systems in athermal, quasistatic shear," Physical Review E **74**, 016118 (2006).

[59] L. Berthier, "Dynamic Heterogeneity in Amorphous Materials," Physics **4** (2011), 10.1103/Physics.4.42.

[60] O. Dauchot, G. Marty, and G. Biroli, "Dynamical Heterogeneity Close to the Jamming Transition in a Sheared Granular Material," Physical Review Letters **95**, 265701 (2005).

[61] R. Candelier, O. Dauchot, and G. Biroli, "Building Blocks of Dynamical Heterogeneities in Dense Granular Media," Physical Review Letters **102**, 088001 (2009).

[62] F. Romá, S. Bustingorry, P. M. Gleiser, and D. Domínguez, "Strong Dynamical Heterogeneities in the Violation of the Fluctuation-Dissipation Theorem in Spin Glasses," Physical Review Letters **98**, 097203 (2007).

[63] A. J. Liu and S. R. Nagel, "Jamming is not just cool any more: Nonlinear dynamics," Nature **396**, 21–22 (1998).

[64] L. M. C. Janssen, "Mode-Coupling Theory of the Glass Transition: A Primer," Frontiers in Physics **6**, 97 (2018).

[65] T. R. Kirkpatrick and D. Thirumalai, "*Colloquium* : Random first order transition theory concepts in biology and physics," Reviews of Modern Physics **87**, 183–209 (2015).

[66] D. Chandler and J. P. Garrahan, "Dynamics on the Way to Forming Glass: Bubbles in Space-Time," Annual Review of Physical Chemistry **61**, 191–217 (2010).

[67] L. M. Janssen, "Active glasses," Journal of Physics: Condensed Matter **31**, 503002 (2019).

[68] H. Lama, M. Yamamoto, Y. Furuta, T. Shimaya, and K. A. Takeuchi, "Emergence of bacterial glass: Two-step glass transition in 2D bacterial suspension," (2022), arxiv:2205.10436 [cond-mat, physics:physics] .

[69] T. E. Angelini, E. Hannezo, X. Trepat, M. Marquez, J. J. Fredberg, and D. A. Weitz, "Glass-like dynamics of collective cell migration," Proceedings of the National Academy of Sciences **108**, 4714–4719 (2011).

[70] E. H. Zhou, X. Trepat, C. Y. Park, G. Lenormand, M. N. Oliver, S. M. Mijailovich, C. Hardin, D. A. Weitz, J. P. Butler, and J. J. Fredberg, "Universal behavior of the osmotically compressed cell and its analogy to the colloidal glass transition," Proceedings of the National Academy of Sciences **106**, 10632–10637 (2009).

[71] J.-A. Park, J. H. Kim, D. Bi, J. A. Mitchel, N. T. Qazvini, K. Tantisira, C. Y. Park, M. McGill, S.-H. Kim, B. Gweon, J. Notbohm, R. Steward Jr, S. Burger, S. H. Randell, A. T. Kho, D. T. Tambe, C. Hardin, S. A. Shore, E. Israel, D. A. Weitz, D. J. Tschumperlin, E. P. Henske, S. T. Weiss, M. L. Manning, J. P. Butler, J. M. Drazen, and J. J. Fredberg, "Unjamming and cell shape in the asthmatic airway epithelium," Nature Materials **14**, 1040–1048 (2015).

[72] L. Berthier and J. Kurchan, "Non-equilibrium glass transitions in driven and active matter," Nature Physics **9**, 310–314 (2013).

[73] G. Szamel, "Mode-coupling theory for the steady-state dynamics of active Brownian particles," The Journal of Chemical Physics **150**, 124901 (2019).

[74] D. Bi, X. Yang, M. C. Marchetti, and M. L. Manning, "Motility-Driven Glass and Jamming Transitions in Biological Tissues," Physical Review X **6**, 021011 (2016).

[75] R. Ni, M. A. C. Stuart, and M. Dijkstra, "Pushing the glass transition towards random close packing using self-propelled hard spheres," Nature Communications **4**, 2704 (2013).

[76] Y. Fily, S. Henkes, and M. C. Marchetti, "Freezing and phase separation of self-propelled disks," Soft Matter **10**, 2132–2140 (2014).

[77] L. Berthier, "Nonequilibrium Glassy Dynamics of Self-Propelled Hard Disks," Physical Review Letters **112**, 220602 (2014).

[78] G. Szamel, E. Flenner, and L. Berthier, "Glassy dynamics of athermal self-propelled particles: Computer simulations and a nonequilibrium microscopic theory," Physical Review E **91**, 062304 (2015).

[79] E. Flenner, G. Szamel, and L. Berthier, "The nonequilibrium glassy dynamics of self-propelled particles," Soft Matter **12**, 7136–7149 (2016).

[80] R. Mandal, P. J. Bhuyan, M. Rao, and C. Dasgupta, "Active fluidization in dense glassy systems," Soft Matter **12**, 6268–6276 (2016).

[81] L. Berthier, E. Flenner, and G. Szamel, "How active forces influence nonequilibrium glass transitions," New Journal of Physics **19**, 125006 (2017).

[82] L. Berthier, E. Flenner, and G. Szamel, "Glassy dynamics in dense systems of active particles," The Journal of Chemical Physics **150**, 200901 (2019).

[83] S. K. Nandi, R. Mandal, P. J. Bhuyan, C. Dasgupta, M. Rao, and N. S. Gov, "A random first-order transition theory for an active glass," Proceedings of the National Academy of Sciences **115**, 7688–7693 (2018).

[84] J. Tailleur, G. Gompper, M. C. Marchetti, J. M. Yeomans, and C. Salomon, eds., *Active Matter and Nonequilibrium Statistical Physics: Lecture Notes of the Les Houches Summer School: Volume 112, September 2018*, 1st ed. (Oxford University PressOxford, 2022).

[85] A. Liluashvili, J. Ónody, and T. Voigtmann, "Mode-coupling theory for active Brownian particles," Physical Review E **96**, 062608 (2017).

[86] V. E. Debets and L. M. C. Janssen, "Active glassy dynamics is unaffected by the microscopic details of self-propulsion," The Journal of Chemical Physics **157**, 224902 (2022).

[87] R. Mandal, S. K. Nandi, C. Dasgupta, P. Sollich, and N. S. Gov, "The random first-order transition theory of active glass in the high-activity regime," Journal of Physics Communications **6**, 115001 (2022).

[88] L. Caprini, U. M. B. Marconi, C. Maggi, M. Paoluzzi, and A. Puglisi, "Hidden velocity ordering in dense suspensions of self-propelled disks," Physical Review Research **2**, 023321 (2020).

[89] S. B. Pope, *Turbulent Flows* (CUP, 2000).

[90] U. Frisch, *Turbulence, the Legacy of A.N. Kolmogorov* (Cambridge University Press, 1995).

[91] G. Ariel, A. Rabani, S. Benisty, J. D. Partridge, R. M. Harshey, and A. Be'er, "Swarming bacteria migrate by Lévy Walk," Nature Communications **6**, 8396 (2015).

[92] G. Ariel, A. Be'er, and A. Reynolds, "Chaotic Model for Lévy Walks in Swarming Bacteria," Physical Review Letters **118**, 228102 (2017).

[93] A. Doostmohammadi, T. N. Shendruk, K. Thijssen, and J. M. Yeomans, "Onset of meso-scale turbulence in active nematics," Nature Communications **8**, 15326 (2017).

[94] R. Alert, J. Casademunt, and J.-F. Joanny, "Active Turbulence," Annual Review of Condensed Matter Physics **13**, 143–170 (2022).

[95] N. Goldenfeld, *Lectures on Phase Transitions and the Renormalization Group*, 1st ed. (CRC Press, 2018).

[96] L. Giomi, "Geometry and Topology of Turbulence in Active Nematics," Physical Review X **5**, 031003 (2015).

[97] M. Bär, R. Großmann, S. Heidenreich, and F. Peruani, "Self-Propelled Rods: Insights and Perspectives for Active Matter," Annual Review of Condensed Matter Physics **11**, 441–466 (2020).

[98] R. Alert, J.-F. Joanny, and J. Casademunt, "Universal scaling of active nematic turbulence," Nature Physics **16**, 682–688 (2020).

[99] R. Chatterjee, N. Rana, R. A. Simha, P. Perlekar, and S. Ramaswamy, "Inertia Drives a Flocking Phase Transition in Viscous Active Fluids," Physical Review X **11**, 031063 (2021).

[100] H. H. Wensink, J. Dunkel, S. Heidenreich, K. Drescher, R. E. Goldstein, H. Lowen, and J. M. Yeomans, "Meso-scale turbulence in living fluids," Proceedings of the National Academy of Sciences **109**, 14308–14313 (2012).

[101] S. Mukherjee, R. K. Singh, M. James, and S. S. Ray, "Intermittency, fluctuations and maximal chaos in an emergent universal state of active turbulence," Nature Physics **19**, 891–897 (2023).

[102] V. Bratanov, F. Jenko, and E. Frey, "New class of turbulence in active fluids," Proceedings of the National Academy of Sciences **112**, 15048–15053 (2015).

[103] G. Szamel and E. Flenner, "Long-ranged velocity correlations in dense systems of self-propelled particles," EPL (Europhysics Letters) **133**, 60002 (2021).

[104] U. M. B. Marconi, L. Caprini, and A. Puglisi, "Hydrodynamics of simple active liquids: The emergence of velocity correlations," New Journal of Physics **23**, 103024 (2021).

[105] C. Bechinger, R. Di Leonardo, H. Löwen, C. Reichhardt, G. Volpe, and G. Volpe, "Active particles in complex and crowded environments," Reviews of Modern Physics **88**, 045006 (2016).

[106] C. W. Gardiner, *Handbook of Stochastic Methods: For Physics, Chemistry, and the Natural Sciences*, 3rd ed., Springer Series in Synergetics (Springer, 2003).

[107] P. Jung and P. Hänggi, "Dynamical systems: A unified colored-noise approximation," Physical Review A **35**, 4464–4466 (1987).

[108] N. Sepúlveda, L. Petitjean, O. Cochet, E. Grasland-Mongrain, P. Silberzan, and V. Hakim, "Collective Cell Motion in an Epithelial Sheet Can Be Quantitatively Described by a Stochastic Interacting Particle Model," PLoS Computational Biology **9**, e1002944 (2013).

[109] D. Martin, J. O'Byrne, M. E. Cates, É. Fodor, C. Nardini, J. Tailleur, and F. van Wijland, "Statistical mechanics of active Ornstein-Uhlenbeck particles," Physical Review E **103**, 032607 (2021).

[110] P. Romanczuk, M. Bär, W. Ebeling, B. Lindner, and L. Schimansky-Geier, "Active Brownian particles: From individual to collective stochastic dynamics," The European Physical Journal Special Topics **202**, 1–162 (2012).

[111] L. Caprini, A. R. Sprenger, H. Löwen, and R. Wittmann, "The parental active model: A unifying stochastic description of self-propulsion," The Journal of Chemical Physics **156**, 071102 (2022).

[112] M. Abundo and E. Pirozzi, "Integrated stationary Ornstein–Uhlenbeck process, and double integral processes," Physica A **494**, 265–275 (2018).

[113] Y.-E. Keta and J. Rottler, "Cooperative motion and shear strain correlations in dense 2D systems of self-propelled soft disks," EPL (Europhysics Letters) **125**, 58004 (2019).

[114] N. Pottier, *Nonequilibrium Statistical Physics: Linear Irreversible Processes*, Oxford Graduate Texts (Oxford University Press, Oxford, 2010).

[115] E. Bitzek, P. Koskinen, F. Gähler, M. Moseler, and P. Gumbsch, "Structural Relaxation Made Simple," Physical Review Letters **97**, 170201 (2006).

[116] J. Guénolé, W. G. Nöhring, A. Vaid, F. Houllé, Z. Xie, A. Prakash, and E. Bitzek, "Assessment and optimization of the fast inertial relaxation engine (fire) for energy minimization in atomistic simulations and its implementation in lammps," Computational Materials Science **175**, 109584 (2020).

[117] R. Mannella, "Integration of stochastic differential equations on a computer," International Journal of Modern Physics C **13**, 1177–1194 (2002).

[118] W. Rüemelin, "Numerical treatment of stochastic differential equations," SIAM Journal on Numerical Analysis **19**, 604–613 (1982).

[119] K. Burrage, P. M. Burrage, and T. Tian, "Numerical methods for strong solutions of stochastic differential equations: An overview," Proceedings of the Royal Society of London. Series A: Mathematical, Physical and Engineering Sciences **460**, 373–402 (2004).

[120] M. P. Allen and D. J. Tildesley, *Computer Simulation of Liquids*, second edition ed. (Oxford University Press, Oxford, United Kingdom, 2017).

[121] Y.-E. Keta, "github.com/yketa/coll_dyn_activem," GitHub repository (2020), MIT licensed.

[122] A. Cavagna, "Supercooled liquids for pedestrians," Physics Reports **476**, 51–124 (2009).

[123] B. Widom, "Intermolecular Forces and the Nature of the Liquid State: Liquids reflect in their bulk properties the attractions and repulsions of their constituent molecules." Science **157**, 375–382 (1967).

[124] A. Wysocki, R. G. Winkler, and G. Gompper, "Cooperative motion of active Brownian spheres in three-dimensional dense suspensions," EPL (Europhysics Letters) **105**, 48004 (2014).

[125] I. Buttinoni, J. Bialké, F. Kümmel, H. Löwen, C. Bechinger, and T. Speck, "Dynamical Clustering and Phase Separation in Suspensions of Self-Propelled Colloidal Particles," Physical Review Letters **110**, 238301 (2013).

[126] A. B. Slowman, M. R. Evans, and R. A. Blythe, "Jamming and Attraction of Interacting Run-and-Tumble Random Walkers," Physical Review Letters **116**, 218101 (2016).

[127] D. Levis and L. Berthier, "Clustering and heterogeneous dynamics in a kinetic Monte Carlo model of self-propelled hard disks," Physical Review E **89**, 062301 (2014).

[128] F. Turci and N. B. Wilding, "Phase Separation and Multibody Effects in Three-Dimensional Active Brownian Particles," Physical Review Letters **126**, 038002 (2021).

[129] S. Mandal, B. Liebchen, and H. Löwen, "Motility-Induced Temperature Difference in Coexisting Phases," Physical Review Letters **123**, 228001 (2019).

[130] M. D. Rintoul and S. Torquato, "Metastability and Crystallization in Hard-Sphere Systems," Physical Review Letters **77**, 4198–4201 (1996).

[131] S. Auer and D. Frenkel, "Prediction of absolute crystal-nucleation rate in hard-sphere colloids," Nature **409**, 1020–1023 (2001).

[132] K. Binder and W. Kob, *Glassy materials and disordered solids: An introduction to their statistical mechanics* (World scientific, 2011).

[133] P. J. Steinhardt, D. R. Nelson, and M. Ronchetti, "Bond-orientational order in liquids and glasses," Physical Review B **28**, 784–805 (1983).

[134] A. K. Omar, K. Klymko, T. GrandPre, and P. L. Geissler, "Phase diagram of active brownian spheres: Crystallization and the metastability of motility-induced phase separation," Physical Review Letters **126**, 188002 (2021).

[135] A. Angell, "Liquid landscape," Nature **393**, 521–523 (1998).

[136] M. L. Ferrer, C. Lawrence, B. G. Demirjian, D. Kivelson, C. Alba-Simionesco, and G. Tarjus, "Supercooled liquids and the glass transition: Temperature as the control variable," The Journal of Chemical Physics **109**, 8010–8015 (1998).

[137] L. Berthier, "Time and length scales in supercooled liquids," Physical Review E **69**, 020201 (2004).

[138] L. Berthier, D. Chandler, and J. P. Garrahan, "Length scale for the onset of Fickian diffusion in supercooled liquids," Europhysics Letters (EPL) **69**, 320–326 (2005).

[139] E. Flenner and G. Szamel, "Fundamental differences between glassy dynamics in two and three dimensions," Nature Communications **6**, 7392 (2015).

[140] E. Flenner and G. Szamel, "Dynamic heterogeneity in two-dimensional supercooled liquids: Comparison of bond-breaking and bond-orientational correlations," Journal of Statistical Mechanics: Theory and Experiment **2016**, 074008 (2016).

[141] B. Illing, S. Fritschi, H. Kaiser, C. L. Klix, G. Maret, and P. Keim, "Mermin–Wagner fluctuations in 2D amorphous solids," Proceedings of the National Academy of Sciences **114**, 1856–1861 (2017).

[142] H. Shiba, T. Kawasaki, and A. Onuki, "Relationship between bond-breakage correlations and four-point correlations in heterogeneous glassy dynamics: Configuration changes and vibration modes," Physical Review E **86**, 041504 (2012).

[143] B. Guiselin, C. Scalliet, and L. Berthier, "Microscopic origin of excess wings in relaxation spectra of supercooled liquids," Nature Physics **18**, 468–472 (2022).

[144] W. Kob and H. C. Andersen, "Testing mode-coupling theory for a supercooled binary Lennard-Jones mixture I: The van Hove correlation function," Physical Review E **51**, 4626–4641 (1995).

[145] E. Flenner and G. Szamel, "Relaxation in a glassy binary mixture: Mode-coupling-like power laws, dynamic heterogeneity, and a new non-Gaussian parameter," Physical Review E **72**, 011205 (2005).

[146] P. Chaudhuri, L. Berthier, and W. Kob, "Universal Nature of Particle Displacements close to Glass and Jamming Transitions," Physical Review Letters **99**, 060604 (2007).

[147] C. Dasgupta, A. V. Indrani, S. Ramaswamy, and M. K. Phani, "Is There a Growing Correlation Length near the Glass Transition?" Europhysics Letters **15**, 307 (1991).

[148] G. Szamel, "Self-propelled particle in an external potential: Existence of an effective temperature," Physical Review E **90**, 012111 (2014).

[149] C. E. Maloney, "Correlations in the Elastic Response of Dense Random Packings," Physical Review Letters **97**, 035503 (2006).

[150] S. Henkes, C. Brito, and O. Dauchot, "Extracting vibrational modes from fluctuations: A pedagogical discussion," Soft Matter **8**, 6092 (2012).

[151] J. P. Wittmer, A. Tanguy, J.-L. Barrat, and L. Lewis, "Vibrations of amorphous, nanometric structures: When does continuum theory apply?" Europhysics Letters (EPL) **57**, 423–429 (2002).

[152] L. Abbaspour, R. Mandal, P. Sollich, and S. Klumpp, "Long-range Velocity Correlations from Active Dopants," (2023), arxiv:2302.13131 [cond-mat] .

[153] W. S. Slaughter, *The Linearized Theory of Elasticity* (Birkhäuser Boston, Boston, MA, 2002).

[154] M. Paoluzzi, D. Levis, and I. Pagonabarraga, "From motility-induced phase-separation to glassiness in dense active matter," Communications Physics **5**, 111 (2022).

[155] W. Kob, C. Donati, S. J. Plimpton, P. H. Poole, and S. C. Glotzer, "Dynamical Heterogeneities in a Supercooled Lennard-Jones Liquid," Physical Review Letters **79**, 2827–2830 (1997).

[156] L. Caprini and U. Marini Bettolo Marconi, "Active matter at high density: Velocity distribution and kinetic temperature," The Journal of Chemical Physics **153**, 184901 (2020).

[157] U. M. B. Marconi, N. Gnan, M. Paoluzzi, C. Maggi, and R. Di Leonardo, "Velocity distribution in active particles systems," Scientific Reports **6**, 23297 (2016).

[158] Y.-E. Keta, R. L. Jack, and L. Berthier, "Disordered Collective Motion in Dense Assemblies of Persistent Particles," Physical Review Letters **129**, 048002 (2022).

[159] C. Maggi, M. Paoluzzi, A. Crisanti, E. Zaccarelli, and N. Gnan, "Universality class of the motility-induced critical point in large scale off-lattice simulations of active particles," Soft Matter **17**, 3807–3812 (2021).

[160] A. Patch, D. Yllanes, and M. C. Marchetti, "Kinetics of motility-induced phase separation and swim pressure," Physical Review E **95**, 012601 (2017).

[161] S. De Karmakar, A. Chugh, and R. Ganesh, "Collective behavior of soft self-propelled disks with rotational inertia," Scientific Reports **12**, 22563 (2022).

[162] G. Brambilla, D. El Masri, M. Pierno, L. Berthier, L. Cipelletti, G. Petekidis, and A. B. Schofield, "Probing the Equilibrium Dynamics of Colloidal Hard Spheres above the Mode-Coupling Glass Transition," Physical Review Letters **102**, 085703 (2009).

[163] C. A. Angell, "Formation of Glasses from Liquids and Biopolymers," Science **267**, 1924–1935 (1995).

[164] G. Szamel, "Theory for the dynamics of dense systems of athermal self-propelled particles," Physical Review E **93**, 012603 (2016).

[165] H. Shiba, Y. Yamada, T. Kawasaki, and K. Kim, "Unveiling Dimensionality Dependence of Glassy Dynamics: 2D Infinite Fluctuation Eclipses Inherent Structural Relaxation," Physical Review Letters **117**, 245701 (2016).

[166] E. Woillez, Y. Zhao, Y. Kafri, V. Lecomte, and J. Tailleur, "Activated escape of a self-propelled particle from a metastable state," Physical Review Letters **122**, 258001 (2019).

[167] E. Woillez, Y. Kafri, and N. S. Gov, "Active trap model," Physical Review Letters **124**, 118002 (2020).

[168] R. Mandal and P. Sollich, "Multiple types of aging in active glasses," Physical Review Letters **125**, 218001 (2020).

[169] R. Mandal and P. Sollich, "How to study a persistent active glassy system," Journal of Physics: Condensed Matter **33**, 184001 (2021).

[170] N. Lačević, F. W. Starr, T. B. Schrøder, and S. C. Glotzer, "Spatially heterogeneous dynamics investigated via a time-dependent four-point density correlation function," The Journal of Chemical Physics **119**, 7372–7387 (2003).

[171] N. Klongvessa, C. Ybert, C. Cottin-Bizonne, T. Kawasaki, and M. Leocmach, "Aging or DEAD: Origin of the non-monotonic response to weak self-propulsion in active glasses," The Journal of Chemical Physics **156**, 154509 (2022).

[172] Y.-E. Keta, R. Mandal, P. Sollich, R. L. Jack, and L. Berthier, "Intermittent relaxation and avalanches in extremely persistent active matter," Soft Matter **19**, 3871–3883 (2023).

[173] Q. Liao and N. Xu, "Criticality of the zero-temperature jamming transition probed by self-propelled particles," Soft Matter **14**, 853–860 (2018).

[174] C. Villarroel and G. Düring, "Critical yielding rheology: From externally deformed glasses to active systems," Soft Matter **17**, 9944–9949 (2021).

[175] J. P. Sethna, K. Dahmen, S. Kartha, J. A. Krumhansl, B. W. Roberts, and J. D. Shore, "Hysteresis and hierarchies: Dynamics of disorder-driven first-order phase transformations," Physical Review Letters **70**, 3347–3350 (1993).

[176] C. Liu, E. E. Ferrero, F. Puosi, J.-L. Barrat, and K. Martens, "Driving Rate Dependence of Avalanche Statistics and Shapes at the Yielding Transition," Physical Review Letters **116**, 065501 (2016).

[177] M. Ozawa, L. Berthier, G. Biroli, A. Rosso, and G. Tarjus, "Random critical point separates brittle and ductile yielding transitions in amorphous materials," Proceedings of the National Academy of Sciences **115**, 6656–6661 (2018).

[178] ALGLIB, "Unconstrained optimization: L-BFGS and CG," (2021), accessed: 2021-04-02.

[179] Y. Nishikawa, M. Ozawa, A. Ikeda, P. Chaudhuri, and L. Berthier, "Relaxation Dynamics in the Energy Landscape of Glass-Forming Liquids," Physical Review X **12**, 021001 (2022).

[180] A. Ninarello, L. Berthier, and D. Coslovich, "Models and Algorithms for the Next Generation of Glass Transition Studies," Physical Review X **7**, 021039 (2017).

[181] H. Mizuno, H. Shiba, and A. Ikeda, "Continuum limit of the vibrational properties of amorphous solids," Proceedings of the National Academy of Sciences **114**, E9767–E9774 (2017).

[182] A. Lemaître, "Structural Relaxation is a Scale-Free Process," Physical Review Letters **113**, 245702 (2014).

[183] M. Lerbinger, A. Barbot, D. Vandembroucq, and S. Patinet, "Relevance of Shear Transformations in the Relaxation of Supercooled Liquids," Physical Review Letters **129**, 195501 (2022).

[184] K. Karimi, E. E. Ferrero, and J.-L. Barrat, "Inertia and universality of avalanche statistics: The case of slowly deformed amorphous solids," Physical Review E **95**, 013003 (2017).

[185] C. Maloney and A. Lemaître, "Subextensive Scaling in the Athermal, Quasistatic Limit of Amorphous Matter in Plastic Shear Flow," Physical Review Letters **93**, 016001 (2004).

[186] C. Maloney, (2022), private conversation.

[187] C. Heussinger, L. Berthier, and J.-L. Barrat, "Superdiffusive, heterogeneous, and collective particle motion near the fluid-solid transition in athermal disordered materials," EPL (Europhysics Letters) **90**, 20005 (2010).

[188] A. Bottinelli and J. L. Silverberg, "How to: Using Mode Analysis to Quantify, Analyze, and Interpret the Mechanisms of High-Density Collective Motion," Frontiers in Applied Mathematics and Statistics **3**, 26 (2017).

[189] A. Pal, S. Kostinski, and S. Reuveni, "The inspection paradox in stochastic resetting," Journal of Physics A: Mathematical and Theoretical **55**, 021001 (2022).

[190] A. Lemaître and C. Caroli, "Plastic response of a two-dimensional amorphous solid to quasistatic shear: Transverse particle diffusion and phenomenology of dissipative events," Physical Review E **76**, 036104 (2007).

[191] A. S. Keys, L. O. Hedges, J. P. Garrahan, S. C. Glotzer, and D. Chandler, "Excitations Are Localized and Relaxation Is Hierarchical in Glass-Forming Liquids," Physical Review X **1**, 021013 (2011).

[192] C. Scalliet, B. Guiselin, and L. Berthier, "Thirty Milliseconds in the Life of a Supercooled Liquid," Physical Review X **12**, 041028 (2022).

[193] A. Nicolas, K. Martens, and J.-L. Barrat, "Rheology of athermal amorphous solids: Revisiting simplified scenarios and the concept of mechanical noise temperature," EPL (Europhysics Letters) **107**, 44003 (2014).

[194] P. Sollich, F. Lequeux, P. Hébraud, and M. E. Cates, "Rheology of Soft Glassy Materials," Physical Review Letters **78**, 2020–2023 (1997).

[195] P. Sollich, "Rheological constitutive equation for a model of soft glassy materials," Physical Review E **58**, 738–759 (1998).

[196] S. M. Fielding, P. Sollich, and M. E. Cates, "Aging and rheology in soft materials," Journal of Rheology **44**, 323–369 (2000).

[197] O. Pouliquen and R. Gutfraind, "Stress fluctuations and shear zones in quasistatic granular chute flows," Physical Review E **53**, 552–561 (1996).

[198] R. P. Behringer, D. Bi, B. Chakraborty, S. Henkes, and R. R. Hartley, "Why Do Granular Materials Stiffen with Shear Rate? Test of Novel Stress-Based Statistics," Physical Review Letters **101**, 268301 (2008).

[199] K. A. Reddy, Y. Forterre, and O. Pouliquen, "Evidence of Mechanically Activated Processes in Slow Granular Flows," Physical Review Letters **106**, 108301 (2011).

[200] Y.-E. Keta, J. U. Klamser, R. L. Jack, and L. Berthier, "Emerging mesoscale flows and chaotic advection in dense active matter," (2023), arxiv:2306.07172 [cond-mat, physics:physics] .

[201] M. E. Fisher, "Correlation Functions and the Critical Region of Simple Fluids," Journal of Mathematical Physics **5**, 944–962 (1964).

[202] L. Caprini and U. Marini Bettolo Marconi, "Spatial velocity correlations in inertial systems of active Brownian particles," Soft Matter **17**, 4109–4121 (2021).

[203] A. Cavagna, I. Giardina, and T. S. Grigera, "The physics of flocking: Correlation as a compass from experiments to theory," Physics Reports **728**, 1–62 (2018).

[204] M. Bourgoin, "Turbulent pair dispersion as a ballistic cascade phenomenology," Journal of Fluid Mechanics **772**, 678–704 (2015).

[205] G. K. Batchelor, "The application of the similarity theory of turbulence to atmospheric diffusion," Quarterly Journal of the Royal Meteorological Society **76**, 133–146 (1950).

[206] M.-C. Jullien, J. Paret, and P. Tabeling, "Richardson Pair Dispersion in Two-Dimensional Turbulence," Physical Review Letters **82**, 2872–2875 (1999).

[207] J. M. Ottino, "Mixing, Chaotic Advection, and Turbulence," Annual Review of Fluid Mechanics **22**, 207–254 (1990).

[208] J. Deseigne, O. Dauchot, and H. Chaté, "Collective Motion of Vibrated Polar Disks," Physical Review Letters **105**, 098001 (2010).

[209] K.-D. N. T. Lam, M. Schindler, and O. Dauchot, "Self-propelled hard disks: Implicit alignment and transition to collective motion," New Journal of Physics **17**, 113056 (2015).

[210] F. Giavazzi, M. Paoluzzi, M. Macchi, D. Bi, G. Scita, M. L. Manning, R. Cerbino, and M. C. Marchetti, "Flocking transitions in confluent tissues," Soft Matter **14**, 3471–3477 (2018).

[211] D. Vågberg and L. Berthier, (2018), unpublished.

[212] A. Walther and A. H. E. Müller, "Janus particles," Soft Matter **4**, 663 (2008).

[213] F. Ginot, A. Solon, Y. Kafri, C. Ybert, J. Tailleur, and C. Cottin-Bizonne, "Sedimentation of self-propelled Janus colloids: Polarization and pressure," New Journal of Physics **20**, 115001 (2018).

[214] J. Yang, R. Ni, and M. P. Ciamarra, "Interplay between jamming and motility-induced phase separation in persistent self-propelling particles," Physical Review E **106**, L012601 (2022).

[215] Y. Hiratsuka, M. Miyata, and T. Q. Uyeda, "Living microtransporter by uni-directional gliding of Mycoplasma along microtracks," Biochemical and Biophysical Research Communications **331**, 318–324 (2005).

[216] G. Briand, M. Schindler, and O. Dauchot, "Spontaneously Flowing Crystal of Self-Propelled Particles," Physical Review Letters **120**, 208001 (2018).

[217] L. Caprini, C. Maggi, and U. Marini Bettolo Marconi, "Collective effects in confined active Brownian particles," The Journal of Chemical Physics **154**, 244901 (2021).

[218] V. Balakrishnan, "Continuous-time random walk theory and non-exponential decays of correlation functions," in *Stochastic Processes Formalism and Applications*, Vol. 184, edited by G. S. Agarwal and S. Dattagupta (Springer Berlin Heidelberg, Berlin, Heidelberg, 1983) pp. 96–103.

[219] L. Galliano, M. E. Cates, and L. Berthier, "Two-dimensional crystals far from equilibrium," (2023), arxiv:2302.11514 [cond-mat, physics:physics] .

A | Residual force

Patinet *et al.* [183] use the residual force $\boldsymbol{f}_{\mathrm{res},i}$ introduced by Lemaître [182] to identify regions with strong non-linear rearrangements.

We can compute the Taylor expansion of the force at time t

$$\begin{aligned}
-\frac{\partial U}{\partial r_{i\gamma}}(\{r_{j\delta}(t)\}_{j,\delta}) &= -\frac{\partial U}{\partial r_{i\gamma}}(\{r_{j\delta}(0)+\Delta r_{j\delta}(t)\}_{j,\delta}) \\
&= -\frac{\partial U}{\partial r_{i\gamma}}(\{r_{j\delta}(0)\}_{j,\delta}) - \sum_{k,\varepsilon}\left[\frac{\partial^2 U}{\partial r_{i\gamma}\partial r_{k\varepsilon}}(\{r_{j\delta}(0)\}_{j,\delta})\right]\Delta r_{k\varepsilon}(t) + \sum_{k,\varepsilon}\mathcal{O}(\Delta r_{k\varepsilon}(t)^2) \\
&= -\frac{\partial U}{\partial r_{i\gamma}}(0) - \sum_{k,\varepsilon} H_{i\gamma,k\varepsilon}(0)\Delta r_{k\varepsilon}(t) + \sum_{k,\varepsilon}\mathcal{O}(\Delta r_{k\varepsilon}(t)^2)
\end{aligned} \tag{A.1}$$

where $\mathbb{H}(0)$ is the Hessian matrix (5.13) computed with the positions at time 0. In ADD the effective potential U_{eff} (4.1) is minimised at all times t, therefore $-\partial_{r_{i\gamma}}U(t) = -(p_{i\gamma}(t) - \overline{p}_{i\gamma}(t))$. We introduce the residual force $\boldsymbol{f}_{\mathrm{res},i}(t)$ and the linear force $\boldsymbol{f}_{\mathrm{lin},i}(t)$ which are related by

$$\begin{aligned}
f_{\mathrm{res},i\gamma}(t) &= \sum_{k,\varepsilon} H_{i\gamma,k\varepsilon}(0)\Delta r_{k\varepsilon}(t) - \frac{\partial U(t)}{\partial r_{i\gamma}} + \frac{\partial U(0)}{\partial r_{i\gamma}} \\
&= \sum_{k,\varepsilon} H_{i\gamma,k\varepsilon}(0)\Delta r_{k\varepsilon}(t) - ((p_{i\gamma}(t) - \overline{p}_{i\gamma}(t)) - (p_{i\gamma}(0) - \overline{p}_{i\gamma}(0))) \\
&= f_{\mathrm{lin},i\gamma}(t) - ((p_{i\gamma}(t) - \overline{p}_{i\gamma}(t)) - (p_{i\gamma}(0) - \overline{p}_{i\gamma}(0))).
\end{aligned} \tag{A.2}$$

This definition ensures that $f_{\mathrm{res},i\gamma}(t) = 0$ if and only if the first-order Taylor expansion (A.1) is exact, *i.e.* if displacements $\{\Delta\boldsymbol{r}_j(t)\}_j$ are elastic.

With actual data, the movement is never purely elastic. We compute histograms of the norm of the residual force for different t (Fig. A.1), which should be bimodal at intermediate times, with a separation at a fixed value $|\boldsymbol{f}_{\mathrm{res}}|$ which we can identify to the threshold above which a particle has rearranged (see Ref. [183], Fig. SM2).

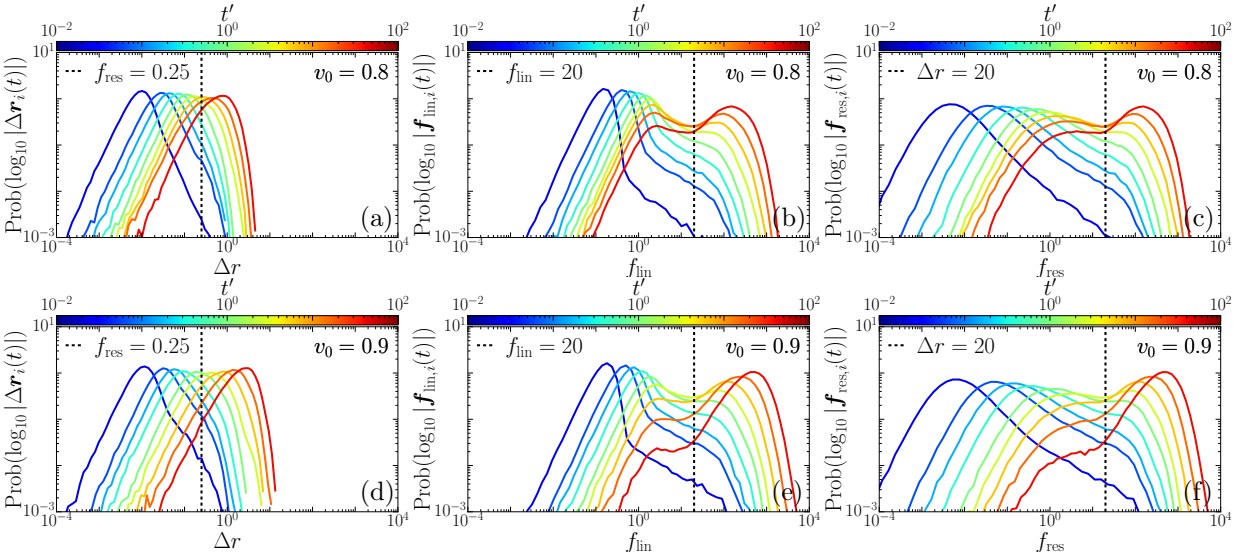

Figure A.1: (a, d) Histogram of the log-norm of displacements $|\Delta\boldsymbol{r}_i(t)|$ for different lag times t'. (b, e) Histogram of the log-norm of the linear force $|\boldsymbol{f}_{\mathrm{lin},i}(t)|$ for different lag times t. (c, f) Histogram of the log-norm of the residual force $|\boldsymbol{f}_{\mathrm{res},i}(t)|$ for different lag times t'. Dashed lines are added as guides to the eye. Parameter values: $N = 1024$, $\delta t' = 10^{-2}$, (a-c) $v_0 = 0.8$, (d-f) $v_0 = 0.9$.

B | Energy spectrum

We provide in this Appendix the proper definitions and properties of the energy spectrum $E(k)$.

B.1 Definition and reference-frame properties

Given a velocity field $\boldsymbol{V}(\boldsymbol{r}) = \sum_i \dot{\boldsymbol{r}}_i \delta(\boldsymbol{r} - \boldsymbol{r}_i)$ we compute its Fourier transform

$$\tilde{\boldsymbol{V}}(\boldsymbol{k}) = \int \mathrm{d}^2\boldsymbol{r}\, \boldsymbol{V}(\boldsymbol{r})\, e^{-\mathrm{i}\boldsymbol{k}\cdot\boldsymbol{r}} = \sum_i \dot{\boldsymbol{r}}_i\, e^{-\mathrm{i}\boldsymbol{k}\cdot\boldsymbol{r}_i} \tag{B.1}$$

$$\boldsymbol{V}(\boldsymbol{r}) = \int \mathrm{d}^2\boldsymbol{k}\, \tilde{\boldsymbol{V}}(\boldsymbol{k})\, e^{\mathrm{i}\boldsymbol{k}\cdot\boldsymbol{r}} \tag{B.2}$$

such that the average kinetic energy

$$\left\langle |\boldsymbol{V}|^2 \right\rangle = \frac{1}{L^2}\int \mathrm{d}^2\boldsymbol{r}\, \left\langle |\boldsymbol{V}(\boldsymbol{r})|^2 \right\rangle = \frac{1}{L^2}\int \mathrm{d}^2\boldsymbol{k}\, \left\langle |\tilde{\boldsymbol{V}}(\boldsymbol{k})|^2 \right\rangle = \frac{1}{L^2}\int \mathrm{d}k\, 2\pi k\, \left\langle |\tilde{\boldsymbol{V}}(\boldsymbol{k})|^2 \right\rangle_{|\boldsymbol{k}|=k} = \int \mathrm{d}k\, E(k) \tag{B.3}$$

where we have used Parseval's theorem, and introduced the *kinetic energy spectrum*

$$E(k) = E^{||}(k) + E^{\perp}(k),\ E^{||}(k) = \frac{2\pi k}{L^2}\left\langle |\tilde{\boldsymbol{V}}(\boldsymbol{k})\cdot\hat{\boldsymbol{k}}|^2 \right\rangle_{|\boldsymbol{k}|=k},\ E^{\perp}(k) = \frac{2\pi k}{L^2}\left\langle |\tilde{\boldsymbol{V}}(\boldsymbol{k})\wedge\hat{\boldsymbol{k}}|^2 \right\rangle_{|\boldsymbol{k}|=k}, \tag{B.4}$$

with $\hat{\boldsymbol{k}} = \boldsymbol{k}/|\boldsymbol{k}|$. We stress that we assumed isotropy so that we can replace the Fourier coefficient $\mathcal{F}(\boldsymbol{k})$ by its average value $\mathcal{F}(k)$ over all different orientations of the vector $\boldsymbol{k}$ ($|\boldsymbol{k}| = k$). In practice, we average over vectors $\boldsymbol{k} = (2\pi m/L, 2\pi n/L)$ such that $m, n \in \mathbb{Z}, |\boldsymbol{k}| \in [k - \delta k/2; k + \delta k/2]$ with $\delta k = 0.1$. By virtue of the Wiener-Khinchine theorem

$$\langle \boldsymbol{V}(\boldsymbol{0})\cdot\boldsymbol{V}(\boldsymbol{R})\rangle = \frac{1}{L^2}\int \mathrm{d}^2\boldsymbol{k}\, e^{\mathrm{i}\boldsymbol{k}\cdot\boldsymbol{R}}\left\langle |\tilde{\boldsymbol{V}}(\boldsymbol{k})|^2 \right\rangle = \int \mathrm{d}k\, J_0(kR)\, E(k) \tag{B.5}$$

where J_0 is the 0-th Bessel function of the first kind.

We introduce the velocities respectively to the centre-of-mass velocity $\overline{\boldsymbol{V}}$

$$\overline{\boldsymbol{V}} = \frac{1}{N}\sum_{i=1}^{N}\dot{\boldsymbol{r}}_i,\ \boldsymbol{v}_i = \dot{\boldsymbol{r}}_i - \overline{\boldsymbol{V}},\ \tilde{\boldsymbol{v}}(\boldsymbol{k}) = \sum_i \boldsymbol{v}_i e^{-\mathrm{i}\boldsymbol{k}\cdot\boldsymbol{r}_i} \tag{B.6}$$

such that $\sum_i \boldsymbol{v}_i = 0$. We can show

$$\left\langle |\tilde{\boldsymbol{v}}(\boldsymbol{k})|^2 \right\rangle = \sum_{i,j=1}^{N}\boldsymbol{v}_i\cdot\boldsymbol{v}_j e^{-\mathrm{i}\boldsymbol{k}\cdot(\boldsymbol{r}_i-\boldsymbol{r}_j)} = \left\langle |\tilde{\boldsymbol{V}}(\boldsymbol{k})|^2 \right\rangle - 2\,\Re\left[\left\langle \tilde{\boldsymbol{v}}(\boldsymbol{k})\cdot\sum_{i=1}^{N} e^{\mathrm{i}\boldsymbol{k}\cdot\boldsymbol{r}_i}\overline{\boldsymbol{V}}\right\rangle\right] - \left\langle |\overline{\boldsymbol{V}}|^2 \sum_{i,j=1}^{N} e^{-\mathrm{i}\boldsymbol{k}\cdot(\boldsymbol{r}_j-\boldsymbol{r}_i)}\right\rangle \tag{B.7}$$

where $\Re[\ldots]$ denotes the real part. We expect the centre-of-mass velocity $\overline{\boldsymbol{V}}$ to be independent from positions $\boldsymbol{r}_i$ and velocities $\boldsymbol{v}_i$ with respect to the centre of mass, and thus

$$\left\langle \tilde{\boldsymbol{v}}(\boldsymbol{k})\cdot\sum_{i=1}^{N} e^{\mathrm{i}\boldsymbol{k}\cdot\boldsymbol{r}_i}\overline{\boldsymbol{V}}\right\rangle = \left\langle \tilde{\boldsymbol{v}}(\boldsymbol{k})\sum_{i=1}^{N} e^{\mathrm{i}\boldsymbol{k}\cdot\boldsymbol{r}_i}\right\rangle \cdot \cancel{\left\langle \overline{\boldsymbol{V}}\right\rangle} = 0 \tag{B.8}$$

and

$$\left\langle |\overline{\boldsymbol{V}}|^2 \sum_{i,j=1}^{N} e^{-\mathrm{i}\boldsymbol{k}\cdot(\boldsymbol{r}_j-\boldsymbol{r}_i)}\right\rangle = \left\langle |\overline{\boldsymbol{V}}|^2\right\rangle \left\langle \sum_{i,j=1}^{N} e^{-\mathrm{i}\boldsymbol{k}\cdot(\boldsymbol{r}_j-\boldsymbol{r}_i)}\right\rangle = \left\langle |\overline{\boldsymbol{V}}|^2\right\rangle NS(\boldsymbol{k}) \tag{B.9}$$

where $S(\boldsymbol{k})$ is the structure factor (2.33). We note that

$$\left\langle |\tilde{\boldsymbol{V}}(\boldsymbol{k})|^2 \right\rangle = \mathcal{O}(N),\ \left\langle |\overline{\boldsymbol{V}}|^2\right\rangle = \mathcal{O}(1/N) \tag{B.10}$$

therefore the term (B.9) is $\mathcal{O}(1)$ and is thus subdominant in (B.7). In the large-N limit, we thus expect

$$\left\langle |\tilde{\boldsymbol{V}}(\boldsymbol{k})|^2 \right\rangle \approx \left\langle |\tilde{\boldsymbol{v}}(\boldsymbol{k})|^2\right\rangle \tag{B.11}$$

and can compute the energy spectrum (B.4) from either $\boldsymbol{V}$ or $\boldsymbol{v}$.

B.2 Low-k limit

We have exactly

$$\left\langle |\tilde{\boldsymbol{V}}(\boldsymbol{k}=0)|^2 \right\rangle = N^2 \left\langle |\overline{\boldsymbol{V}}|^2 \right\rangle \tag{B.12}$$

and thus

$$E(k) \underset{k\to 0}{\sim} \frac{2\pi k}{L^2} \left\langle |\tilde{\boldsymbol{V}}(\boldsymbol{k}=0)|^2 \right\rangle = 2\pi k \rho N \left\langle |\overline{\boldsymbol{V}}|^2 \right\rangle \tag{B.13}$$

where $\rho = N/L^2$ is the number density. We can also derive the limit for the individual parts by noting that

$$\left\langle |\tilde{\boldsymbol{V}}(\boldsymbol{k})\cdot\hat{\boldsymbol{k}}|^2 \right\rangle_{|\boldsymbol{k}|=k} = \frac{1}{2\pi}\int \mathrm{d}\theta \left\langle |\tilde{\boldsymbol{V}}(\boldsymbol{k})\cdot\hat{\boldsymbol{k}}|^2 \right\rangle = \frac{1}{2\pi}\int \mathrm{d}\theta \left\langle \left| \sum_{i=1}^{N} e^{-\mathrm{i}\boldsymbol{k}\cdot\boldsymbol{r}_i} \boldsymbol{V}_i \cdot \hat{\boldsymbol{k}} \right|^2 \right\rangle \tag{B.14}$$

where $\theta \equiv \arg(\boldsymbol{k})$ so that $\boldsymbol{V}_i \cdot \hat{\boldsymbol{k}} = V_{i,x}\cos\theta + V_{i,y}\sin\theta$. We take the $k \to 0$ limit in (B.14)

$$\begin{aligned}\left\langle |\tilde{\boldsymbol{V}}(\boldsymbol{k})\cdot\hat{\boldsymbol{k}}|^2 \right\rangle_{|\boldsymbol{k}|=k} &\underset{k\to 0}{=} \frac{1}{2\pi}\sum_{i,j=1}^{N}\int \mathrm{d}\theta \left[\langle V_{i,x}V_{j,x}\rangle \cos^2\theta + \langle V_{i,y}V_{j,y}\rangle \sin^2\theta + \langle V_{i,x}V_{j,y} + V_{i,y}V_{j,x}\rangle \cos\theta\sin\theta\right] \\ &= \frac{1}{2}\sum_{i,j=1}^{N}\langle \boldsymbol{V}_i\cdot\boldsymbol{V}_j\rangle = \left\langle |\tilde{\boldsymbol{V}}(\boldsymbol{k}=0)|^2 \right\rangle\end{aligned} \tag{B.15}$$

from which we conclude

$$E^{\parallel}(k) \underset{k\to 0}{=} E^{\perp}(k) \underset{k\to 0}{=} \frac{1}{2}E(k) \tag{B.16}$$

using (B.4).

B.3 Large-k limit

We expect to have

$$\left\langle |\tilde{\boldsymbol{V}}(\boldsymbol{k})|^2 \right\rangle = \sum_{i,j=1}^{N} \left\langle \boldsymbol{V}_i\cdot\boldsymbol{V}_j e^{-\mathrm{i}\boldsymbol{k}\cdot(\boldsymbol{r}_i-\boldsymbol{r}_j)} \right\rangle \underset{k\to\infty}{=} \sum_{i,j=1}^{N} \langle \boldsymbol{V}_i\cdot\boldsymbol{V}_j\,\delta_{ij}\rangle = \sum_{i=1}^{N}\left\langle |\boldsymbol{V}_i|^2 \right\rangle \tag{B.17}$$

which is lesser than $\left\langle |\tilde{\boldsymbol{V}}(\boldsymbol{k}=0)|^2 \right\rangle$, consistently with Ref. [78].

B.4 Energy spectrum from correlation function

It is also possible to evaluate the energy spectrum $E(k)$ from the correlation function (inverse as (B.5))

$$\begin{aligned}\left\langle |\tilde{\boldsymbol{v}}(\boldsymbol{k})|^2 \right\rangle &= \left\langle \left(\int \mathrm{d}^2\boldsymbol{r}\, e^{\mathrm{i}\boldsymbol{k}\cdot\boldsymbol{r}}\boldsymbol{v}(\boldsymbol{r})\right)\cdot\left(\int \mathrm{d}^2\boldsymbol{r}'\, e^{-\mathrm{i}\boldsymbol{k}\cdot\boldsymbol{r}'}\boldsymbol{v}(\boldsymbol{r}')\right)\right\rangle \\ &= \int \mathrm{d}^2\boldsymbol{r}\int \mathrm{d}^2\boldsymbol{r}'\, e^{\mathrm{i}\boldsymbol{k}\cdot(\boldsymbol{r}-\boldsymbol{r}')}\left\langle \boldsymbol{v}(\boldsymbol{r})\cdot\boldsymbol{v}(\boldsymbol{r}')\right\rangle \\ &= L^2\int \mathrm{d}^2\boldsymbol{R}\, e^{\mathrm{i}\boldsymbol{k}\cdot\boldsymbol{R}}\left\langle \boldsymbol{v}(\boldsymbol{0})\cdot\boldsymbol{v}(\boldsymbol{R})\right\rangle .\end{aligned} \tag{B.18}$$

We assume the correlation function has the form [201]

$$\langle \boldsymbol{v}(\boldsymbol{0})\cdot\boldsymbol{v}(\boldsymbol{R})\rangle = C(|\boldsymbol{R}|) = \frac{v_0^2}{(R/R_0)^a}e^{-R/\xi} \tag{B.19}$$

with $a < 2$, and thus

$$\left\langle |\tilde{\boldsymbol{v}}(\boldsymbol{k})|^2 \right\rangle = 2\pi L^2 \int \mathrm{d}R\, R\, J_0(kR) C(R) \tag{B.20}$$

where J_0 is the 0-th Bessel function of the first kind, therefore the energy spectrum

$$E(k) = \frac{2\pi k}{L^2}\left\langle |\tilde{\boldsymbol{v}}(\boldsymbol{k})|^2 \right\rangle = k v_0^2 (2\pi\xi)^2 (R_0/\xi)^a \Gamma(2-a)\, {}_2F_1\left(\frac{3-a}{2}, \frac{2-a}{2}, 1, -(k\xi)^2\right) \tag{B.21}$$

where Γ is the Euler Gamma function and ${}_2F_1$ is the hypergeometric function. $E(k)$ then has the following asymptotic expansions

$$E(k) \underset{k\to 0}{\sim} v_0^2(2\pi)^2\xi(R_0/\xi)^a\Gamma(2-a)(k\xi)^1, \tag{B.22}$$

$$E(k) \underset{k\to \infty}{\sim} v_0^2(2\pi)^2\xi(R_0/\xi)^a \frac{\Gamma(2-a)\Gamma\left(\frac{1}{2}\right)\Gamma(1)}{\Gamma\left(\frac{3-a}{2}\right)\Gamma\left(\frac{a}{2}\right)}(k\xi)^{-(1-a)}, \tag{B.23}$$

such that the behaviour $C(R) \sim R^{-\alpha}$ at small $R \ll \xi$ is mirrored in the decay $E(k) \sim k^{-(1-a)}$ at large k.